Analysis of the Interference Effects

Between Two Sears-Haack Bodies at Mach 2.7

By

Jeffrey Walter Bantle

B.A. June 1980, Ripon College

A Thesis submitted to

The Faculty of

The School of Engineering and Applied Sciences

of The George Washington University in partial satisfaction

of the requirements for the degree of Master of Science

December 1982

ABSTRACT

As part of a larger program to investigate the characteristics of multibody supersonic configurations, a study was conducted analyzing changes in wave drag due to interference effects between two Sears-Haack bodies at Mach 2.7 and zero degrees angle of attack. This study consisted of an experimental investigation and theoretical analysis of twin Sears-Haack bodies. In the experiment, pressure data was measured on one body while force data was measured on the other body. The study objectives were to better understand the interference effects between these bodies and determine the effectiveness of two theoretical methods (PAN AIR, a near-field panel method, and Far-Field Wave Drag, a method based on the supersonic area rule) in predicting these interference effects.

The study involved the analysis of pressure distributions and changes in wave drag associated with different relative positions of the bodies. Changes in wave drag were observed for combinations of both lateral separation and longitudinal skew of the two bodies. It was found that these changes in wave drag versus relative position of the bodies could be explained in terms of both shock location and shock strength. Results indicated that a significant reduction in wave drag could be obtained due to the favorable interference effects. These effects yielded a two-body configuration with less total drag than a single body of equal total volume and the same length.

Both theories satisfactorily predicted the changes in wave drag associated with different relative locations of the bodies shown by the experiment, especially when they were adjusted due to their use of the Mach line rather than the shock path. Thus, confidence was developed in these two theoretical techniques for their use in further analysis of multibody configurations.

ACKNOWLEDGEMENTS

TABLE OF CONTENTS

LIST OF FIGURES

LIST OF TABLES

SYMBOLS

C_{D_w}	wave drag coefficient
C_p	pressure coefficient
$D(co)$	total drag of the cut-off body (measured by the balance), lbs
$D(twice)$	total drag of a Sears-Haack body with twice the volume and the same length of the original single body, lbs
$D(1)$	total drag of a Sears-Haack body, lbs
$D(2)$	total drag of two isolated Sears-Haack bodies, interference-free, lbs
$D(2^*)$	total drag of two Sears-Haack bodies with favorable interference, lbs
$D_B(co)$	base pressure drag of the cut-off body, lbs
$D_F(co)$	skin friction drag of the cut-off body, lbs
$D_F(twice)$	skin friction drag of a Sears-Haack body of twice the volume and the same length, lbs
$D_F(1)$	skin friction drag of a Sears-Haack body, lbs
$D_F(2)$	skin friction drag of two isolated Sears-Haack bodies, interference-free, lbs
$D_F(2^*)$	skin friction drag of two Sears-Haack bodies with favorable interference, lbs
D_w	wave drag, lbs
D_{w_0}	wave drag, interference-free, lbs
D_{w_1}	total wave drag of the 30" body and the cut-off body under the influence of each other (configuration 1), lbs
D_{w_2}	total wave drag of two 30" bodies under the influence of each other (configuration 2), lbs
$D_w(co)$	wave drag of the cut-off body, lbs

$D_w(co)_1$ wave drag of the cut-off body under the influence of the 30" body, lbs

$D_w(twice)$ wave drag of a Sears-Haack body with twice the volume and the same length of the original single body, lbs

$D_w(1)$ wave drag of a single Sears-Haack body, lbs

$D_w(2)$ wave drag of two isolated Sears-Haack bodies, interference-free, lbs

$D_w(2*)$ wave drag of two Sears-Haack bodies with favorable interference, lbs

$D_w(30)_1$ wave drag of the 30" body under the influence of the cut-off body, lbs

$D_w(30)_2$ wave drag of the 30" body under the influence of the 30" body, lbs

d_{max} maximum diameter of the body, in

FR   fineness ratio $= \ell/d_{max}$

f   source strength, in^2/sec

ℓ length of the body, in

$(L/D)_{max}$ maximum lift-to-drag ratio

M_∞ freestream Mach number

p   pressure, lb/in^2

p_i isentropic pressure, lb/in^2

p_2 second-order pressure, lb/in^2

p_∞ freestream pressure, lb/in^2

q   dynamic pressure, lb/in^2

r   body radius, in

r_{max} maximum body radius, in

S   body cross-sectional area, in^2

SEP   lateral separation of the bodies, in

SHOCK LOC	intersection of the cut-off body nose shock and the 30" body centerline , inches from the nose of the 30" body
SKEW	longitudinal rearward displacement of the force body from the pressure body, in
t	time, sec
t_1	x variable of integration
U	decay function
$\vec{V}$	total velocity, in/sec
V_b	body volume, in^3
V_∞	freestream velocity magnitude, in/sec
$\vec{V}_\infty$	freestream velocity, in/sec
$\vec{W}$	total linearized mass flux, slug (in^2)
x	longitudinal coordinate along body axis, in
x_1	lengthwise variable of integration
x_2	lengthwise variable of integration
Z	position function

Greek symbols

β	Mach number parameter $= \left\| 1 - M_\infty^2 \right\|^{1/2}$
Δ	vertical distance force body is below pressure body, in
ΔC_p	change in pressure coefficient due to the shock
ΔD_w	change in wave drag from the noninterference case, lbs
∂	partial derivative
ζ	parametric variable
γ	specific heat ratio
μ	Mach angle, deg.
ρ	density, slug/in^3

ρ_∞ freestream density, slug/in^3

ϕ perturbation velicity potential, in^2/sec

ϕ_{xx} second derivative of ϕ with respect to x, sec^{-1}

ϕ_{yy} second derivative of ϕ with respect to y, sec^{-1}

ϕ_{zz} second derivative of ϕ with respect to z, sec^{-1}

θ azimuthal angle, deg

θ_1 relative angle of 0° pressure line to the force body, deg

θ_2 relative angle 90° pressure line to the force body, deg

INTRODUCTION

Throughout history, man has sought to travel faster in all modes of transportation. Flight has been no exception to this quest for increasing speed. As aircraft development is traced from the Wright "Flyer" of 1903 to the present state of modern jet-propelled aircraft, a significant increase in the speed of air travel occurs. Advanced technology developed during this era has not only resulted in an economical mass transportation system able to operate at very high subsonic speeds, but has also made flight at supersonic speeds possible.

Although present technology has enabled supersonic flight, it has not, as of yet, made supersonic flight economically feasible in a mass transportation system. The lack of widespread use of the supersonic transport by airline companies reflects the unsoundness of such a business venture. The Concorde is the only operating supersonic transport of today. It operates for about twice the cost of the more conventional wide-body subsonic transports, not to mention the high cost of its development and construction.

Large passenger capability, as well as new state-of-the-art technology (refs. 1 and 2), results in configurations approaching a more practical supersonic mass transportation vehicle. In the past, an increase in passenger capacity of a jet transport has generally yielded an economically favorable result. This more efficient condition is usually brought about by extending the length and/or diameter of the fuselage, hence increasing the passenger capacity, without an

1

appreciable increase in operating cost. Some of the current supersonic transports under study have a passenger capability of nearly 300 passengers (ref. 3) and are already in excess of 300 feet long. Further increases in passenger capacity are sought; however, a further appreciable extension in the length of the fuselage does not seem practical. Other possibilities enabling an increase in passenger capacity would be to increase the volume of the fuselage without increasing the length, or to use more than one fuselage. The multiple-fuselage concept is one of great interest, and there are currently double-bodied configurations under study (ref. 4). This idea of multiple-fuselage vehicles not only deals with the concept of increasing the passenger capacity but, also, introduces the notion of favorable interference effects resulting in a reduction of drag.

As an initial study of these multibody configurations and the interference effects taking place, this thesis presents an analysis of the interference effects between two isolated twin bodies in supersonic flow. Two theoretical techniques were compared with wind tunnel results for wave drag versus the relative position of the bodies. This study not only sought to understand the interference effects taking place, but to determine the effectiveness of each of the theoretical techniques in predicting these interference effects. Also, comparisons between these two isolated bodies were made with a single body of equal total volume.

Ramifications of this study of interference effects go beyond the design of multibodied configurations. Other uses of this analysis might be to study the effects of interference between components on launch

vehicle space systems as well as on different types of supersonic aircraft. This study might also be useful when analyzing the effects of adding external stores to configurations and the aerodynamic interactions during store separation.

BACKGROUND

With the onset of any research, it is desirable to examine any past research that might apply to the development of the new concept being considered. This effort proves difficult, however, when considering multiple-fuselage supersonic vehicles, since further development of conventional supersonic cruise vehicles is still needed. Nevertheless, there has been a number of research efforts considering interfering bodies at transonic and supersonic speeds, as well as actual past development and current interest in the technology of twin-fuselage aircraft.

Applicable to this research is an experimental investigation, by Georg Drougge (ref. 5), of the interference effects between bodies of revolution at transonic speeds (Mach numbers ranging form 0.8 to 1.15). Interference effects between two bodies and three bodies were observed with comparisons made between the two-body experimental results and a theory based on the supersonic area rule. While agreement between theory and experiment was not very good for the lower Mach numbers, much better comparisons were seen at the higher Mach number of 1.15 (see figure 1, which is a reproduction of Drougge's figure 18). In Appendix A of this report, some of Drougge's experimental results of two interfering bodies at Mach 1.15 were compared with the analysis tools used in the RESULTS AND ANALYSIS section of this research paper. The reader should note, however, that the data extracted from reference 5

4

was from rather austere graphs allowing only a general comparison of the trends and not detailed comparisons. Also, results from longitudinal movements and detailed pressure distributions were not provided. Experimental results at higher Mach numbers, closer to Mach numbers of interest for the design of supersonic aircraft, were also desirable, but not provided. Thus, further experimental data were needed to support the twin-body concept.

Another document of interest covers an experimental investigation, by Gapcynski and Carlson, of a body of revolution in the vicinity of a reflection plane at Mach numbers of 1.41 and 2.01 (ref. 6). Pressure distributions were obtained for different separations of the body and reflection plane with changes in axial force, normal force directed toward the plate, and pitching moment observed. Favorable areas of interference with respect to axial force were found for certain separations (refer to fig. 10 of ref. 6). In general, Gapcynski and Carlson found that for small separation distances the body is subject to positive axial-force increments, normal-force increments directed toward the plate, and pitching-moment increments tending to move the model nose away from the plate. As the separation distance is increased, but the body kept within the region of the reflected nose shock, the direction of these force and moment increments is reversed. All of these results can be understood when considering the shock location and its effect on the pressure distribution which will be analyzed in the RESULTS AND ANALYSIS section. While appicable to the multibody problem, mutual effects between the bodies and their shocks are not satisfactorily

analyzed this way. Also, longitudinal skews of the bodies cannot be analyzed using a reflection plane.

Friedman and Cohen, in reference 7, studied the wave drag of a system of bodies at zero angle of attack and supersonic speeds by means of linearized slender-body theory and reverse-flow theorems. They sought to determine the effect of varying the relative location of a principal body and adding auxiliary body or bodies in a two- or three-body system. They found beneficial arrangements, including ones resulting in two- or three-body systems having no more wave drag than that of a principal body alone (refer to figs. 9 and 10 of ref. 7). The most favorable position of the auxiliary body was with its maximum cross section slightly forward of the shock, while the least favorable was with the nose of the auxiliary body aligned with the shock. These are similar to some of the effects explained in the RESULTS AND ANALYSIS section of this study. While Friedman and Cohen presented results of some of the general effects on a particular auxiliary body, mutual effects between similar size bodies and experimental verification of these effects is needed in addressing the multibody problem.

An extension of the work presented in this particular report might be to consider optimizing the shape of a satellite body located in the flow field of another body. This problem was addressed by Rennemann in reference 8. Based on linearized theory, Rennemann derived a general expression for the cross-sectional-area distribution of the minimum-drag body of revolution of given volume and length in a nonuniform supersonic flow field. He concluded that "little or no advantage can be expected

from shaping satellite bodies for favorable interference drag."
Rennemann further commented that "the important parameter appears to be
the location of the satellite body." There are still other facets
concerning this problem, however, including considering bodies that are
not bodies of revolution.

These research efforts involving the study of interference effects
and body shaping, are paralleled by actual multibody configurational
studies. These studies include actual past double-body subsonic
aircraft and current studies of subsonic multibody aircraft and
multibody supersonic configurations.

The idea of twin-fuselage aircraft is not new. By the late
twenties, Italy had built twin-fuselage seaplanes; and in 1951 a
twin-fuselage configuration was used as a test bed for engines (see
ref. 9). North American built 272 twin-fuselage P-51 (P-82) Mustangs
allowing greater range, increased payload, and better takeoff
performance than its single-fuselage counterpart.

Recently, there has been renewed interest in the multibody concept.
Reference 10 indicated that a "multibody aircraft concept may offer
benefits similar to the span-distributed-load aircraft, yet retain
configurational and operational characteristics more like those of a
conventional transport aircraft." John Houbolt, in a recent article in
Astronautics & Aeronautics (ref. 9), took a look at multifuselage
subsonic aircraft. He states that twin-fuselage aircraft "would break
the stalemate in productivity with single-fuselage aircraft by a
compounding of beneficial design properties, and do this with or without

an infusion of advanced technology." He found that a "synergistic compounding of benefits" occurs. Due to the alleviation of wing-bending moments in twin-fuselage aircraft, higher aspect ratio wings may be used without a weight penalty; this leads to better aerodynamic performance than a single-fuselage aircraft. He also found reductions in friction drag, total fuselage weight, thrust requirements, wing and tail size, and fuel weight. As a result, Houbolt suggested that twin-body arrangements could yield as much as 40 percent increase in seat-miles per gallon over more conventional single-body aircraft.

In another Astronautics & Aeronautics article (ref. 4), Domenic Maglieri and Samuel Dollyhigh comment on the recent attention given to supersonic transports in "multilobe and multibody configurations of large passenger capacity." They contend that while increasing passenger capacity greatly, the multilobe concept keeps fuselage cross section to a minimum. Also, they add that recent studies show that for certain separation distances, the aerodynamic performance ($M_\infty L/D_{max}$) equals or exceeds that of single-fuselage configurations having only half the passenger capacity.

With interest focusing on the promising supersonic multibody concept, it is important to understand the interference effects taking place and to have useful theoretical prediction techniques. Thus, the need exists for this analysis of the interference effects between two isolated bodies and for the determination of the usefulness of two theories, PAN AIR and Far Field Wave Drag, in predicting these effects.

THEORETICAL METHODS USED FOR ANALYSIS

Two methods were used for the theoretical analysis of the inter-
ference effects between the isolated bodies with a third method added
for the bodies-alone analysis. These analysis techniques consisted of
the following: the Far-Field Wave Drag program, based on the supersonic
area rule; PAN AIR, a near-field panel method; and the Lighthill method,
restricted to use on isolated bodies of revolution. This section con-
tains a brief description and summary of the theoretical development of
each of these methods. Also, some comments were made about the
usability of each of these analysis tools.

Far-Field Wave Drag Theory

The Far-Field Wave Drag program computes the zero-lift wave drag of
an arbitrary configuration by utilizing the supersonic area rule, an
extension of the transonic area rule. The transonic area rule, from
reference 11, states that the transonic wave drag of a wing-body
combination is primarily dependent on the axial development of the
cross-sectional areas normal to the airstream. The rule assumes that the
wave drag of the aircraft is the same as the wave drag of an equivalent
body of revolution having the same cross-sectional area distribution.
It has been found that reasonably good wave-drag estimates can be made
near Mach 1 if slender-body theory (ref. 12) is applied to the aircraft
area distribution.

9

The slender-body theory utilizes the Prandtl-Glauert equation.

$$\beta^2 \Phi_{xx} + \Phi_{yy} + \Phi_{zz} = 0 \tag{1}$$

where

$$\beta^2 = \left| 1 - M_\infty^2 \right| \tag{2}$$

Von Karman, in reference 12, represented the flow about an axisymmetric body by the superposition of a uniform supersonic flow and a continuous supersonic source distribution along a line parallel to the flow. Von Karman, also, showed that the source density, $f(x)$, is related to the area distribution of the body, $S(x)$, by

$$f(x) = \frac{dS}{dx} \left[\frac{V_\infty}{2\pi} \right] \tag{3}$$

Using this relation and other conditions, he arrived at the drag of the body.

$$D_w = \frac{-\rho V_\infty^2}{4\pi} \int_0^\ell \int_0^\ell S''(x_1) \, S''(x_2) \, \ln \left| x_1 - x_2 \right| \, dx_1 \, dx_2 \tag{4}$$

The supersonic area rule is a generalization of the transonic area rule. It relates the wave drag of an aircraft at high Mach numbers to a number of developments of cross-sectional areas as intersected by Mach planes, thus producing a series of equivalent bodies (ref. 13). In figure 2, the supersonic-area-rule wave drag computing procedure, taken from reference 13, is illustrated. Each cross-sectional area development is determined by the normal components of cross-sectional areas as intersected by Mach planes inclined to the stream at the Mach angle μ. These inclined Mach planes can be oriented at different azimuthal angles, θ, forming a number of cross-sectional area developments, each

corresponding to a particular θ. Thus, at each Mach number, a series of equivalent bodies is generated. The wave drag of each of these equivalent bodies is determined by the von Karman slender-body formula (ref. 12), which gives the wave drag as a function of the equivalent-body area distribution and the freestream conditions (eqn. (4)). The wave drag of the aircraft is, then, taken to be the integrated average of the equivalent body wave drags.

$$D_w = \frac{1}{2\pi} \int_0^{2\pi} D_w(\theta) \, d\theta \tag{5}$$

The Far-Field Wave Drag program actually used is an extension in the configurational geometry package of the version contained in the wave drag portion of an aerodynamic design and analysis system for supersonic aircraft developed by Boeing Commercial Airplane Company. The new geometry package allows totally arbitrary configurations to be input, whereas the original Boeing geometry package stipulated that the configurations had to be symmetric about the $x - z$ plane. This new geometry package was written by Charlotte Craidon and is proposed for publication under the title, "Computer Program for Calculating the Zero Lift Wave Drag of Complex Aircraft Designs." The Boeing program documentation is given in references 14, 15, and 16. An analysis of the Far-Field Wave Drag program, contained in reference 17, concluded that "in addition to providing reasonably accurate supersonic wave drag estimates, the computer program provides a useful tool which can be used in design studies and for configurational optimization."

PAN AIR

PAN AIR, an abbreviation for Panel Aerodynamics, is a near-field panel method designed to analyze subsonic or supersonic inviscid flows about arbitrary configurations. Magnus and Epton (ref. 18, p. 1.0-1) define a panel method as

> "A program which solves a linear partial differential equation numerically by approximating the configuration surface by a set of panels on which unknown singularity strengths are defined, imposing boundary conditions at a discrete set of points, such as panel centers, and thereby generating a system of linear equations relating the unknown singularity strengths."

These linear equations can be solved for the singularity strengths which can be used to find properties of the flow.

The flow solutions from PAN AIR, as well as the Far-Field Wave Drag program, are governed by the Prandtl-Glauert equation for linearized compressible flow.

$$\beta^2 \phi_{xx} + \phi_{yy} + \phi_{zz} = 0 \tag{1}$$

where

$$\beta^2 = \left| 1 - M_\infty^2 \right| \tag{2}$$

The Prandtl-Glauert equation is the governing equation describing steady, inviscid, irrotational, isentropic flow with small perturbation assumptions. Due to the small perturbation assumptions, the Prandtl-Glauert equation

does not describe transonic flow nor hypersonic flow. A precise Mach number range over which the Prandtl-Glauert equation will apply is hard to determine due to the influence of the perturbation velocity in the small perturbation assumptions. For slender configurations, at small angles of attack, PAN AIR can be used over a much larger range of Mach numbers than for thick configurations, or for ones at high angles of attack.

Continuing with the development of PAN AIR, the Prandtl-Glauert equation is converted to an integral equation which can be solved using a general panel method. Using Green's Theorem, the Prandtl-Glauert equation is transformed to an integral equation. This equation is further simplified by introducing the source strength and doublet strength. With the addition of boundary conditions, a boundary value problem is posed.

The process by which a panel method solves this boundary value problem is known as discretization. In the first step of this process, the configuration surface is divided into panels. "Singularity parameters" (source and doublet strengths) are, then, defined at discrete points, while a source and doublet distribution are defined over each panel. A discrete set of points, where boundary conditions are imposed (called control points) are chosen. Each boundary condition imposed results in a linear equation in the unknown singularity parameters. There must be as many boundary conditions as singularity parameters to solve the system of linear equations.

Thus, we have a set of linear equations, one for each boundary condition. These linear equations can be solved, obtaining the singularity strength parameters. From these, we can arrive at the velocity potential and, hence, the local velocities. These resulting local velocities are, then, used to compute pressures. A more in-depth look at the development of PAN AIR is given in references 18 and 19.

A variety of pressure formulas is also available using PAN AIR. The second order pressure formula is:

$$P_2 = p_\infty - [\rho_\infty(\vec{V}_\infty \cdot \vec{V}) + \frac{1}{2}(\vec{V} \cdot \vec{W})] \tag{9}$$

and the isentropic formula is

$$P_i = p_\infty + \frac{\rho_\infty V_\infty^2}{\gamma M_\infty^2}\left\{\left[1 - \frac{\gamma-1}{2} \cdot \frac{M_\infty^2}{V_\infty^2}(V^2 - V_\infty^2)\right]^{\frac{\gamma}{\gamma-1}} - 1\right\} \tag{10}$$

In the solutions shown, force calculations result from the integrated isentropic pressure equation. Experience has shown, that in the range where linear theory is valid, the isentropic pressure equation agrees very closely with the second order pressure equation. When linear theory is violated, these two pressure equations tend to diverge from each other. This observation is quite useful in determining local regions where linear theory solutions are no longer valid.

As stated earlier, PAN AIR is a panel method; however, it contains a number of distinguishing features as compared to earlier, less complex, panel methods. First of all, PAN AIR allows continuous geometries to be input. Earlier panel methods left gaps in the geometry due to the configurational description. While this has little effect on subsonic flow, a significant effect is seen in supersonic flow since doublet

strengths must jump from zero to nonzero at the panel edge. Also, PAN AIR allows continuity of singularity strengths due to linear source and quadratic doublet variation on each panel. Earlier methods defined doublet and source strengths as locally constant, which caused discontinuities and resulted in numerical stability problems. Thus, PAN AIR contains improvements over earlier panel methods.

Lighthill Integral Method for Axisymmetric Bodies

Used in this study only to obtain pressure distributions of the bodies alone, the Lighthill method is restricted to use on isolated bodies of revolution. The equation for the surface pressure coefficient on a slender body of revolution, smooth or not smooth, has been shown by Lighthill in reference 20 to be

$$C_p = \frac{1}{\pi} \int_0^x \frac{U(Z)\, dS'(t_1)}{\beta\, r(t_1)} - [r'(x)]^2 \tag{11}$$

where

$$x = \text{body field station}$$
$$U(Z) = \text{decay function}$$
$$Z = \text{position function,} = \frac{x - t_1}{r(t_1)}$$

$$t_1 = \text{x variable of integration}$$
$$\beta = \text{Mach number parameter,} = |M^2 - 1|^{1/2}$$
$$r(t_1) = \text{body radius at } t_1$$
$$S'(t_1) = \text{first derivative of body cross-sectional area } S \text{ at } t_1$$
$$r'(x) = \text{first derivative of body radius } r \text{ at } x$$

A further discussion of this method and a numerical approach are given in reference 21. Equation (11) is easily evaluated numerically because the integrand is without singularities.

Usability Comparison of the Theoretical Methods

Before leaving this section on theories, some comments should be made on the actual usability of each of these programs. Although PAN AIR outputs more detailed information than the Far-Field Wave Drag program, it is more difficult to model geometries and uses more computer time and storage than does Far-Field Wave Drag.

In comparing the output information of these two programs, PAN AIR provides detailed pressure distributions from which forces and moments are calculated. The Far-Field Wave Drag program (FFWD), on the other hand, yields only the total zero-lift wave drag of the entire configuration.

Although FFWD does not give detailed pressure distributions, it is much easier to model input geometries with it than with PAN AIR. The expanded version of FFWD defines components using x, y, z coordinates with a reference point location associated with each component. Computer programs exist which allow configurations to be input in this format quite easily. Also, the reference points allow component movement or configurational changes with very little trouble. PAN AIR sets up a panel geometry which is very similar to this. However, component intersections are quite complex. Thus, configurational changes are very difficult to implement.

The Far-Field Wave Drag program is also much less costly to run than PAN AIR. The computer storage and time needed for PAN AIR is related to the number of panels needed for a configuration and the boundary conditions used. Boundary conditions are imposed at every

control point. Control points are located either at panel centers or panel edges, depending upon the use of sources and doublets and on the location of "abutment intersections" (ref. 18). For each boundary condition, a linear equation is formed. Thus, PAN AIR must solve a matrix whose size depends upon the number of boundary conditions imposed, which depends on the number of panels used. Thus, PAN AIR requires much more computer time and storage than FFWD which calculates a series of cross-sectional area distributions.

EXPERIMENTAL PROGRAM

Wind-Tunnel Facility

The experimental research was conducted in test section 2 of NASA, Langley Research Center's Unitary plan wind tunnel. This is a continuous flow, closed circuit, pressure tunnel with two 4x4x7-foot test sections which cover a Mach number range from 1.46 to 4.63. A detailed description and calibration of the wind tunnel can be found in reference 24.

The 100,000 horsepower compressor drive system consists of the starting motor, main drive motor, and six compressors. The main drive motor is located in line with three compressors on each end, while the starting motor is offset and transmits power to this drive line through a speed increase gear.

Test capability over a continuous Mach number range is provided by two test sections. Test section 1 covers the Mach number range from 1.46 to 2.86, and test section 2 covers the Mach number range from 2.30 to 4.63. The Mach number is varied by adjusting an asymmetric sliding-block nozzle that changes the throat-to-test-section area ratio.

Many methods are available for the support of models. The basic model support system consists of a horizontal wall-mounted strut capable of forward and aft travel of 36.25 inches. Attached to the strut is a sting support which allows ± 20 inches of traverse, or lateral, movement and ± 14 degrees of sideslip motion. In front of the sting support is the angle-of-attack mechanism and roll mechanism.

The data acquisition system includes 100 analog and 40 digital recording channels coupled to a Sigma 3 computer with various input and output devices. Force and moment data are measured by strain-gauge balances, while pressure data are taken with pressure transducers used with scanning valves.

Wind Tunnel Models and Support Apparatus

The wind-tunnel research models consisted of two Sears-Haack bodies. One was cut off at the back and sting mounted; the other was mounted on a strut and bolted to the sidewall of the tunnel. Force measurements were made on the cut-off body, while pressure data was measured on the sidewall-mounted body.

The governing equations for a Sears-Haack body, or body of minimum wave drag, are, in parametric form (ref. 22):

$$x(\zeta) = \frac{\ell}{2} (1+\cos\zeta) \tag{9a}$$

$$S(\zeta) = \frac{4V_b}{\ell}(\sin\zeta - 1/3 \sin(3\zeta)) \tag{9b}$$

where ℓ = length of the body

V_b = volume of the body

ζ = parametric variable varying from 180° to 0° for
x varying from 0 to ℓ

x = longitudinal axis

A closed form equation can also be written describing a Sears-Haack body (ref. 21):

$$r = r_{max} \{1 - (\frac{2x}{\ell} -1)^2\}^{3/4} \tag{10}$$

where   x = longitudinal axis
        ℓ = length of the body
        r = radius at longitudinal location x
    r_{max} = maximum radius of the body

The pressure body, shown in figure 3, had the following characteristics:

    ℓ = 30 inches
    V_b = 58.87 in^3
    r_{max} = 1.03 in

The pressure body had a total of 120 pressure orifices connected to

six, 5 psi, scanning valves. The side row of orifices, numbered 100

through 158, was referred to as the 0 degree line of pressure orifices,

while the top row of orifices, numbered 200 through 258, was referred to

as the 90 degree line of pressure orifices (see fig. 3). Each row con-

tained 59 orifices, one spaced every half inch. There were also two

orifices located on the bottom of the model. One was located $3\frac{1}{2}$ inches

back from the nose, directly below orifice 206, and was labeled orifice

306; and the other was located $26\frac{1}{2}$ inches back from the nose, directly

below orifice 252, and was labeled orifice 352. These two orifices were

used to zero the angle of attack of the pressure model.

The pressure body was mounted to the sidewall of the wind tunnel on

a blade strut and could be adjusted vertically and slightly in pitch

using a 4-inch slot in the base of the strut. The blade strut, also

shown in figure 3, had a sweep of 70 degrees near the body and a sharp

leading edge to reduce the strength of the leading-edge shock. The strut

contained the 120 pressure tubes connecting the orifices to the scanning

valves.

The force body, shown in figure 4, can be described by the same

equations as the pressure body (parametric equations (9a) and (9b), and

equation (10)) but was cut off at x = 26.80 inches where r = .50 inches. This allowed the model to be mounted on a 3/4-inch diameter sting.

The six component, parallel-wired, strain gauge balance used had small maximum deflections to allow a high degree of precision. The accuracy of this balance for any particular component measured is about .5 percent of the maximum reading for that component. Experience has shown that measurement repeatability is even better than .5 percent. The maximum balance deflections allowed were 4 pounds in axial force, 10 pounds in side force, and 70 pounds in normal force. The maximum moments allowed were 10 inch-pounds in rolling moment, 8 inch-pounds in yawing moment, and 50 inch-pounds in pitching moment. Although the balance provided the required accuracy, it presented operational difficulties due to the relatively small range of allowable forces and moments.

Two other important elements of the experimental apparatus included a 24-inch long sting extension and a dogleg sting adjustment. The sting extension was used to extend the sting of the force body enabling its movement throughout the test section. The dogleg sting adjustment enabled vertical movement of the force body. The need for this type of movement is explained in the following section, Experimental Test.

Experiment

The wind tunnel experiment was conducted at a Mach number of 2.70 and a Reynolds number of 2.00×10^6 per foot. Test section 2 was chosen due to the very small variations in both Mach number and flow angularity throughout the test section at the test Mach number of 2.70 (see ref. 24).

This is important since the bodies were located at different positions throughout the test section during the wind tunnel test.

The entire test was performed with each of the bodies at an angle of attack of zero degrees. For the force body, this was done by adjusting the angle of attack to obtain zero normal force throughout the test under noninterference conditions or interference conditions with the bodies in the same x - y plane. For the pressure body, zero angle of attack was obtained by adjusting the angle, using the slotted wall attachment, until pressure orifices 206 and 306 read the same, or very nearly the same, pressure. The angle of attack could also be checked using the same type of comparison between pressure orifices 252 and 352. These pairs of orifices were located on the top and bottom of the model, 180 degrees apart, (see the Wind Tunnel Models and Support Apparatus section) and must read the same pressure for the model to be at zero degrees with the wind.

The parameters defining the relative position of the bodies are shown in figure 5. Note the definitions of SEP, the lateral distance between the bodies, and SKEW, the longitudinal displacement of the force body. Also, positive SKEW is shown to be the longitudinal distance the force body is displaced behind the pressure body.

The actual relative position of the bodies during the experiment is given in the test matrix shown in figure 6. SEP varied from 3 inches to 15 inches while SKEW varied from -45 inches to +48 inches. The selection of the two sidewall mounting positions for the pressure body were chosen on the basis of the test section size limitation, the sting apparatus

movement limitations, and the actual places that attachments could be made to the sidewall. Case 1 shows the rearward position of the pressure body with force data being measured on the forward body. Case 2 shows the forward position of the pressure body with force data now being measured on the rear body.

Size constraints on the body and blade limited the number of pressure orifices. Thus, only a 0 degree line and a 90 degree line of orifices were used (see the Wind Tunnel Models and Support Apparatus section). However, a denser distribution of pressures around the body is desirable to obtain the drag of the pressure body. This can be done by the radial movement of the force body around the pressure body. This effectively varies the 0 degree line of orifices from 0 degrees to 90 degrees and, concurrently, the 90 degree line of orifices from 90 degrees to 180 degrees. This is depicted in figure 7(a). In position 1, the bodies are located in the same $x - y$ plane, hence, with a 0 degree line and 90 degree line of pressures. With the force body in position 2, the 0 degree line on the pressure body is effectively at 90 degrees relative to the force body, while the 90 degree line on the pressure body is effectively at 180 degrees relative to the force body. Thus, a pressure distribution varying θ from 0 degrees to 180 degrees around the body can be obtained enabling the calculation of wave drag. Note in figure 7(b) the definition of θ_1 as the relative angle of the 0 degree line to the force body, while θ_2 is the relative angle of the 90 degree line in force body. Note, also, the definition of Δ as the vertical distance the force body has been dropped below the pressure body.

The radial movement of the force body around the pressure body is accomplished using a dogleg attachment to the sting and a traverse motion of the sting apparatus. Moving the body along the circular arc in figure 7(b) from position 1 to a position 3 is accomplished using a dogleg attachment to the sting allowing a vertical drop of Δ. A corresponding traverse movement allows the radius, or SEP, to be held constant. Quantum drops, or drops only in steps, were allowed by the dogleg attachment; however, adjustments of a continuous nature could be made to the height of the pressure model using a 4-inch slot on the blade wall attachment. Thus, with these adjustments, any particular θ between 0 degrees and 180 degrees could be obtained. For any particular θ_1 or θ_2 chosen, the needed vertical drop, Δ, can be found as follows:

$$\Delta = (SEP)\ \sin\theta_1 = -(SEP)\ \sin(90^\circ - \theta_2) \tag{11}$$

and

$$\theta_2 = 90^\circ + \theta_1 \tag{12}$$

It should be pointed out, however, that in keeping with good experimental procedure, the number of movements of the pressure body were minimized. This minimized the effects of physical changes in the test apparatus on the outcome of the experiment.

A summary of all the particular cases tested is found in Table I. The point numbers corresponding to each particular configuration (SEP, SKEW, Δ, θ_1, θ_2) is the key to locating the experimental data in reference 25. Also, a picture of the bodies in the wind tunnel is shown in figure 8.

Data Reduction

Both the force body and pressure body had unwanted external forces and interference that needed to be considered during the gathering and reduction of the wind tunnel data. For the force body, these included skin friction drag and drag due to the chamber (or base) pressure. For the pressure body, there were unwanted interference effects from the blade used to mount it on the sidewall and, also, disturbances from the sting apparatus of the force body on the pressure body for certain configurations.

While all the results contain comparisons of wave drag, the balance in the force body measured the total drag on the cut-off body. The total drag, measured by the balance, of the cut-off body can be expressed as follows.

$$D \ (co) = D_W \ (co) + D_F \ (co) + D_B \ (co) \tag{13}$$

where

$D \ (co)$ = total drag on the cut-off body
(that measured by the balance)

$D_W \ (co)$ = wave drag of the cut-off body

$D_F \ (co)$ = skin friction drag of the cut-off body

$D_B \ (co)$ = base pressure drag of the cut-off body

As can be seen from the above relation, estimates of the skin-friction drag and base-pressure drag were needed to determine the wave drag of the cut-off body.

The skin-friction drag of the force body was calculated using the Aerodynamic Design and Analysis System for Supersonic Aircraft developed

by Boeing (refs. 16, 17, and 18). This analysis system makes use of the T' method for the calculation of skin-friction drag. The theory and experimental verification of the T' method are given in reference 26 with a short summary contained in reference 16. The T' method is based on the calculation of a compressible skin-friction coefficient from a reference skin friction coefficient for a given Mach number, Reynolds number, and adiabatic wall temperature. Subtracting both the base pressure drag, computed using measured data from two chamber pressure tubes in the base of the model, and the skin-friction drag from the balance reading resulted in the wave drag of the force body.

While the wave drag of the pressure body was found by integrating the axial component of the orifice pressures over the body surface, there were external effects that needed to be considered first. There was interference to each line of pressure due to the blade connection of the pressure body to the sidewall. This effect is discussed in the RESULTS AND ANALYSIS section under Bodies Alone. There were, also, unwanted interference effects on the pressure body due to the sting apparatus of the force body while the pressure body was in the zone of influence of this sting apparatus. Shown in figure 9 is the pressure body with a hatched zone. Any time the sting apparatus of the force body passed within this zone, unwanted disturbances were caused in the pressure data. Configurations where the sting apparatus was located in this zone, or very close to it, were noted throughout the test, and the corresponding disturbed pressure data was eliminated during the data reduction after the test.

RESULTS AND ANALYSIS

In this section, the experimental results are discussed and comparisons are made with each of the theoretical prediction techniques: Lighthill, PAN AIR, and Far-Field Wave Drag (FFWD). The wave drag of the bodies alone (interference-free) will, first, be discussed. Next, the different types of interference effects will be analyzed. This will lead to a discussion of wave drag versus relative position of the bodies and then wave drag versus shock location. Finally, some considerations involving skin friction drag will be made.

Throughout this section, the data will be presented in the following ways: pressure distributions; comparisons of D_w/q (wave drag divided by dynamic pressure) for the bodies alone; and comparisons of $\Delta D_w/D_{w_0}$ (change in wave drag divided by the interference-free wave drag) for the different configurations. There are restrictions on the types of comparisons that can be made due to the type of data obtainable, not only from the experiment, but from each of the theoretical techniques. Below is a summary of the type of experimental data gathered and the type of output data from the theoretical programs.

		30" Pressure Body		Cut-off Force Body
Experiment	i)	Pressure distributions	i)	Wave drag obtained from the balance measurements
	ii)	Wave drag obtained from integrated pressure distributions		

27

(Cont.)	30" Pressure Body	Cut-off Force Body

PAN AIR   i)   Pressure distributions of both bodies

           ii) Wave drag (as well as other force data) for both
               bodies obtained from integrated pressure distributions.

FFWD   Outputs the wave drag of the entire configuration only

Lighthill   Outputs the pressure distribution and wave drag only for
            each body alone (interference-free)

Bodies Alone

Before considering the interference effects between the bodies, comparisons will be made between experiment and theory for the wave drag of the bodies alone (interference-free). Here, a comparison is made between the experiment, Lighthill, and PAN AIR, of the pressure distribution for the 30" pressure body. Also, wave drag comparisons between the experiment, Lighthill, PAN AIR, and FFWD of both bodies are made.

Consider the pressure distribution of the 30" body, outside of the influence of the cut-off force body, as shown in figure 10. Note the good agreement between the experiment, Lighthill, and PAN AIR on the front end of the body. The deviation of the experimental pressure distribution from that of the theory on the back of the body is due to the interference from the sidewall blade mount. As shown in figure 10, the x location at which interference first occurs can be predicted by sketching a Mach line from the blade-body intersection across the body.

Using PAN AIR, an adjustment was sought for this unwanted interference due to the sidewall blade mount. A 30" body with a blade mount at x = 15" was modeled in PAN AIR, and the resulting pressure distribution is compared

to the experimental results in figure 11. Note, that for $\bar{\theta} = 90^\circ$, PAN AIR predicts a similar effect as the experimental data; however, the shock location predicted by PAN AIR is displaced rearward. For $\bar{\theta} = 0^\circ$, a similar result is seen with the shock location predicted by PAN AIR displaced further rearward. The further the shock must wrap around the body, the more distorted the PAN AIR pressure distribution becomes. This is due to the spreading of any effect from panel to panel by PAN AIR. It is expected that a denser distribution of panels would do a better job of predicting the pressure distribution; however, the number of panels used in this case is very close to the maximum panel size allowed by PAN AIR at this time. Thus, the PAN AIR prediction of the 0° pressure line is more distorted than its prediction of the 90° pressure line. Therefore, a correction for the 90° pressure line will be sought, since PAN AIR will do a better job predicting the 90° pressure line than the 0° pressure line. Note that for an interference-free body at zero-degrees angle of attack, both the 90° and 0° pressure lines should read the same pressure. Thus, the 90° pressure line will be corrected due to the presence of the blade; then the 0° pressure line will be adjusted using the new 90° pressure line. This will yield an array of ΔC_p for both pressure lines. Each array of ΔC_p will be used as the correction, due to the presence of the blade, for its respective line of pressure. These arrays of ΔC_p will be used later in the analysis of the interference effects.

To get a better prediction by PAN AIR of the pressure distribution for the experimental body with blade, the blade was moved forward to the $x = 13.5"$ location in the PAN AIR model. This was done in order to match

the shock location shown by PAN AIR with that shown by the experiment. The resulting PAN AIR pressure distribution for the 90° pressure line is shown in figure 12 compared with the original experimental pressure distribution for the 90° pressure line. Note the good agreement between PAN AIR and experiment.

We now have the needed information to correct the pressure distribution due to the blade interference. This procedure, outlined in figure 13, consists of first correcting the 90° pressure line and then correcting the 0° pressure line using the new 90° pressure line. In this way, two arrays of ΔC_p will be obtained. Each array will be used to correct its respective line of pressure for the presence of the blade. In figure 13, step A, the 90° line of pressure is corrected, using the 0° line of pressure, up to x = 20", since the effect of the shock due to the blade doesn't appear in the 0° pressure line until x = 20.5". In step B, the 90° pressure distribution for the rest of the body is corrected by adding the difference in C_p between the PAN AIR – (body alone) pressure distribution and the PAN AIR – (body with blade at x = 13.5") pressure distribution to the experimental 90° pressure line. This results in the corrected 90° pressure line shown. The 0° pressure line is then adjusted starting at x = 20.5", using the 90° pressure line. Figure 14 shows each pressure line before and after the correction. The difference in C_p between the corrected and original lines of pressure form two arrays of ΔC_p. These arrays of ΔC_p, each added to its respective line of pressure, increase D_w/q of the body by .008 (5.6%).

There was a small difference in the experimental pressure distribution and corresponding wave drag of the 30" body depending upon its forward or aft location in the test section. The previous experimental pressure distributions shown in figures 10 through 14 were of the 30" body located in the forward test section location. Figure 15 compares both the 0° and 90° lines of pressure for both locations of the 30" body. Note the difference in the pressure distributions resulting in about a 7 percent difference in D_w/q. One possible explanation for this effect is that it is due to the physical location of the body in the test section rather than random type error in measurement. This can be seen from Table II, by noting the repeatability of D_w/q measured for the body in the forward location of the test section. D_w/q for the 30" body alone varied less than 1 percent while it was located in the front of the test section. When the 30" body was tested alone in the aft location of the test section, the value of D_w/q increased by about 7 percent. In the following sections, comparisons will be made between experiment and theory of the change in wave drag from the noninterference case, thus, avoiding the problem of tunnel location of the 30" body.

Figure 16 contains a comparison of D_w/q between experiment and theories for the bodies alone. Note the good agreement between PAN AIR, Lighthill, and experiment. However, FFWD overestimated D_w/q by about 19 percent for the 30" body and by 24 percent for the cut-off body.

This large difference between FFWD and experiment for the noninterfering bodies can be analyzed on the basis of some previous experimental results of bodies alone. Reference 23 contains some experimental results

of cut-off Sears-Haack bodies with $\ell/d_{max} = 7$, 10, and 13 at Mach numbers ranging from 0.6 to 4.0. After modeling these bodies in the Lighthill method, PAN AIR, and FFWD, the results were compared to experimental values from reference 23. Figure 17 shows a comparison between theory (PAN AIR, FFWD, Lighthill) and experiment of C_{D_w} versus Mach number for each of the three bodies. Note that as ℓ/d_{max} is increased, all theories agree better with the experiment. Consider the body with $\ell/d_{max} = 13$, which is about the same fineness ratio as the bodies used in this study. At Mach 2.7, PAN AIR seems to do a good job predicting the wave drag of this body; however, FFWD appears to overestimate the drag by about 25 percent. Thus, the high prediction of D_w/q by FFWD for the 30" body and the cut-off body is related to the low fineness ratios of the bodies. One would expect FFWD to continue to improve with higher fineness ratio bodies, such as those normally used in supersonic cruise vehicles. In the experiment, the bodies used had about as high a fineness ratio as possible and, yet, produce enough drag to be measured to the needed accuracy.

Also shown in figure 16 are the estimates of D_w/q by FFWD and PAN AIR for a body of twice the volume and same length ($\ell/d_{max} = 10.3$). Note the large difference in the estimates of D_w/q by the two theories. This is due to the very low fineness ratio of the body (see figure 17). In general, according to slender-body theory (ref. 22), the drag of a Sears-Haack body can be written as:

$$D_w = \frac{64 V_b{}^2 \rho_\infty V_\infty{}^2}{\Pi \ell^4} \tag{14}$$

or
$$D_w/q = \frac{128 V_b{}^2}{\Pi \ell^4} \tag{15}$$

Then, using equations (15) and (9b), the wave drag coefficient (based on the maximum cross-sectional area) can be written as:

$$C_{D_w} = \frac{24 V_b}{\ell^3} \tag{16}$$

Thus, if the volume of the body is doubled, while the length remains constant, C_{D_w} is also doubled while D_w/q increases four times. Note that C_{D_w} is based on the maximum cross-sectional area of the body which is different for the two bodies being compared (the body with twice the volume has a maximum cross-sectional area twice that of the other body). The experimental data in figure 17 supports the conclusion that doubling the volume of a body while holding the length constant doubles the value of C_{D_w}. Doubling the volume, while keeping the length constant, of a body with an ℓ/d_{max} of 10 yields a body with an ℓ/d_{max} of about 7. Notice, that the values of C_{D_w} for the body with $\ell/d_{max} = 7$ are approximately double the C_{D_w} values for the body with $\ell/d_{max} = 10$. Therefore, a reasonable estimate of D_w/q for a body with twice the volume of the 30" body would be $(4 \times .15)$ .60 in^2. Thus, a twin-body configuration without any interference effects has approximately half the wave drag of a single body with equal volume and same length.

Interference Effects, General Types

Before analyzing actual configurations, consider some of the general types of interference effects. In these cases, a given body and

the effect of a shock impingement on that body will be discussed. All of the pressure distributions shown are taken from experimental data at $\theta = 0^{\circ}$.

First, an unfavorable shock effect consisting of a shock impingement on the forward-facing slope (or positive slope) of the body will be considered. Figure 18 shows a typical change in the pressure distribution due to the influence of a shock striking the front of the body. Note, at the point of shock impingement the fluid is compressed, causing an increase in pressure, after which expansion of the fluid takes place. Thus, the effect on the pressure distribution is an increase in pressure on the forward end of the body (where the slope of the body surface is positive) and a decrease in pressure on the back end of the body (where the slope of the body surface is negative). Both of these changes in the pressure distribution result in an increase in drag of the body and, hence, an unfavorable effect.

A shock impingement at the back end of the body produces a more favorable effect. Figure 19 shows the change in the pressure distribution due to a shock striking the aft end of the body. Again, at the point of shock impingement, the fluid is compressed and then expanded. The effect is an increase in pressure on the back end of the body resulting, more favorably, in a decrease in drag.

Finally, consider the effect of a shock passing in front of the body. Here, there are two cases to consider. The first is shown in figure 20, where the shock passes a considerable distance in front of the body. Note, the decrease in pressure on the front end of the body

at $\theta = 0^o$. This decrease in pressure yields the favorable effect of reducing the drag. As the shock moves closer to the body, as shown in figure 21, an unfavorable effect takes place. The pressure is increased on the front end of the body for $\theta = 0^o$ and decreased on the back end of the body resulting in increased drag. The effect on the other lines of pressure for these two cases will be shown later.

Some of the basic types of interference and their effect on the drag of the body have been considered. It should be noted, however, that in some cases more than one effect, at one time, can occur. This is due to the presence of the nose shock and tail shock. Also, for very close separations, shock reflections must be considered. These different interference effects will be referred to throughout the discussions of wave drag versus relative position of the bodies.

Wave Drag Versus Lateral Separation

Consider the change in wave drag when separating the bodies laterally. In this case, only the effect of the nose shock (and possibly its reflections) need be considered. See figure 22 for the cases considered. First, some of the experimentally measured pressure distributions will be discussed (figures 23, 24, 28 and 29) and compared to the PAN AIR pressure distributions (figures 26, 27, 30 and 31). Finally, comparisons between experimental and theoretical wave drag results will be made for each of the bodies separately and for the total configuration (figures 32, 33, and 34).

To illustrate the effect of the nose shock (and possibly its reflections), figure 23 contains pressure distributions for different

separations at different values of θ. Figure 23(a) shows a pressure distribution for SEP/ℓ = .50, an interference-free case (see figure 22). Thus, no effects from the other body are seen in either pressure distribution. The effect seen at the tail end of the body is due to the blade support, which is discussed in the Bodies-Alone section. It should be noted that the blade support effect is contained in all the pressure distributions shown in figures 23 through 27. In figure 23(b), as the bodies are moved to the closer SEP/ℓ of .40, the shock now appears at the tail end of the body. As the bodies are moved closer, still, as in figures 23(c), 23(d), and 23(e), the shock moves forward on the body. Consider figure 23(d) as an example demonstrating the shock wrapping around the body. Note, that as the shock spreads around the body, the location of the shock moves rearward and its effect is diminished. For θ = 1.9°, in figure 23(d), the shock is located at about x = 12" and causes a change in C_p of about .04 at the peak. As θ is increased to 71.1°, the shock location has moved rearward to approximately x = 14" with a smaller change in C_p of about .02 at the peak. As the shock wraps even further around the body, to a θ of 161.1°, its effect is located even further rearward and is very small. Figures 23(b), 23(c), and 23(e) also demonstrate this effect.

Figure 23(e) shows the existence of a shock reflection. This shock reflection is a result of the nose shock of the 30" body reflecting off the cut-off body (see figure 22). Note, that the reflected shock, which wraps around the body yielding a similar effect to the pressure distribution as discussed above, is initially much weaker than the nose shock

(it has less of an effect on the pressure distribution). This reflected shock is weaker because it travels a further distance than the nose shock and, also, because it is reflected. Consider figure 24, where pressure distributions, for very close to constant θ (θ = 1° to 3°), of different separations are given. Note, as shown in figures 25(a), and 25(b) that as the separation distance is increased (the distance the shock travels is increased), the change in C_p due to the shock decreases. Note, also, that the reflected shock has less effect on the pressure distribution than a shock that is not reflected and travels the same distance. Thus, in discussing some of the effects of the shock, it has been demonstrated that as the shock wraps around the body it moves rearward and its effect is diminished. It has also been shown that a shock is weakened the further it travels and, also, when it is reflected.

Before considering the actual change in wave drag resulting from these shocks, figure 26 shows a comparison between PAN AIR and experiment of some of the more interesting pressure distributions. Consider, first, figure 26(a) where pressure distributions are given for SEP/ℓ = .300. Note how PAN AIR agrees with the experiment fairly well, including the magnitude of the shock disturbance; however, its prediction of the actual location of the shock seems to be displaced. This is due to the prediction of the shock path using the Mach line by PAN AIR. PAN AIR's prediction of shock location gets better as the bodies get closer together and the distance the shock travels decreases (figure 26(b) and 26(c)). It might be possible to adjust PAN AIR for this difference in shock location as shown in figure 27. Here the PAN AIR pressure distribution for

SEP/ℓ = .267 shows good agreement in shock location with the experimental results for SEP/ℓ = .300. Also, shown in figures 26(a), 26(b), and 26(c), is that PAN AIR's pressure distribution prediction tends to become worse as the shock wraps around the body. As discussed in the Bodies-Alone section, PAN AIR's prediction of the effect of the shock as it wraps around the body is highly dependent on panel density; and, with the current total panel number limitations, the PAN AIR model generated uses close to the maximum number of panels allowed. One more comparison to consider might involve the shock reflection shown in figure 26(c). PAN AIR seems to do a fair job in predicting the existence of the reflected shock; however, since this shock has travelled further than the nose shock from the force body, PAN AIR misses in predicting its location.

Using the blade correction described in the Bodies-Alone section, the pressure distributions contained in figures 23, 24, 26, and 27 were adjusted and are shown in figures 28, 29, 30 and 31, respectively. Making this adjustment assumes that the total effect from two different shocks (from two different sources) is the sum of each effect individually. As can be seen from the pressure distributions in figures 30 and 31, this assumption seems to yield good agreement between experiment and PAN AIR on the back end of the body. The same conclusions drawn from figures 23 through 27 can now be seen from figures 28 through 31 without the effect due to the blade complicating the pressure distribution.

Figures 32 through 34 show the resulting changes in wave drag of the bodies as they are separated. In all three figures, $\Delta D_w / D_{w_0}$ (the change in wave drag from the noninterference case divided by the wave drag of the

noninterference case) is plotted against the separation of the bodies in body lengths (ℓ = 30"). Figures 32 and 33 show the effects on the 30" body and cut-off body, respectively; while figure 34 combines the two bodies to show the effect on the entire configuration. Remember, when considering figures 32 through 34, that the wave drag of the 30" body is obtained by integrating the proper component of the pressures, while the wave drag of the cut-off body is obtained from force data measured by the balance (see the WIND TUNNEL and DATA REDUCTION sections).

By considering figure 24 (or figure 29), the resulting experimental wave drag trends in figures 32 through 34 can be understood. Consider, firstly, the trend shown by the experimental data of figure 32 in conjunction with figure 24. Starting all the way to the right of figure 32 at SEP/ℓ = .50, an interference-free case (see figure 22), there is no change in the wave drag. As the bodies are moved closer together, at SEP/ℓ = .40, the shock is now impinging at the rear end of the body (figure 24) causing the wave drag to decrease (see the section on the Interference Effects, General Types) as shown in figure 32. As the bodies move still closer together until SEP/ℓ = .30, the shock impinges on the body where it has its most favorable effect (see both figure 24 and 32). Moving the bodies closer together causes the shock to progress forward on the 30" body and the wave drag to rise. At SEP/ℓ = .20 the shock location has moved just forward of the center of the body (see figure 24) to the positive slope of the body; this causes an increase in the drag. As the bodies are moved even closer together, the shock continues to move forward on the 30" body and to hit a greater sloped

surface causing a further increase in wave drag. The trend depicted in figure 33 can be explained similarly; however, since the body is now cut off at the back, the bodies must be moved slightly closer together before shock impingement on the back end of the cut-off body occurs.

In all three figures (32 through 34), comparisons are made between both PAN AIR and FFWD theories with experimental data. Both PAN AIR and FFWD seem to do a good job in predicting the areas of favorable interference and the changes in wave drag associated with the relative locations of the bodies. Notice, however, that the theoretical trends seem to be shifted slightly to the left of the experimental trends. This is due to the prediction of the shock path using the Mach line by PAN AIR, and the use of Mach lines in calculating the area distributions by FFWD theory. In each of the figures 32, 33, and 34, the PAN AIR and FFWD curves have been adjusted due to this difference in shock path and Mach line (more for the larger separations and less as the bodies get closer together). The agreement between the experiment and both adjusted theories is very good. For the closer separations, PAN AIR seems to do a slightly better job than FFWD in predicting the drag of the 30" body and the entire configuration. Note that when considering just lateral separation of these bodies, the optimum configuration is at approximately a SEP/ℓ of .30 resulting in about a 12.5 percent decrease in wave drag.

The summary of the type of experimental data gathered and the type of output data from the theoretical programs, given at the beginning of the RESULTS AND ANALYSIS section, shows that FFWD outputs only the wave drag of the entire configuration. However, comparisons were just

examined, between FFWD and experiment, of the wave drag of each of the bodies seperately versus SEP/ℓ. Thus, wave drag estimates of each of the bodies separately versus SEP/ℓ must be obtained from FFWD. These estimates were obtained in the following manner. The total wave drag, as predicted by FFWD, of the 30" body and the cut-off body under the influence of each other (configuration 1), D_{w_1}, can be written as:

$$D_{w_1} = D_w(30)_1 + D_w(co)_1 \tag{17}$$

where $D_w(30)_1$ is the wave drag of the 30" body under the influence of the cut-off body and $D_w(co)_1$ is the wave drag of the cut-off body under the influence of the 30" body. Next, the wave drag is obtained from FFWD of two twin 30" Sears-Haack bodies, D_{w_2}, each identical to the 30" pressure body of the experiment (configuration 2), versus SEP/ℓ. Then

$$D_{w_2} = D_w(30)_2 + D_w(30)_2 \tag{18}$$

where $D_w(30)_2$ is the wave drag of the 30" body under the influence of the 30" body. Thus,

$$D_w(30)_2 = \tfrac{1}{2} D_{w_2} \tag{19}$$

Next, assume that the wave drag of the 30" body, at a given SEP/ℓ, is the same in both configurations 1 and 2. In other words, that the wave drag of the 30" body under the influence of an identical 30" body, $D_w(30)_2$, is the same as the wave drag of the 30" body under the influence of the cut-off body, $D_w(30)_1$, at any given SEP/ℓ. This assumption can be written as:

$$D_w(30)_1 = D_w(30)_2 \qquad\qquad (20)$$

This is a valid assumption, when considering just separation of the bodies, since only the nose shock from the other body is influencing the 30" body, and this nose shock will be the same whether it originates from an identical 30" body or the cut-off body. Then, from equations (19) and (20)

$$D_w(30)_1 = \tfrac{1}{2}\, D_{w_2} \qquad\qquad (21)$$

Finally, from equations (23) and (27) the following relation can be written:

$$D_w(co)_1 = D_{w_1} - \tfrac{1}{2}\, D_{w_2} \qquad\qquad (22)$$

Thus, equations (21) and (22) give, at a given SEP/ℓ, the wave drag of the 30" pressure body under the influence of the cut-off body and the wave drag of the cut-off body under the influence of the 30" pressure body, respectively, in terms of data output from FFWD.

When considering figures 32, 33, and 34, recall that in the Bodies-Alone section FFWD overestimated D_w/q of each of the bodies alone due to the low fineness ratio bodies used. Thus, the actual wave drag of the bodies in mutual interference will also be overestimated by FFWD; however, the percentage change in wave drag predicted by FFWD of the bodies in mutual interference agrees very well with theory as shown in figures 32, 33, and 34.

Thus, the resulting trends in wave drag versus separation of the bodies and the effectiveness of each of the theories in predicting these

trends have been discussed. It has been shown that the wave drag is greater than or less than the noninterference case when the shock impingement is located on the forward or aft part of the body, respectively. When considering just separation of the bodies, the optimal configuration occurs at a SEP/ℓ of about .30 resulting in a 12.5 percent reduction in wave drag. Also shown was that both PAN AIR and FFWD predict these areas of favorable interference, including the magnitude of the wave drag change, quite well. However, when both theories were adjusted due to the difference between the Mach line and shock path, they agree even more closely with the experimental results.

Wave Drag Versus Longitudinal Skew at Two Different Separations

In this section, the effect of skew (or longitudinal displacement) on the wave drag of the bodies will be examined. Again, experimental results will be shown with comparisons made between the experimental data and the data predicted by the theoretical techniques (PAN AIR and FFWD). This analysis will be done at SEP/ℓ = .40 and SEP/ℓ = .20.

For SEP/ℓ = .40, the setup is shown in figure 35 with experimental and theoretical results shown in figures 36 through 41. Figure 36 shows the experimental pressure distributions, at θ = 0°, for eight different skews. Figure 37 shows experimental pressure distributions around the body for SKEW/ℓ = -1.2. Figure 38 contains pressure distribution comparisons between experiment and PAN AIR for SKEW/ℓ = -.60, -1.00, -1.20, and -1.40. Comparisons between both theories and experiment of $\Delta D_w/D_{w_0}$ versus SKEW/ℓ for the 30" body, the cut-off body, and the entire configuration are shown in figures 39, 40 and 41, respectively.

To understand the trend shown by the experimental data in figure 39 ($\Delta D_W/D_{W_O}$ versus SKEW/ℓ, for SEP/ℓ = .40, of the 30" body), consider figures 36 and 39. For a SKEW/ℓ of 0, the wave drag is decreased slightly from the noninterference case (figure 39) due to the nose shock of the cut-off body impinging on the extreme tail end of the 30" body (figure 36). As SKEW/ℓ becomes more negative, the nose shock impingement progresses forward on the 30" body. At a SKEW/ℓ of -.20, a local minimum in the wave drag of the 30" body is reached (figure 39). As the force body is displaced further forward (SKEW/ℓ becomes more negative), the shock moves forward on the body and causes the wave drag to increase. At a SKEW/ℓ of -.60, the shock has moved to the forward facing slope of the 30" body increasing its drag above that of the noninterference case. The shock location on the front part of the body, resulting from a SKEW/ℓ of -.80, yields a maximum increase of about 24 percent in the wave drag of the 30" body. As the cut-off body is moved forward to a SKEW/ℓ of -1.00, the nose shock from the cut-off body passes just in front of the 30" body. This causes the pressure to be elevated near the nose of the 30" body. Not shown in the experimental data is a weak shock originating from the tail of the cut-off body striking the back of the 30" body when SKEW/ℓ = -1.00. This effect was masked by interference from the model support apparatus (this is why some of the symbols are flagged in figure 39). To get an idea of the effect of the tail shock, see the pressure distribution predicted by PAN AIR at a SKEW/ℓ of -1.00 in figure 38. The effect of this weak shock striking the back end is to decrease the drag of the 30" body. Thus, at a SKEW/ℓ of -1.00 there are two effects

counteracting each other. As the cut-off body is moved further forward, to a SKEW/ℓ of -1.20, depression of the pressure on the front end of the 30" body for $\theta = 0^\circ$ occurs (see figure 36(b)). However, as this effect spreads around the body the depression of pressure near the nose of the body is not as great (see figure 37). This depression of pressure near the nose, combined with the favorable tail-shock effect (according to PAN AIR, figure 38) decreases the drag of the 30" body. Note, at a SKEW/ℓ of -1.40 the tail shock now yields an unfavorable effect according to PAN AIR (see figure 38); however, further depression of the pressure on the nose of the body has occurred. This results is an overall favorable effect on the drag of the 30" body (consider the general trend shown by experiment and theory in figure 39). When considering figure 39, a comment about the two local minimums of the general trend should be made. Consider the general trend shown by the experiment and theory, even though some of the experimental data contains interference due to model support apparatus. The first local minimum, at SKEW/ℓ = -.20, is a result of the nose shock from the cut-off body striking the tail of the 30" body. The second local minimum, at SKEW/ℓ = -1.20, is a result of the nose shock of the cut-off body passing in front of the 30" body causing a depression of the pressure on the front of the body. These are the two basic favorable effects discussed in the section entitled Interference Effects, General Types.

A very similar curve is shown in figure 40 for $\Delta D_w/D_{w_0}$ of the cut-off body versus positive SKEW/ℓ. However, due to the cut-off body being truncated at the rear, any effect due to a change in pressure on

the tail end of the cut-off body is smaller than the similar effect on the 30" body. This is due to the cut-off body having less negative (or rearward) facing surface area. Also, any percentage change in wave drag due to a change in pressure on the front end of the cut-off body is larger than the similar effect on the 30" body. This is simply due to the cut-off body having less total wave drag than the 30" body. Thus, similar changes in wave drag will yield a larger percentage change in wave drag for the cut-off body than for the 30" body.

Combining the data of figures 39 and 40 yields the results shown in figure 41. Here the fractional change in wave drag of the entire configuration versus SKEW/ℓ at a SEP/ℓ of .40 is plotted. Note how the curve is nearly symmetric with respect to the vertical axis due to the similar effects on each body for different directions of SKEW. However, the difference between the two halves of the curves results from one of the bodies being cut off. Note, that skews of positive and negative two-tenths of a body length yield about a 4 percent and 6 percent decrease in wave drag of the configuration from the noninterference case, respectively. The larger skews of positive and negative 1.4 body lengths result in larger reductions in wave drag from the noninterference case. (Note that at the large negative values of SKEW/ℓ the experimental results contain interference. However, the theoretical results support the last conclusion.)

Figure 38 shows a comparison between experiment and PAN AIR for four different skews at a SEP/ℓ of .40 and constant θ of 0°. The first comparison, at a SKEW/ℓ of -.60, shows the existence of a nose shock

impinging on the body at about x = 9". This comparison is similar to
ones shown in the previous section where PAN AIR agrees with the experi-
mental pressure distribution quite well including the magnitude of the
pressure peak caused by the shock. Consider the other three pressure
distribution comparisons between experiment and PAN AIR (SKEW/ℓ = -1.00,
-1.20, -1.40) where changes in the experimental pressure distribution
near the nose of the 30" body had occurred. PAN AIR seems to do a fair
job in predicting these changes. Notice, however, that some experimental
pressures are deleted due to interference of the model support apparatus.

Note the good agreement between the theories and experiment,
especially between the adjusted theories and experiment, in figures 39,
40, and 41 where $\Delta D_w/D_{w_0}$ is plotted against SKEW/ℓ. Again, both
theories predict the same areas of favorable interference. Good agree-
ment between the theories and experiment is also seen when comparing the
magnitude of the fractional changes in wave drag.

An analysis similar to the one just discussed can be made at a
SEP/ℓ = .20. The general test setup is shown in figure 42. A series
of experimental pressure distributions is shown in figures 43 and 44,
while comparisons between PAN AIR and experiment of various pressure
distributions are shown in figures 45 and 46. Comparisons between the
theories and the experiment of $\Delta D_w/D_{w_0}$ versus SKEW/ℓ for the 30" body,
the cut-off body, and the entire configuration are shown in figures 47,
48, and 49, respectively.

Figures 43 and 44 contain experimental pressure distributions of a
similar type as discussed previously. Figure 43 shows how the pressure

distribution, for θ 0° and SEP/ℓ = .20, of the 30" body changes as SKEW/ℓ varies from .50 to -.30. Again, as the cut-off body is moved forward (from SKEW/ℓ = .50 to -.30) the shock originating from its nose progresses forward on the 30" body. In figure 44, the movement of the shock around the body at a SKEW/ℓ of -.30 is depicted. Again, as the shock wraps around the body, it moves rearward and is diminished.

Shown in figures 45 and 46 are pressure distribution comparisons between experiment and PAN AIR. Figure 45 shows comparisons of pressure distributions for $\theta \approx 0^\circ$ at SKEW/ℓ = .30, 0, and -.30. In figure 46 are pressure distribution comparisons at four different values of θ for SKEW/ℓ = .30. As mentioned before, agreement is quite good between PAN AIR and experiment except that PAN AIR displaces the location of the shock rearward.

The resulting changes in wave drag shown in the experiment and predicted by the theoretical techniques are illustrated in figures 47, 48, and 49. In each case, $\Delta D_w/D_{w_0}$ versus SKEW/ℓ is plotted. In all three plots, the flagged symbols mean unwanted external interference from the sidewall blade was present. Note the good agreement between PAN AIR and experiment in figures 47, and 48. In both figures 47 and 48, when PAN AIR is corrected due to its shock location shift, it agrees much better with experimental data. Comparisons with both theories and experiment are shown for the entire configuration in figure 49. Note that PAN AIR and FFWD agree with each other quite well. Both, also, predict the experimental trends quite accurately. The corrected PAN AIR

curve in figure 49 is taken from the weighted average of the corrected PAN AIR curves in figures 47 and 48.

To get a better understanding of the unwanted external blade interference, consider figure 50. Here, $\Delta D_W/D_{W_O}$ is again shown versus SKEW/ℓ for the cut-off body at a SEP/ℓ of .20. Instead of giving just the average experimental values, the values for each batch are given. Note how each batch agrees very closely with the other batches until interference from the blade of the 30" body is present. The spread in the experimental values after a SKEW/ℓ of .40 is due to the difference in blade interference for each batch. At each batch, the cut-off body is at a different Δ below the 30" body. Thus, the interference from the blade will be different for each batch.

Wave Drag Versus Shock Location

The drag data for various separations and skews may be analyzed to show a simple dependence of $\Delta D_W/D_{W_O}$ on both the strength and location of the shock. In figure 51 values of $\Delta D_W/D_{W_O}$ from the experiment and PAN AIR are plotted versus the shock location on the 30" body in body lengths. The SHOCK LOC, as referred to in the figures, is defined as the intersection of the cut-off body nose shock and the 30" body centerline. Note, that the general trend depends on the shock location rather than the given SEP/ℓ. However, for the closer separation (SEP/ℓ is smaller) the effect of the shock is greater causing larger changes in wave drag. In other words, if the effect of the shock on the wave drag is favorable (for example SHOCK LOC/ℓ = .8), the decrease in drag will be greater for the closer separation since the shock is stronger for the closer separation.

Similarly, if the effect of the shock on the wave drag is unfavorable (for example, SHOCK LOC/ℓ = .15) the increase in wave drag will be greater for the closer separation.

Skin Friction Considerations

Up to this point, it has been shown that the existence of favorable interference effects between two bodies results in a decrease in wave drag compared to that for two interference-free bodies. In the Bodies-Alone section, the wave drag of a two-body system, interference-free, was shown to have half the wave drag of a single body of equal volume. However, as comparisons are made between this two-body system and a single body of equal volume, the skin-friction drag of each system must also be considered. In the Bodies-Alone section (using slender body theory), it was shown that:

$$\frac{D_w}{q} = \frac{128 \, V_b{}^2}{\Pi \ell^4} \tag{23}$$

For a single Sears-Haack body let

$D_w(1)$ = wave drag
$D_F(1)$ = skin friction drag
$D(1)$ = total drag

then,

$$D(1) = D_w(1) + D_F(1) \tag{24}$$

For a Sears-Haack body of twice the volume and same length let

$D_w(\text{twice})$ = wave drag of a body of twice the volume
$D_F(\text{twice})$ = skin friction drag of a body of twice the volume
$D(\text{twice})$ = total drag of a body of twice the volume

Then

$$D(\text{twice}) = D_w(\text{twice}) + D_F(\text{twice}) \tag{25}$$

Using equation (23)

$$D_W(\text{twice}) = 4 \, D_W(1) \tag{26}$$

Also, since the wetted area of this Sears-Haack body of twice the volume has increased by $\sqrt{2}$ over the original body, while the reference length has remained constant, use the following approximation for D_F (twice):

$$D_F(\text{twice}) = \sqrt{2} \, D_F(1) \tag{27}$$

Therefore:

$$D(\text{twice}) = 4D_W(1) + \sqrt{2} \, D_F(1) \tag{28}$$

For two isolated Sears-Haack Bodies, interference-free, let

$D_W(2)$ = wave drag of the system
$D_F(2)$ = skin friction drag of the system
$D(2)$ = total drag of the system

Since the bodies are interference free:

$$D_W(2) = 2D_W(1) \tag{29}$$

$$D_F(2) = 2D_F(1) \tag{30}$$

Therefore,

$$D(2) = 2D_W(1) + 2D_F(1) \tag{31}$$

Consider these two bodies in favorable interference, and let

$D_W(2^*)$ = wave drag of the two-body system with favorable interference

$D_F(2^*)$ = skin friction drag of the two-body system with favorable interference

$D(2^*)$ = total drag of the two-body system with favorable interference

Previously, a particular case showed a 12.5 percent reduction in wave drag of a two-body system with interference over a two-body interference-free system:

$$D_W(2^*) = .875 \, D_W(2) \tag{32}$$

Since

$$D_F(2*) = D_F(2) \tag{33}$$

then

$$D(2^*) = .875 \ D_W(2) + D_F(2) \tag{34}$$

$$= .875 \ [2D_W(1)] + 2D_F(1)$$

$$D(2^*) = 1.75 \ D_W(1) + 2D_F(1) \tag{35}$$

Thus, for a body of twice the volume

$$D(\text{twice}) = 4D_W(1) + \sqrt{2} \ D_F(1) \tag{28}$$

For a two-body system, interference-free

$$D(2) = 2D_W(1) + 2D_F(1) \tag{31}$$

For a two-body system in favorable interference

$$D(2^*) = 1.75D_W(1) + 2D_F(1) \tag{35}$$

For the Sears-Haack bodies of the experiment

$$D_F(1) \approx 2D_W(1) \tag{36}$$

using the T' method to calculate the skin friction drag (refs. 16, 17, and 18).

Therefore, equations (28), (31), and (35) become

$$D(\text{twice}) = 6.83 \ D_W(1) \tag{37}$$

$$D(2) = 6 \ D_W(1) \tag{38}$$

$$D(2^*) = 5.75 \ D_W(1) \tag{39}$$

Thus, according to equations (37), (38), and (39), a two-body system, interference-free, has 12 percent less total drag than a single body of equal volume. Also, if those two bodies interfere favorably (12.5 percent reduction in wave drag over the interference-free case) a 16 percent decrease in total drag occurs over that of a single body of equal volume.

Using experimental results where possible, the previous formulation can be summed up as follows:

	D_W/q	D_F/q	D/q	% decrease in D/q from body of twice volume
Single body (30")	.146	.311*	.457	
Body of twice volume (equal to total vol. of two-body system)	.584*	.440*	1.024	
Two-body system, interference-free	.292	.622*	.914	10.7%
Two-body system, 12.5% favorable interference	.256	.622*	.878	14.3%

(* obtained from theoretical techniques)

CONCLUDING REMARKS

Interest in multibody supersonic configurations exists due to their
large passenger capacity and their potential for a reduction in wave
drag resulting from favorable interference effects. As an initial study
of these multibody supersonic vehicles, an analysis was conducted of the
interference effects between two Sears-Haack bodies. The objectives of
this analysis were to better understand the interference effects between
the two bodies, determine the effectiveness of some theoretical tech-
niques in predicting these interference effects, and make comparisons of
both wave drag and total drag between a two-body system and a single
body of equal volume and the same length.

The study consisted of a wind-tunnel experiment and theoretical
analysis at Mach 2.7. One of the bodies was cut off at the back and
sting mounted, while the other body was mounted on the tunnel sidewall
with a blade. Force measurements were made on the cut-off body, and
pressure data was measured on the sidewall mounted body.

Various relative positions of the bodies were analyzed. Changes in
wave drag due to lateral separation of the bodies showed favorable
interference when a shock impinged on the back half of the body. This
favorable interference between the two bodies resulted in as much as a
12.5 percent reduction in wave drag over that of the two bodies,
interference-free. When studying the effects of longitudinal skew,
another favorable effect was seen. This favorable effect was due to the

nose shock of one of the bodies passing at about .2 to .4 body lengths
in front of the other body. This effect lowered the pressure on the
nose of the body and resulted in a decrease in wave drag of that body
over the noninterference case. The changes in wave drag for a particu-
lar body were shown to depend on both the location of the shock on the
body and the strength of the shock at the body.

To gain confidence in two theoretical techniques (PAN AIR, a near-
field panel method, and Far-Field Wave Drag, a method based on the
supersonic area rule) for predicting these interference effects, com-
parisons were made between them and experimental results. For the bodies
alone, good agreement was found between PAN AIR and the experiment in
comparisons of both pressure distributions and wave drag. Far-Field
Wave Drag, however, overestimated D_W/q of the bodies alone. This dif-
ference between FFWD and experiment of the bodies-alone wave drag was
found to be related to the low fineness ratio bodies used. Throughout
the analysis, pressure distribution comparisons and wave drag comparisons
were made between experiment and theory. PAN AIR pressure distributions
agreed fairly well with experimental pressure distributions, including
the magnitude of the shock disturbance. However, PAN AIR predicted the
location of the shock further downstream on the body due to its use of
the Mach line to describe the shock path. Both PAN AIR and Far-Field
Wave Drag did a good job in predicting the areas of favorable inter-
ference and the magnitude of the wave drag changes, associated with dif-
ferent relative locations of the bodies, shown in the experiment.
However, the theoretical trends were shifted slightly due to the use of

the Mach line rather than shock path by both theories. Adjusting the theoretical trends due to this shock-path difference resulted in better agreement between the theories and the experiment.

Drag comparisons were made between a two-body system and a single body of equal volume (and same length). These comparisons were based on experimental data supplemented, where necessary, by theoretical results. The single body had twice the wave drag of the two-body system, interference-free. One of the two-body configurations (SEP/ℓ = .30, SKEW/ℓ = 0) was shown to have 12.5 percent less wave drag than a two-body system, interference-free. Such favorable interference results in a two-body configuration having 56 percent less wave drag than a single body of equal volume. However, the skin friction drag of a two-body system is greater than that of a single body. Combining this large reduction in wave drag and this increase in skin friction of a two-body system yields a 14 percent decrease in wave drag of a two-body configuration with favorable interference over a single body of equal volume and the same length.

APPENDIX A

This appendix contains a comparison between a portion of the
experimental data taken from reference 5 and results from both the PAN
AIR and Far-Field Wave Drag (FFWD) programs. The portion of the
experiment of interest consisted of a wind-tunnel test of two identical,
interfering, parabolic bodies of revolution at Mach numbers ranging from
0.8 to 1.15, and at various separations. In the experiment, the wave
drag was calulated from pressure data obtained from one of the bodies.
The correlation was done only at Mach 1.15 since both the PAN AIR and
FFWD programs have speed regime limitations. (The FFWD program is
strictly supersonic; and PAN AIR cannot handle transonic flow.)   ·
Although Mach 1.15 is much lower than typical Mach numbers of interest
for the design of supersonic aircraft, this comparison gives an idea of
whether the theories are correctly predicting the actual physical
trends.

FFWD and PAN AIR models were generated and run at appropriate
separation distances for the identical bodies of figure 52. Full
bodies were defined as in figure 52, while part bodies were defined up
to the 12.42 cm station. Drougge, the experimentalist of reference 5,
defined the part body as the position up to where he felt flow
separation had not yet occurred.

Overall, the agreement between the theories and experiment is quite
good. Comparisons between the theories and experiment of wave-drag

coefficient versus separation for the full-body and part-body configurations are presented in figures 53 and 54, respectively. Due to the rather austere graphs in reference 5, detailed comparisons were not really possible; however, comparisons of the trends between both theories and experiment were very good.

Thus, it seems appropriate to conclude that FFWD and PAN AIR predict similar trends as shown in the limited, nondetailed experimental data at Mach 1.15 of reference 5. However, further experimental data is needed to support the twin-body concept.

REFERENCES

1. Hoffman, Sherwood: Bibliography of Supersonic Cruise Aircraft Research (SCR) Program from 1972 to Mid-1977. NASA RP-1003, 1977.

2. Hoffman, Sherwood: Bibliography of Supersonic Cruise Research (SCR) Program from 1977 to Mid-1980. NASA RP-1063, 1980.

3. Walkley, K. B.; Espil, G. J.; Lovell, W. A.; Martin, G. L.; and Swanson, E. E.: Concept Development of a Mach 2.7 Advanced Technology Transport Employing Wing-Fuselage Blending. NASA CR-165739, 1981.

4. Maglieri, Domenic J.; and Dollyhigh, Samuel M.: We Have Just Begun to Create Efficient Transport Aircraft. Astronautics & Aeronautics, Vol. 20, No. 1, February 1982, pp. 26-38.

5. Drougge, Georg: An Experimental Investigation of the Interference Between Bodies of Revolution at Transonic Speeds with Special Reference to the Sonic and Supersonic Area Rules. The Aeronautical Institute of Sweden Report 83 (Stockholm), 1959.

6. Gapcynski, John P.; and Carlson, Harry W.: A Pressure-Distribution Investigation of the Aerodynamic Characteristics of a Body of Revolution in the Vicinity of a Reflection Plane at Mach Numbers of 1.41 and 2.01. NACA RM L54-J29, 1955.

7. Friedman, Morris D., and Cohen, Doris: Arrangement of Fusiform Bodies to Reduce the Wave Drag at Supersonic Speeds. National Advisory Committee for Aeronautics Report 1236, 1955.

8. Rennemann, Conrad, Jr.: Minimum-Drag Bodies of Revolution in a Nonuniform Supersonic Flow Field, NACA TN-3369, 1955.

9. Houbolt, John C.: Why Twin Fuselage Aircraft? Astronautics & Aeronautics, Vol. 20, No. 4, April 1982, pp. 26-35.

10. Moore, J. W.; Craven, E. P.; Farmer, B. T.; Honrath, J. F.; Stephens, R. E.; and Meyer, R. T.: Multibody Aircraft Study (Vols. I and II). NASA CR-165829, 1982.

11. Whitcomb, Richard T.: A Study of the Zero-Lift Drag Rise of Wing-Body Combinations Near the Speed of Sound. NACA Rep. 1273, 1956. (Supersedes NACA RM L52H08)

12. von Karman, Th.: The Problem of Resistance in Compressible Fluids. R. Accad. d'Italia, Cl. Sci. Fis., Mat. e Nat., vol. XIII, 1935, pp. 210-265.

13. Whitcomb, Richard T.; and Sevier, John R., Jr.: A Supersonic Area Rule and an Application to the Design of a Wing-Body Combination with High Lift-Drag Ratios. NASA TR R-72, 1960. (Supersedes NACA RM L53H3 la)

14. Middleton, W. D.; and Lundry, J. L.: A System for Aerodynamic Design and Analysis of Supersonic Aircraft, Part 1 - General Description and Theoretical Development. NASA CR-2715, 1976.

15. Middleton, W. D.; and Lundry, J. L.: A System for Aerodynamic Design and Analysis of Supersonic Aircraft, Part 2 - Users Manual. NASA CR-2716, 1976.

16. Middleton, W. D.; and Lundry, J. L.: A System for Aerodynamic Design and Analysis of Supersonic Aircraft, Part 3 - Computer Program Description. NASA CR-2727, 1976.

17. Harris, Roy V., Jr.: An Analysis and Correlation of Aircraft Wave Drag. NASA TM X-947, 1963.

18. Magnus, Alfred E.; and Epton, Michael E.: PAN AIR - A Computer Program for Predicting Subsonic or Supersonic Linear Potential Flows About Arbitrary Configurations Using a Higher Order Panel Method, Vol. 1 - Theory Document. NASA CR-3251, 1980.

19. Tinoco, E. N.; Johnson, F. T.; and Freeman, L. M.: Application of a Higher Order Panel Method to Realistic Supersonic Configurations. Journal of Aircraft, Vol. 17, January 1980, pp. 38-44.

20. Lighthill, M. J.: General Theory of High Speed Aerodynamics. Higher Approximation. Vol. VI of High Speed Aerodynamics and Jet Propulsion, Ch. 8, Sec. E, W. R. Sears, ed., Princeton University Press, 1954.

21. Walkley, Kenneth B.: A Procedure for the Determination of the Effect of Fuselage Nose Bluntness on the Wave Drag of Supersonic Cruise Aircraft. NASA CR-145306, 1978.

22. Ashley, Holt; and Landahl, Marten T.: Aerodynamics of Wings and Bodies. Reading, Mass., Addison Wesley Publishing Company, 1965.

23. Harris, Roy V., Jr.; and Landrum, Emma Jean: Drag Characteristics of a Series of Low-Drag Bodies of Revolution at Mach Numbers from 0.6 to 4.0. NASA TN D-3136. 1965.

24. Jackson, Charlie M., Jr.; Corlett, William A.; and Monta, William J.:
Description and Calibration of the Langley Unitary Plan Wind Tunnel.
(Proposed NASA Technical Paper)

25. Bantle, Jeffrey W.: Experimental Investigation of the Interference
Effects Between Two Sears-Haack Bodies at Mach 2.7. (Proposed
NASA CR)

26. Sommer, Simon C.; and Short, Barbara J.: Free-Flight Measurements of
Turbulent-Boundary-Layer Skin Friction in the Presence of Severe
Aerodynamic Heating at Mach Numbers From 2.8 to 7.0. NASA TN-3391,
1955.

27. Liepmann, H. W.; and Roshko, A.: Elements of Gasdynamics. New York,
John Wiley and Sons, Inc., May 1967.

62
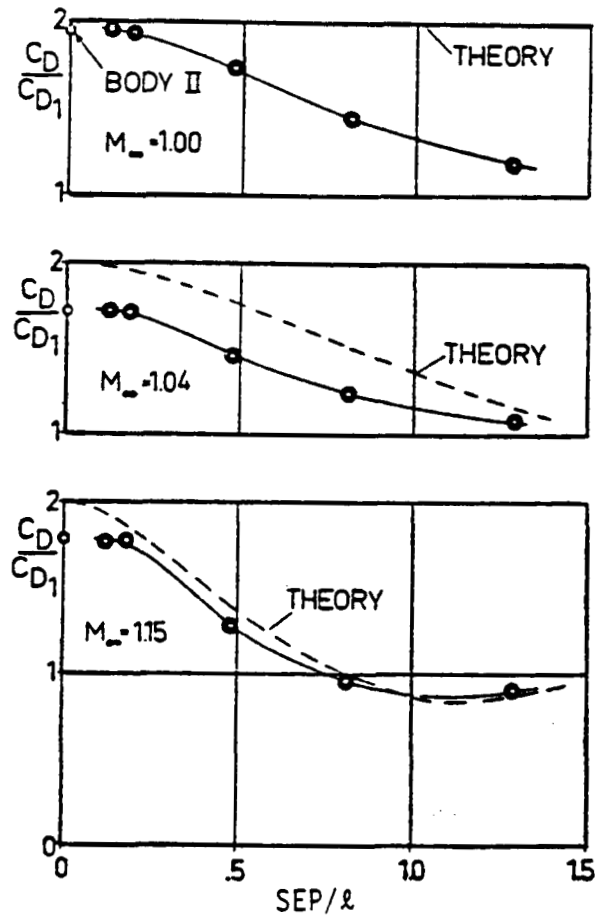
Figure 1.- Comparison between the theory and experiment of reference
5 for the wave drag ratio C_D/C_{D_1} (where C_D is the wave
drag coefficient of the body in the influence of the
other body and C_{D_1} is the wave drag coefficient of the
body interference-free) against the lateral seperation
in body lengths, SEP/ℓ, for M_∞ = 1.00, 1.04, 1.15.
(reproduction of figure 18, reference 5)
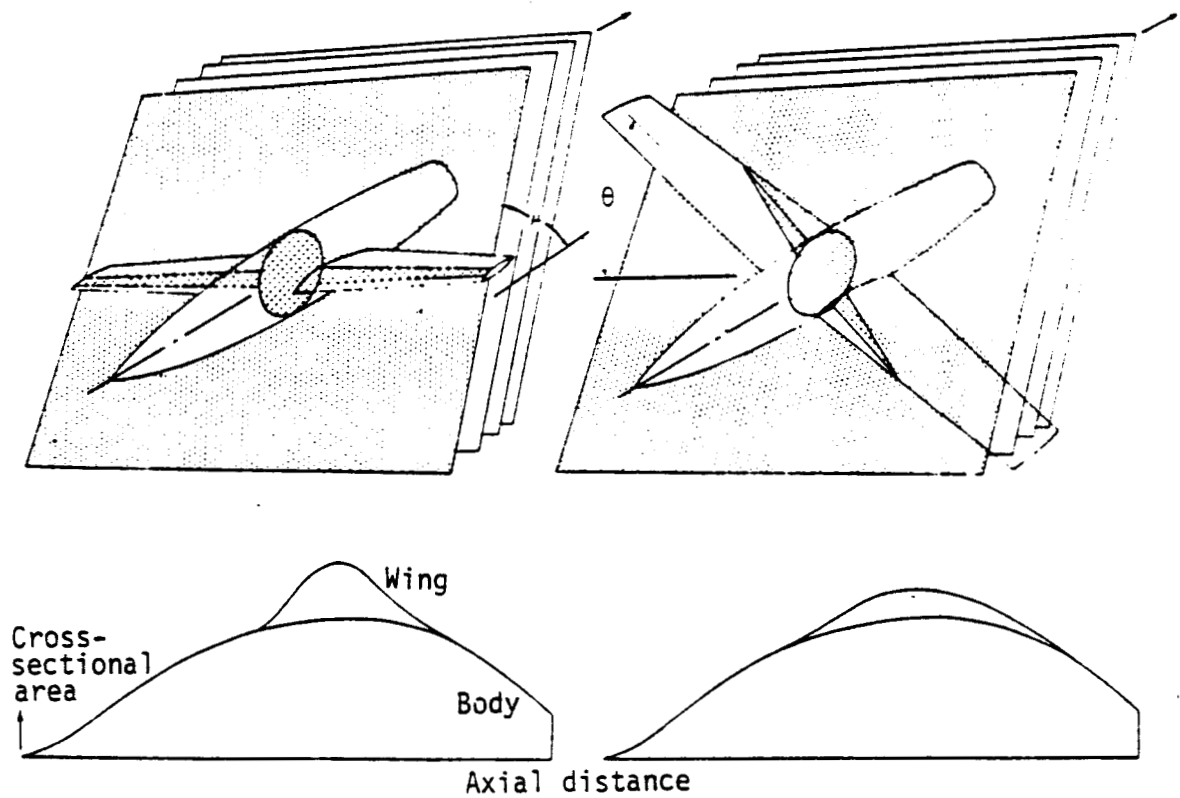
Figure 2- Procedure for determining area developments related to
wave drag at moderate supersonic Mach numbers.
(reproduction of figure 2, reference 15)
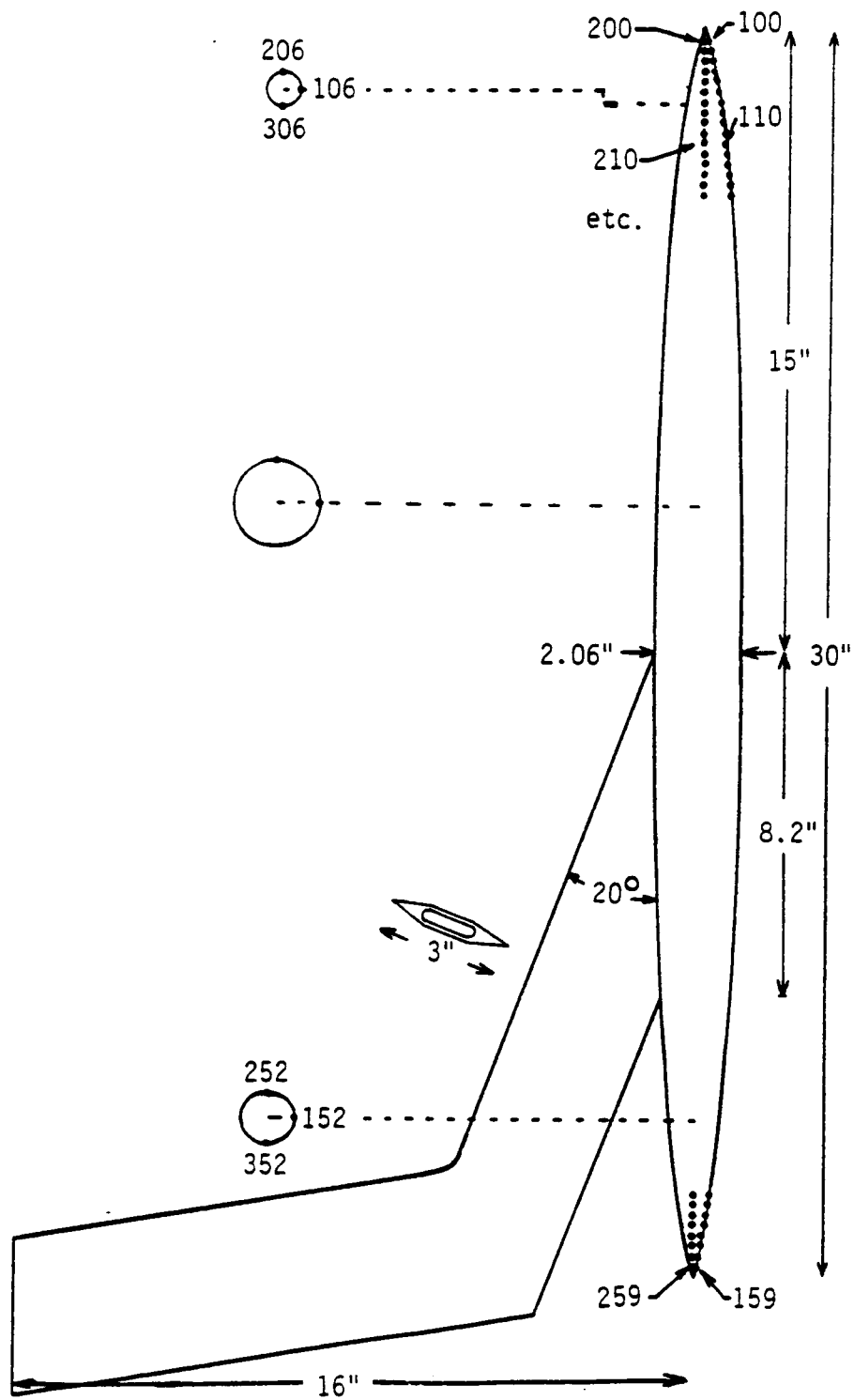
Figure 3.- 30" pressure body with blade support.
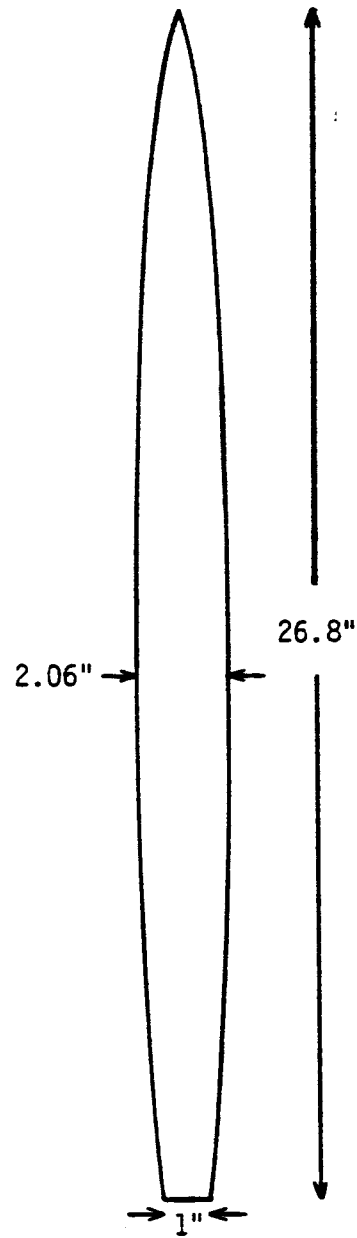
Figure 4.- Force body.
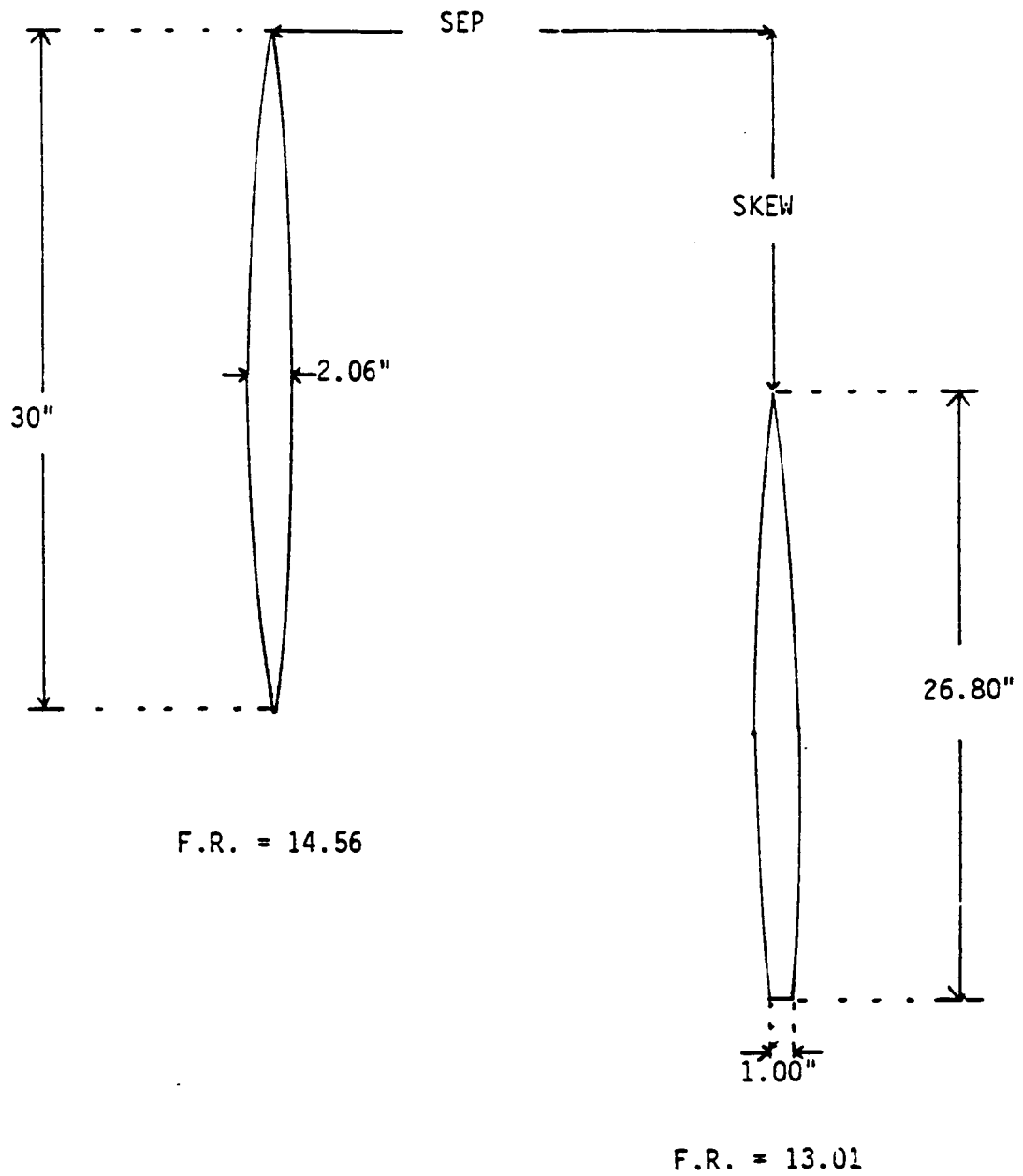
Figure 5.- Body dimensions and position parameters.
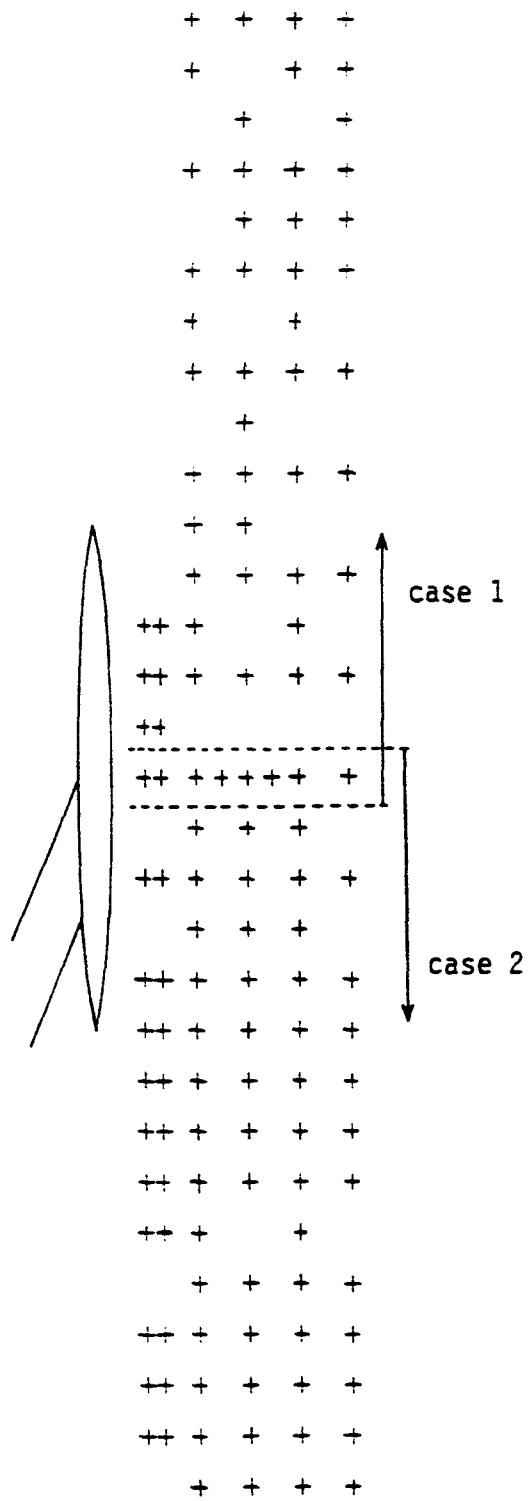
Figure 6.- Test matrix (+ center of force body).

90° line of pressure

0° line of pressure

90°

(1)

(2)
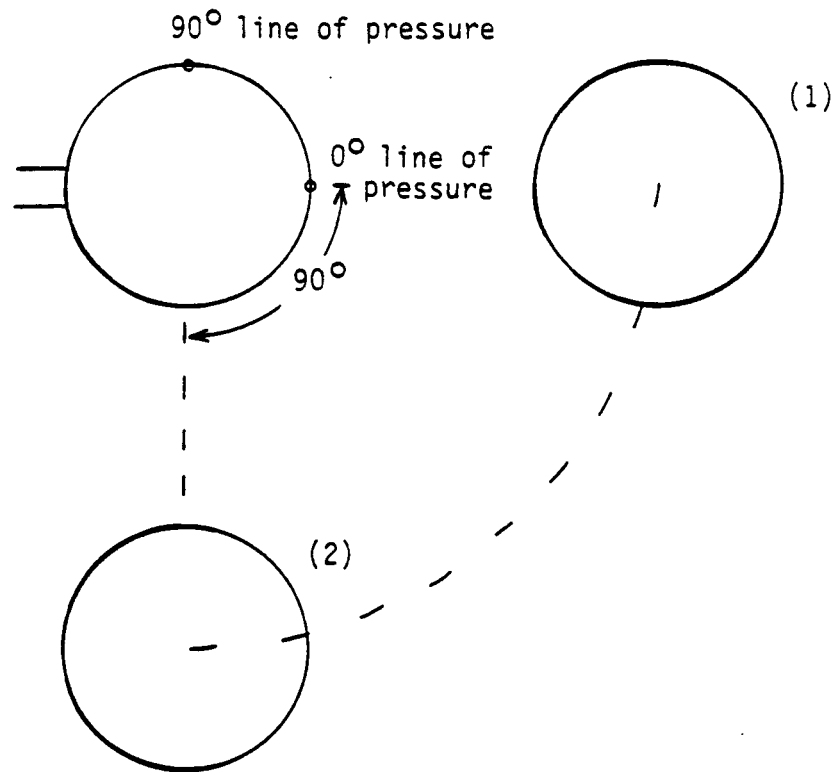
(a) 90° rotation

Figure 7.- Rotation of force body around pressure body.
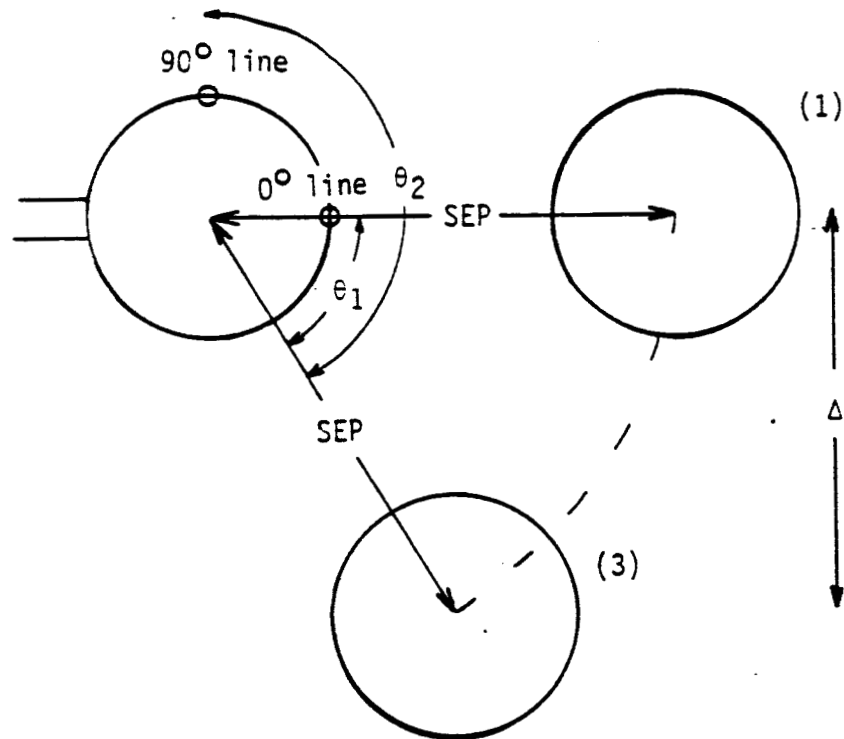
(b) defining parameters

Figure 7.- Concluded.
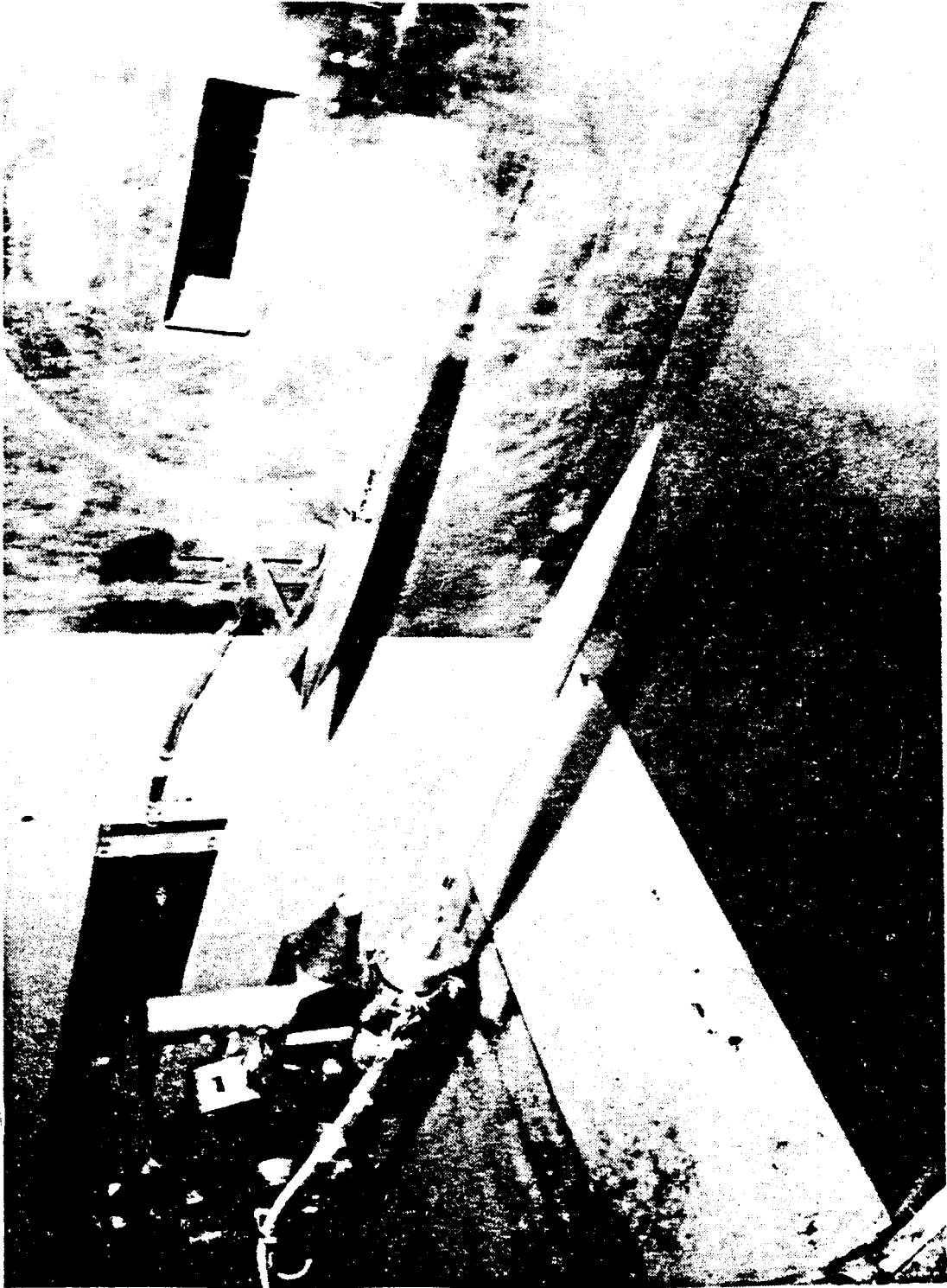
Figure 8.- Photograph of research models and support apparatus in Unitary Plan wind tunnel.
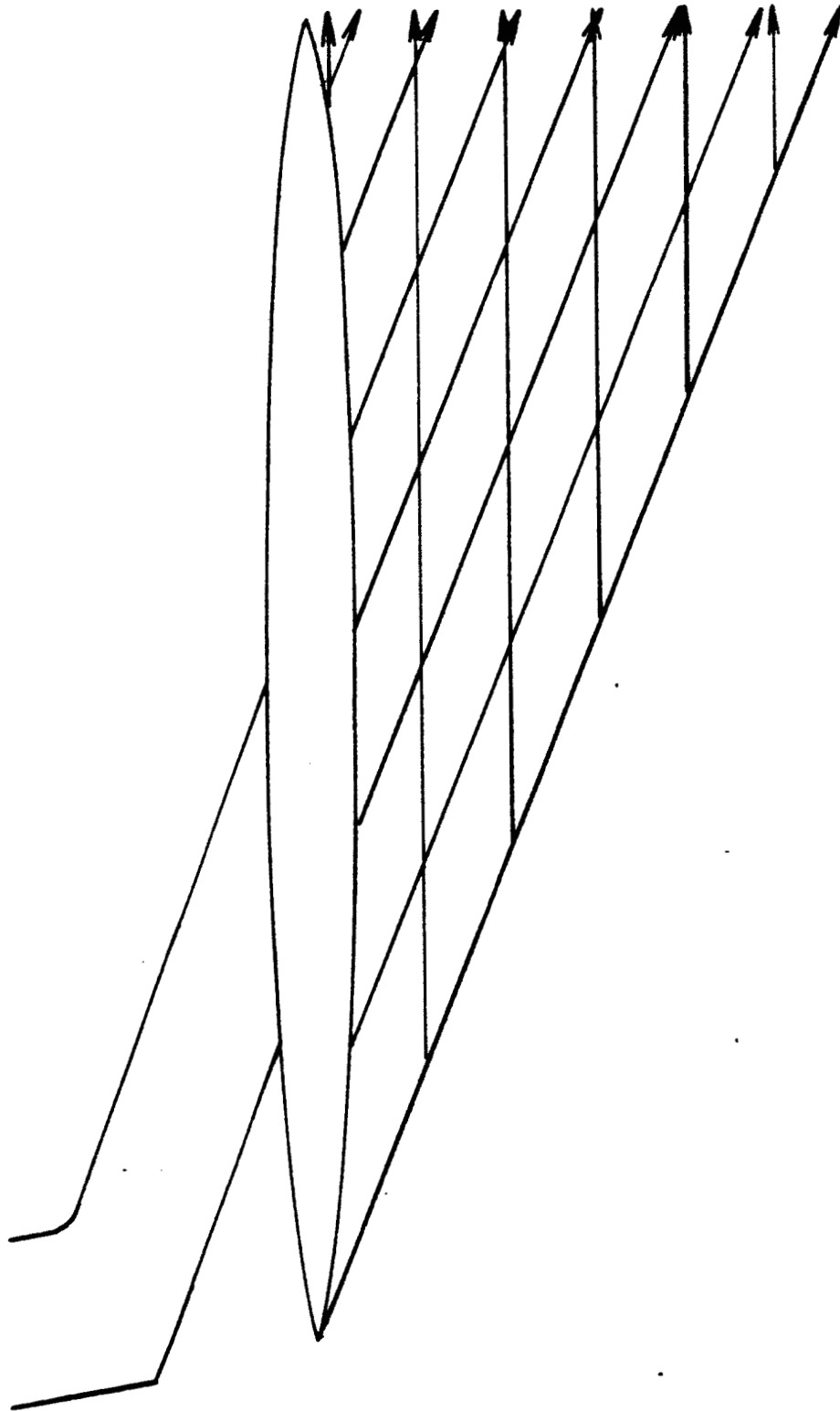
Figure 9.- Area which influences the 30" body.
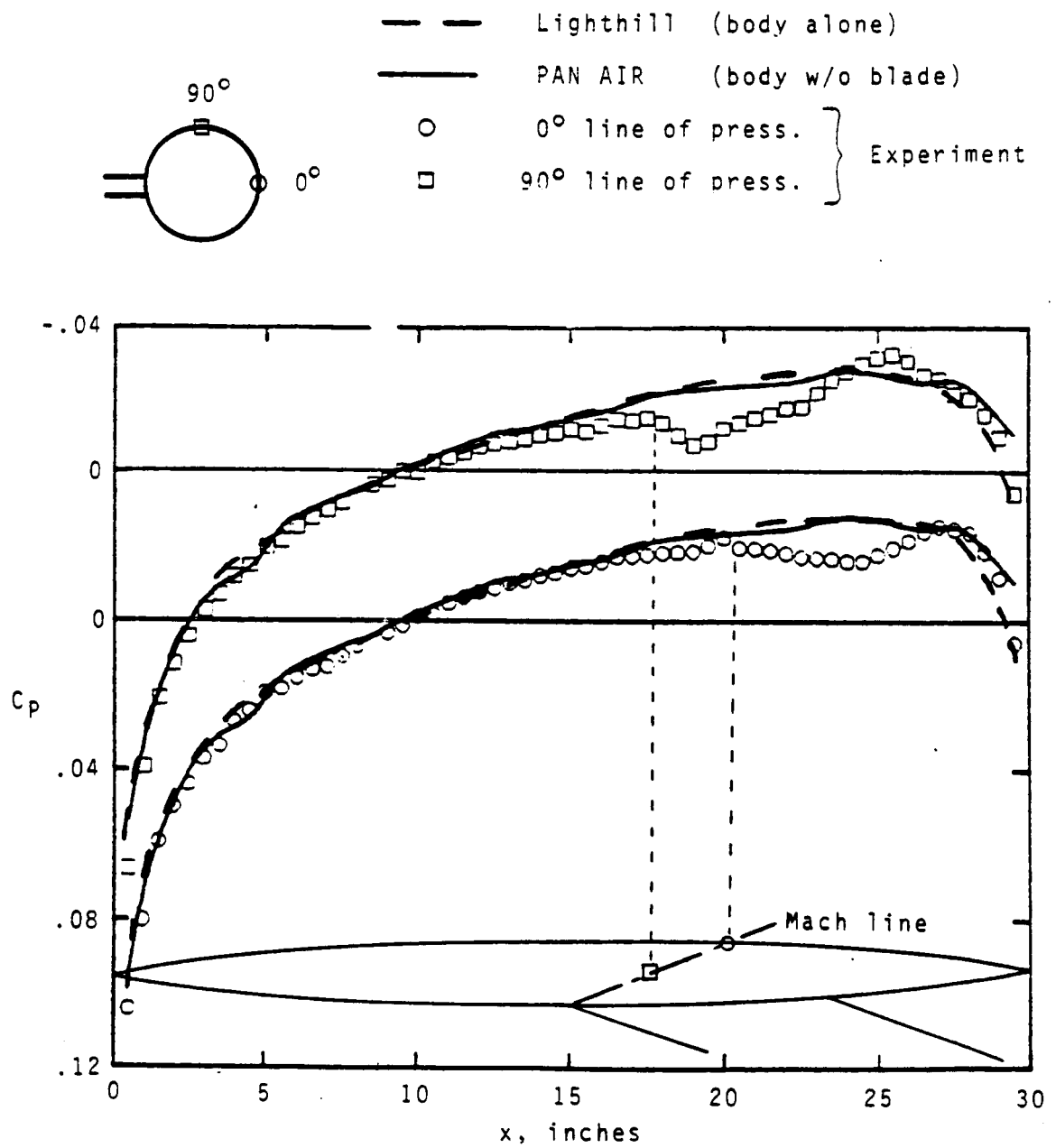
Figure 10.- Pressure distribution of the 30" body alone.
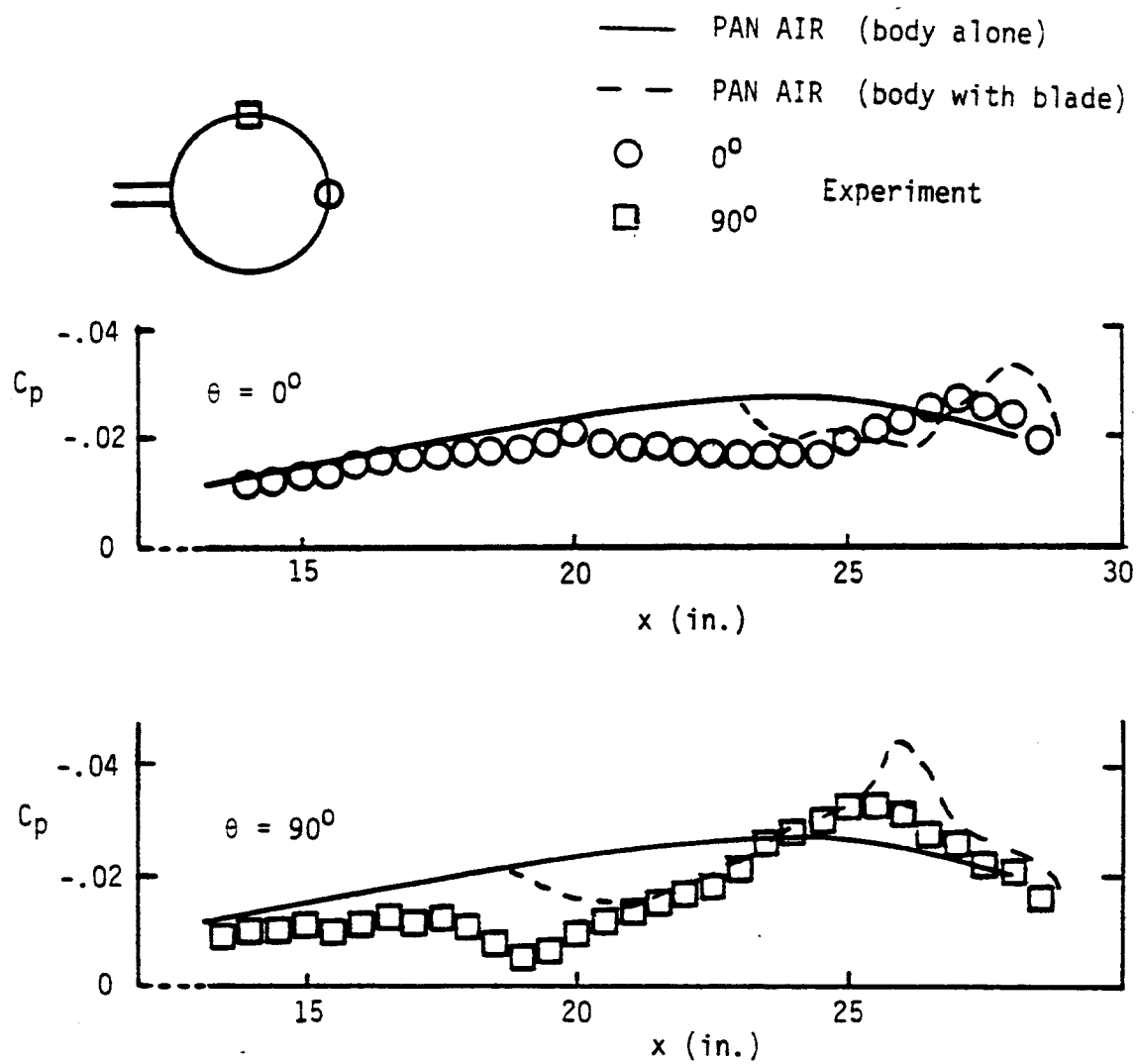
Figure 11.- Experimental and PAN AIR pressure distributions for 30" body with blade located at x = 15".
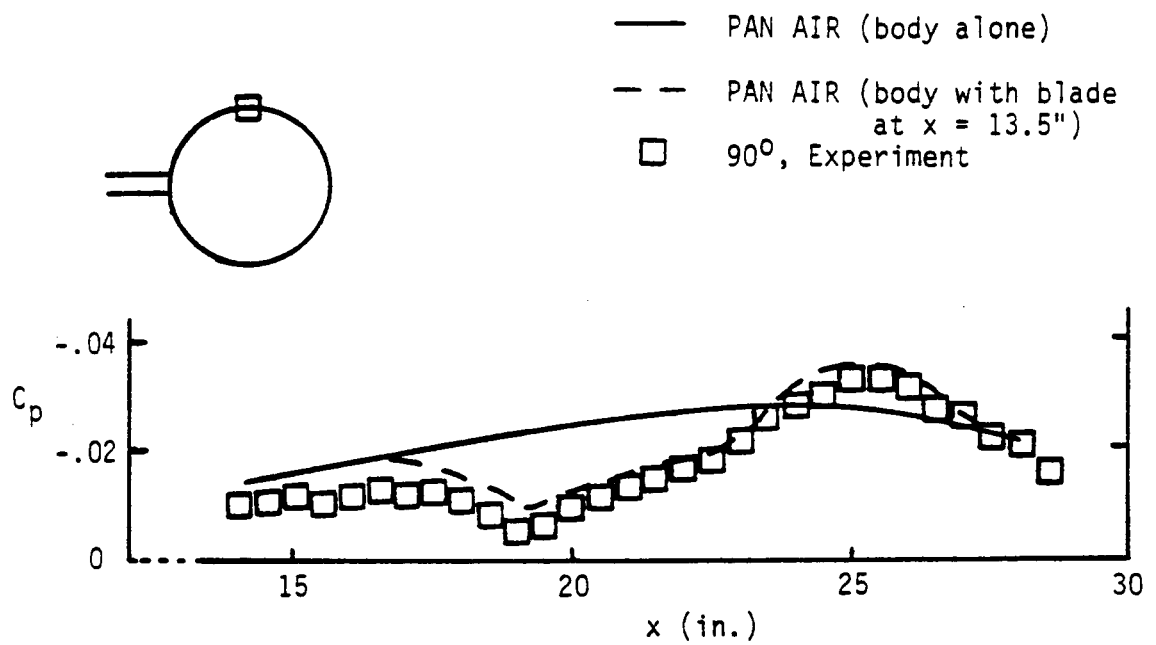
Figure 12.- Experimental and PAN AIR pressure distributions for 30"
body with blade (Experiment: blade at x = 15", PAN AIR:
blade at x = 13.5").
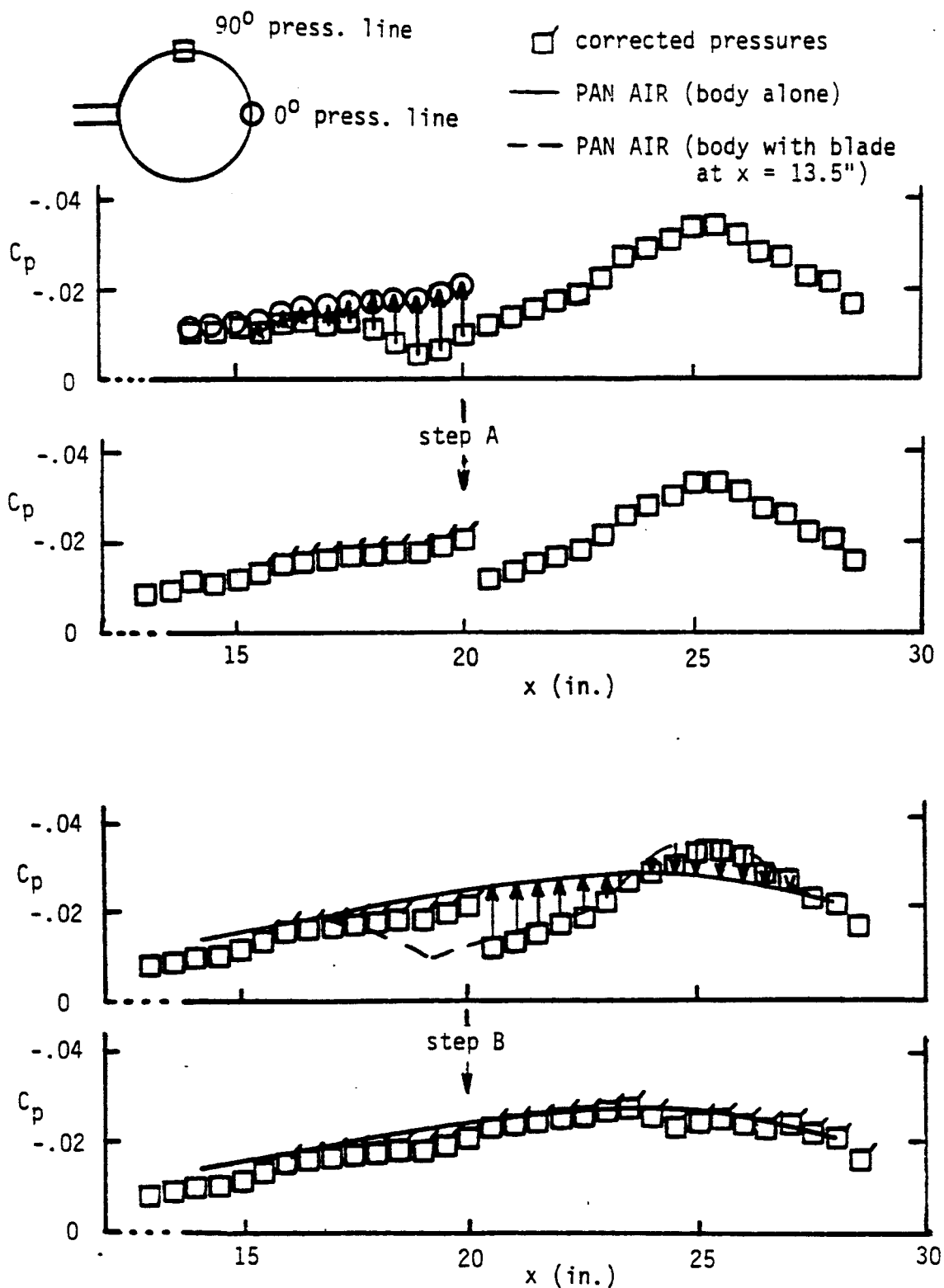
Figure 13.- Procedure for correcting the 90° line of pressure.
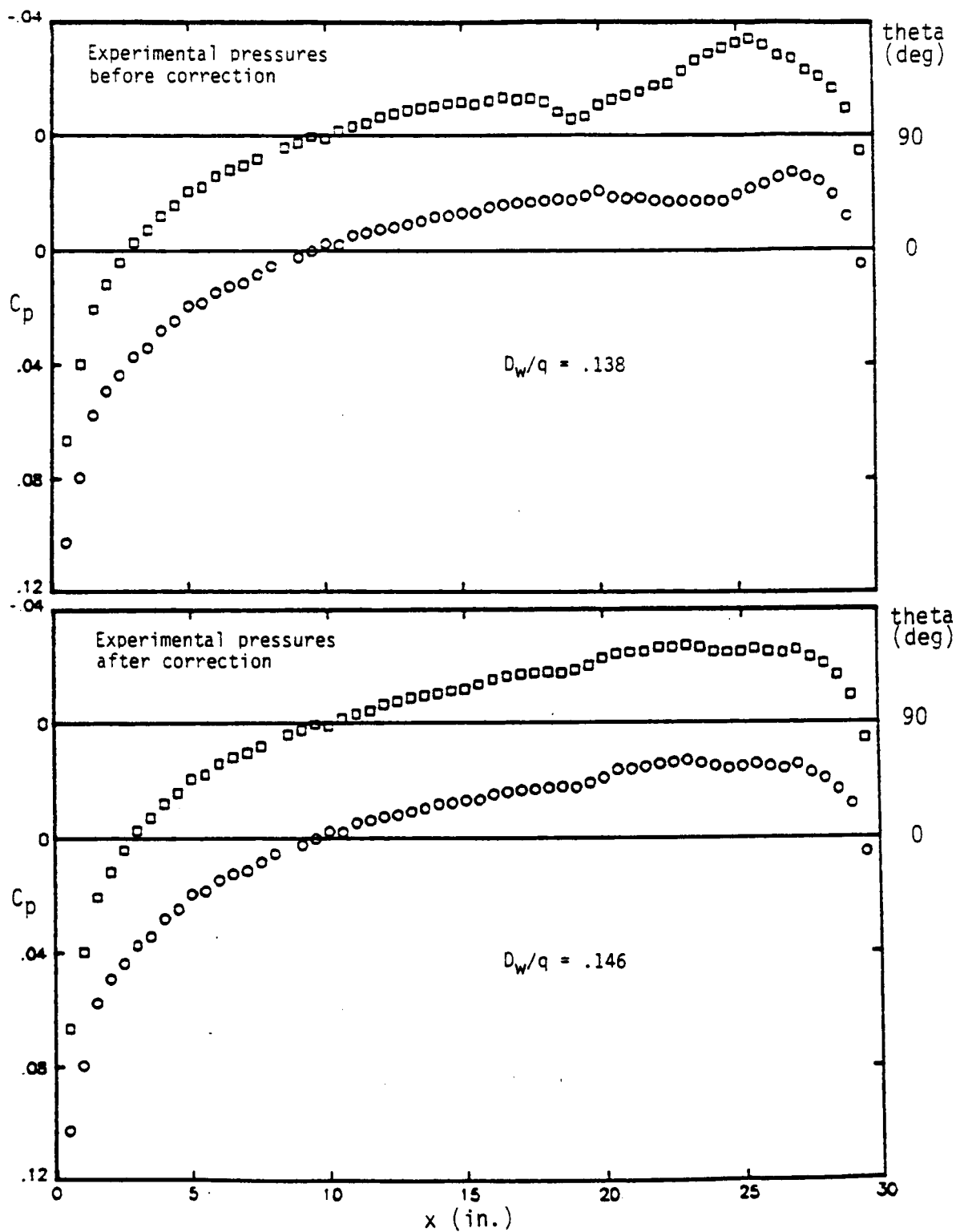
Figure 14.- Experimental pressure distributions of the 30" body
(interference-free) before and after blade correction.
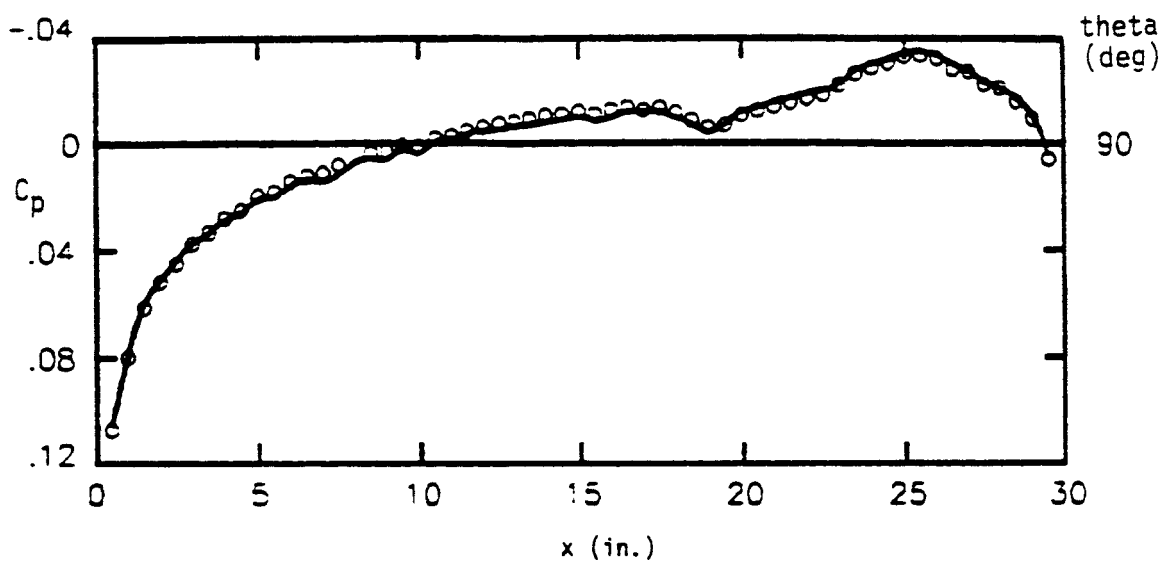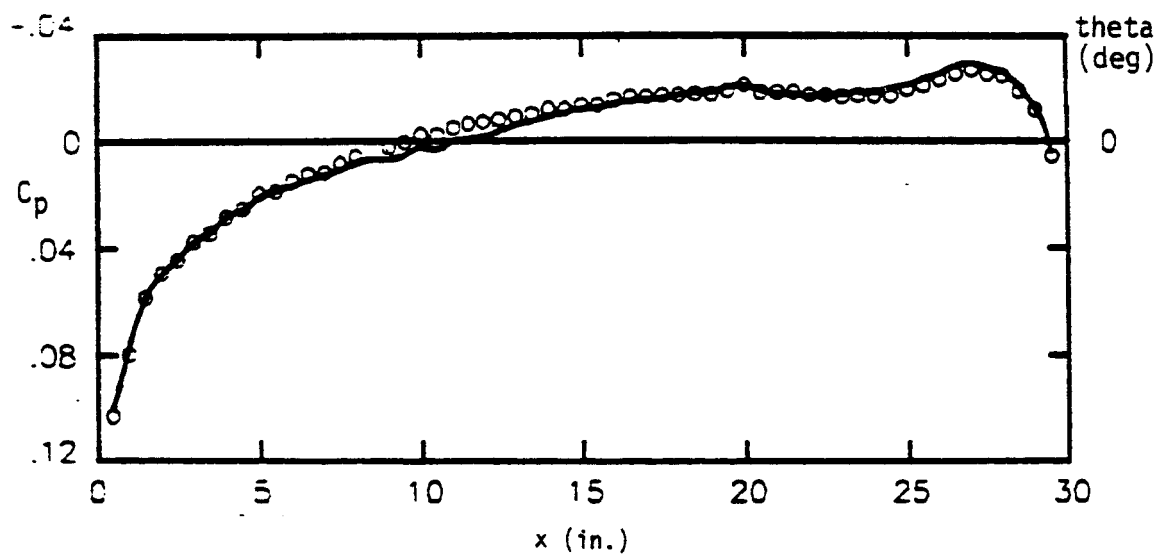
Figure 15.- Pressure distributions of the 30" body (interference-free)
at the two test section locations.
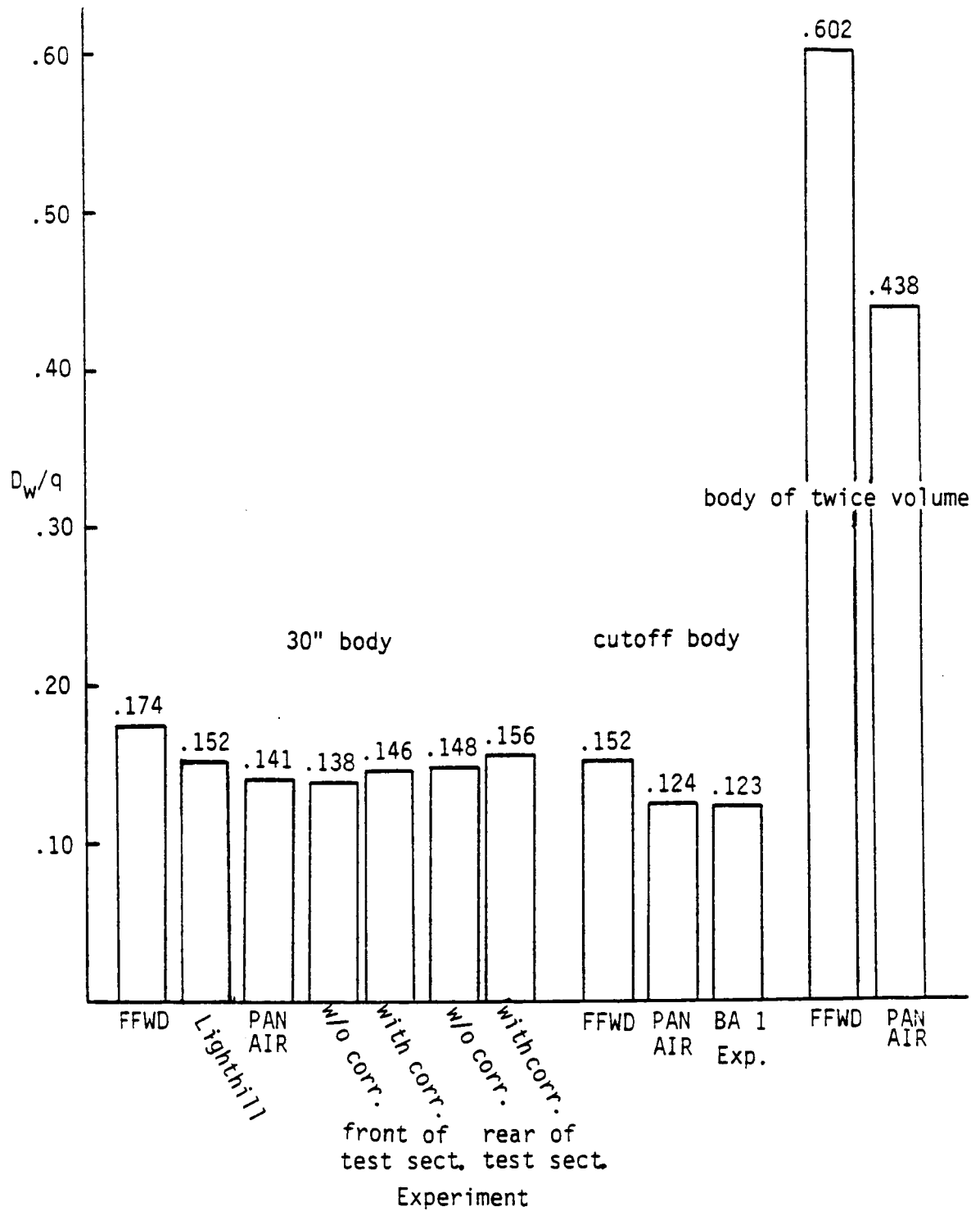
Figure 16.- D_W/q for bodies alone.
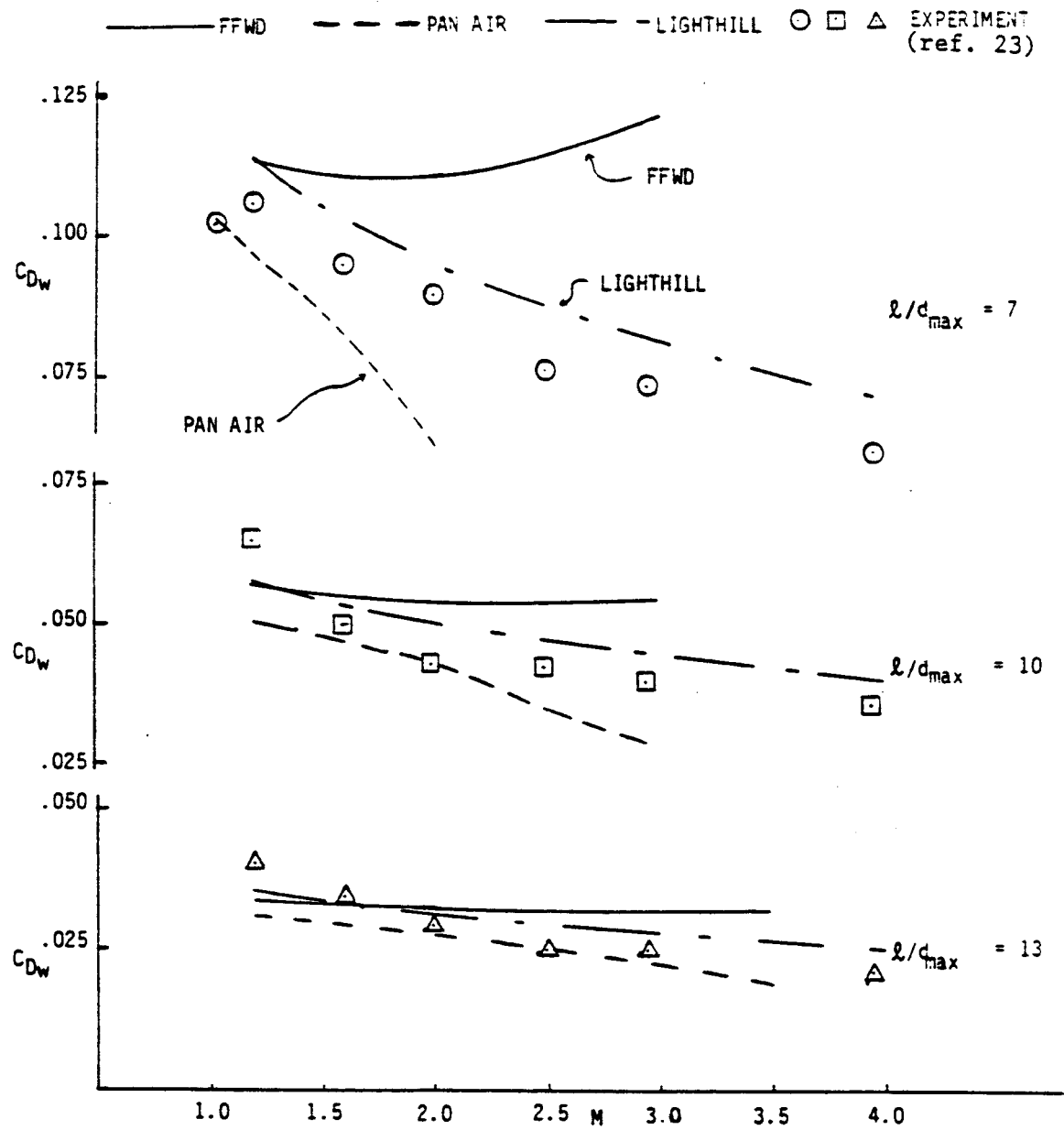
Figure 17.- C_{D_w} versus Mach number for three different bodies of revolution.
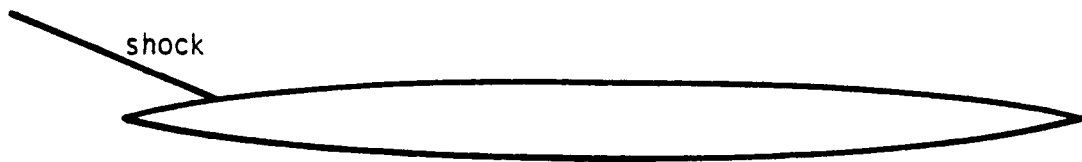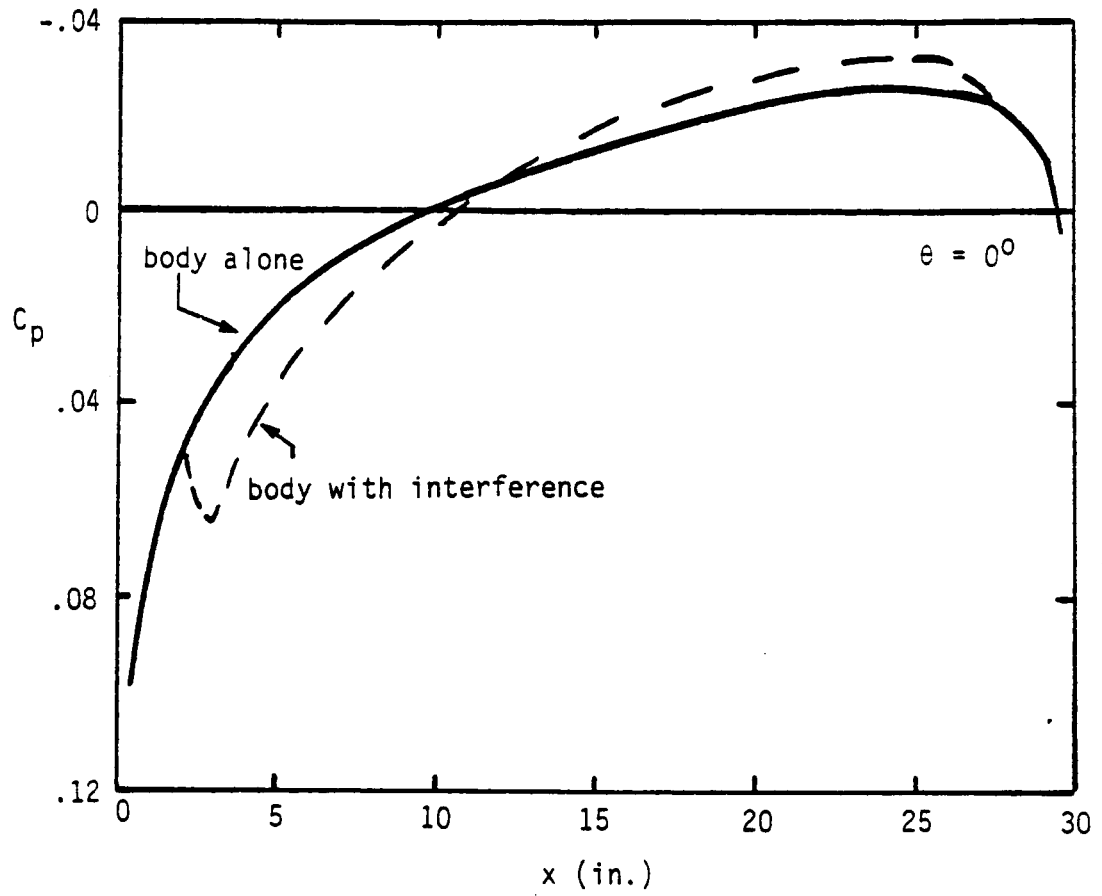
Figure 18.- Change in body pressure distribution due to front end shock impingement.
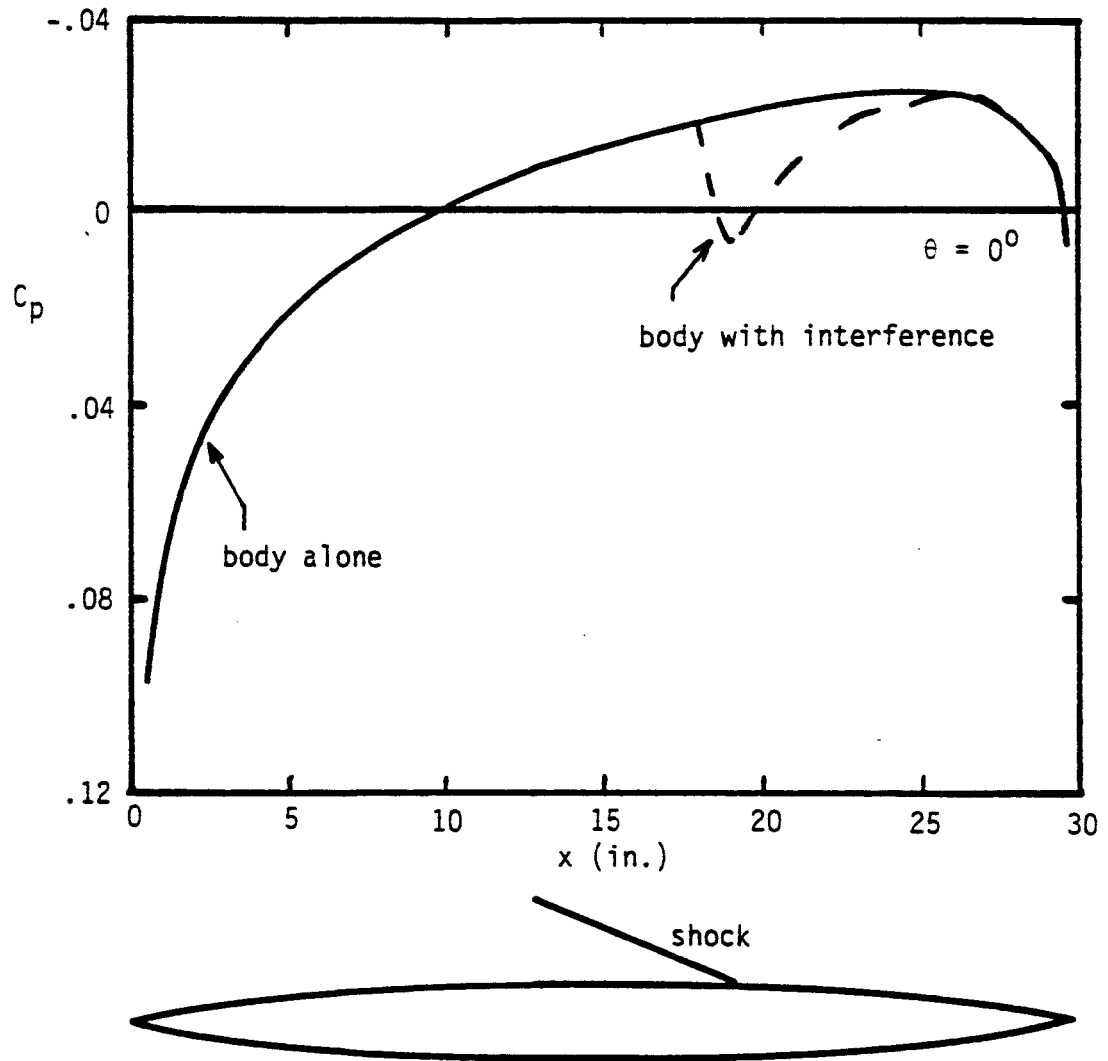
Figure 19.- Change in body pressure distribution due to aft end shock impingement.
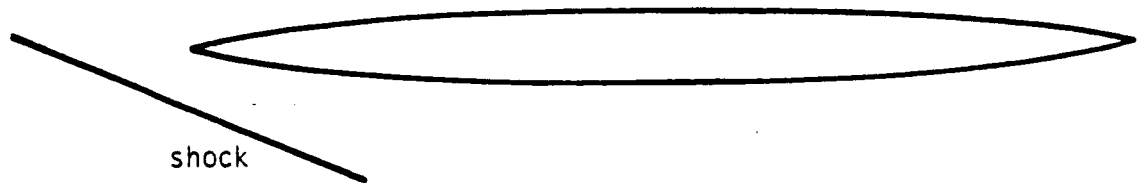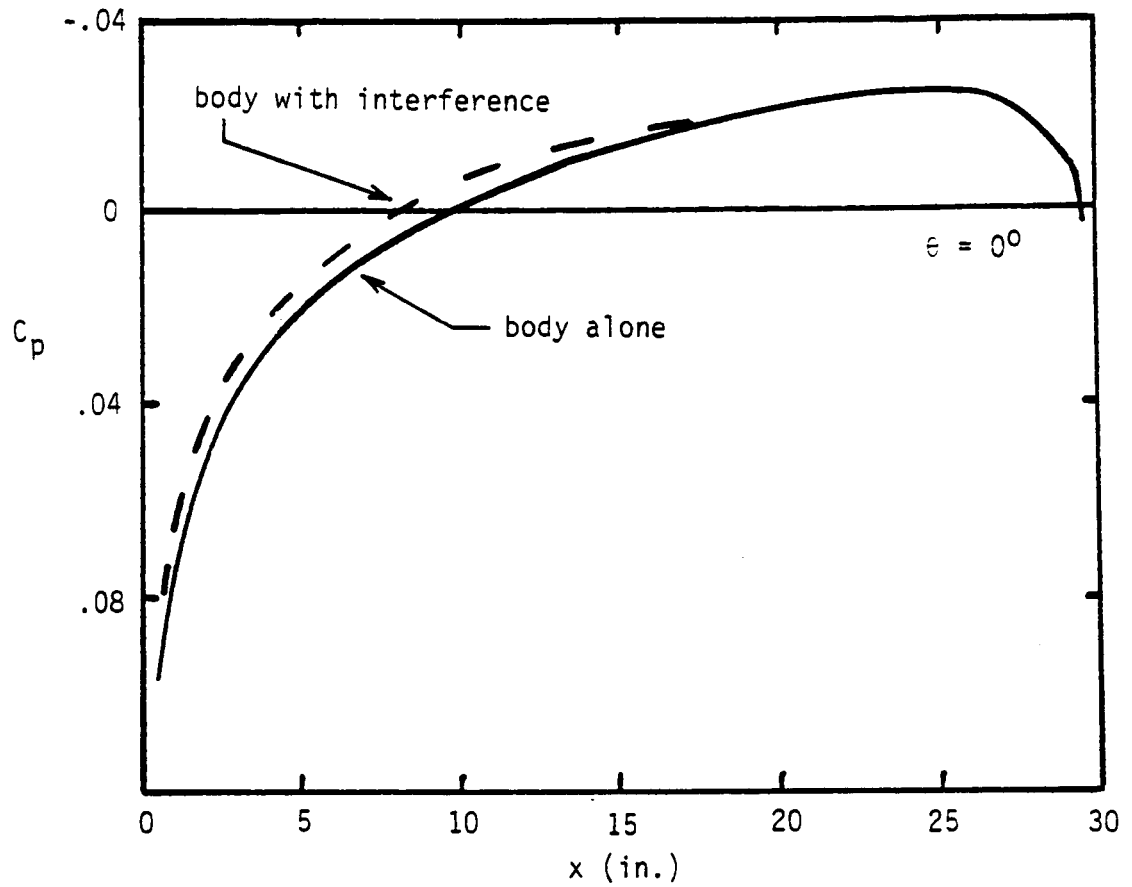
Figure 20.- Change in body pressure distribution due to shock passing a considerable distance (about .2 body lengths) in front of body.
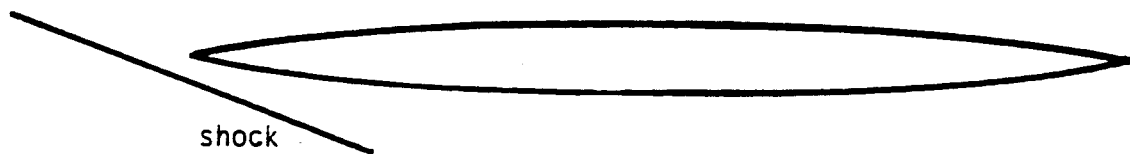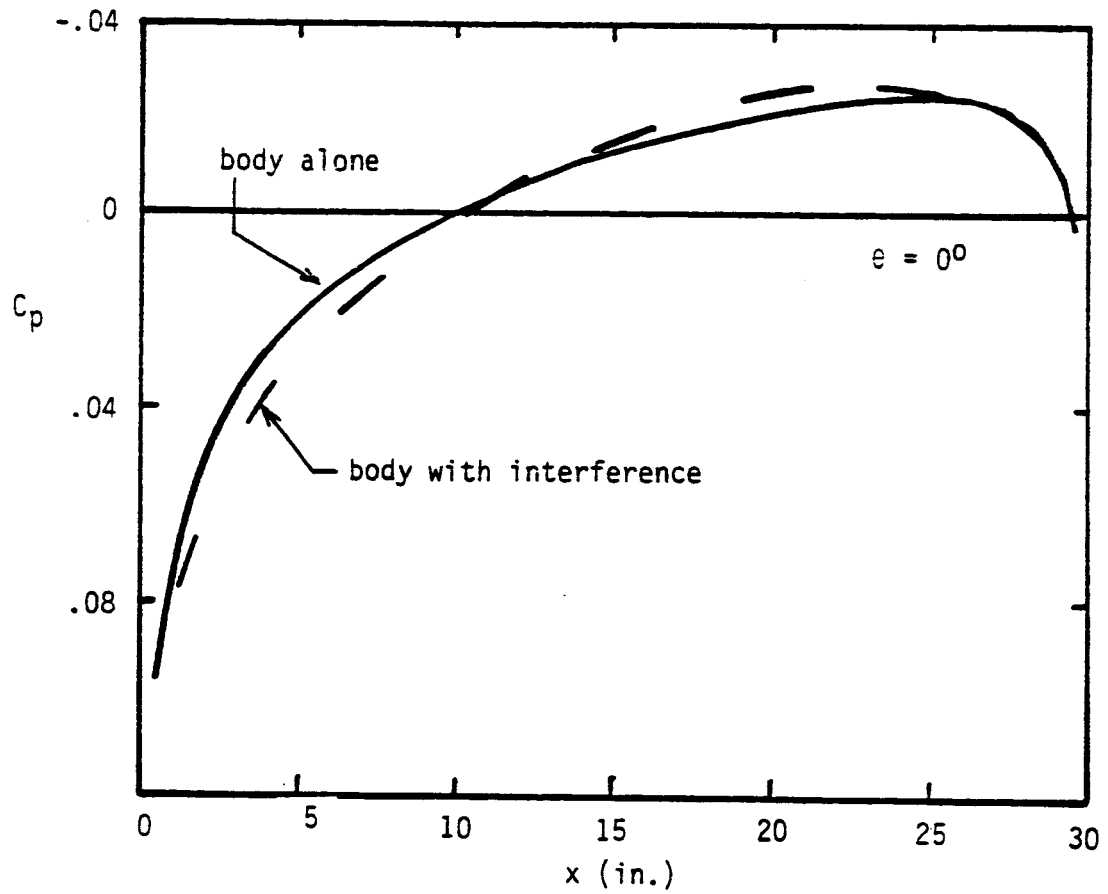
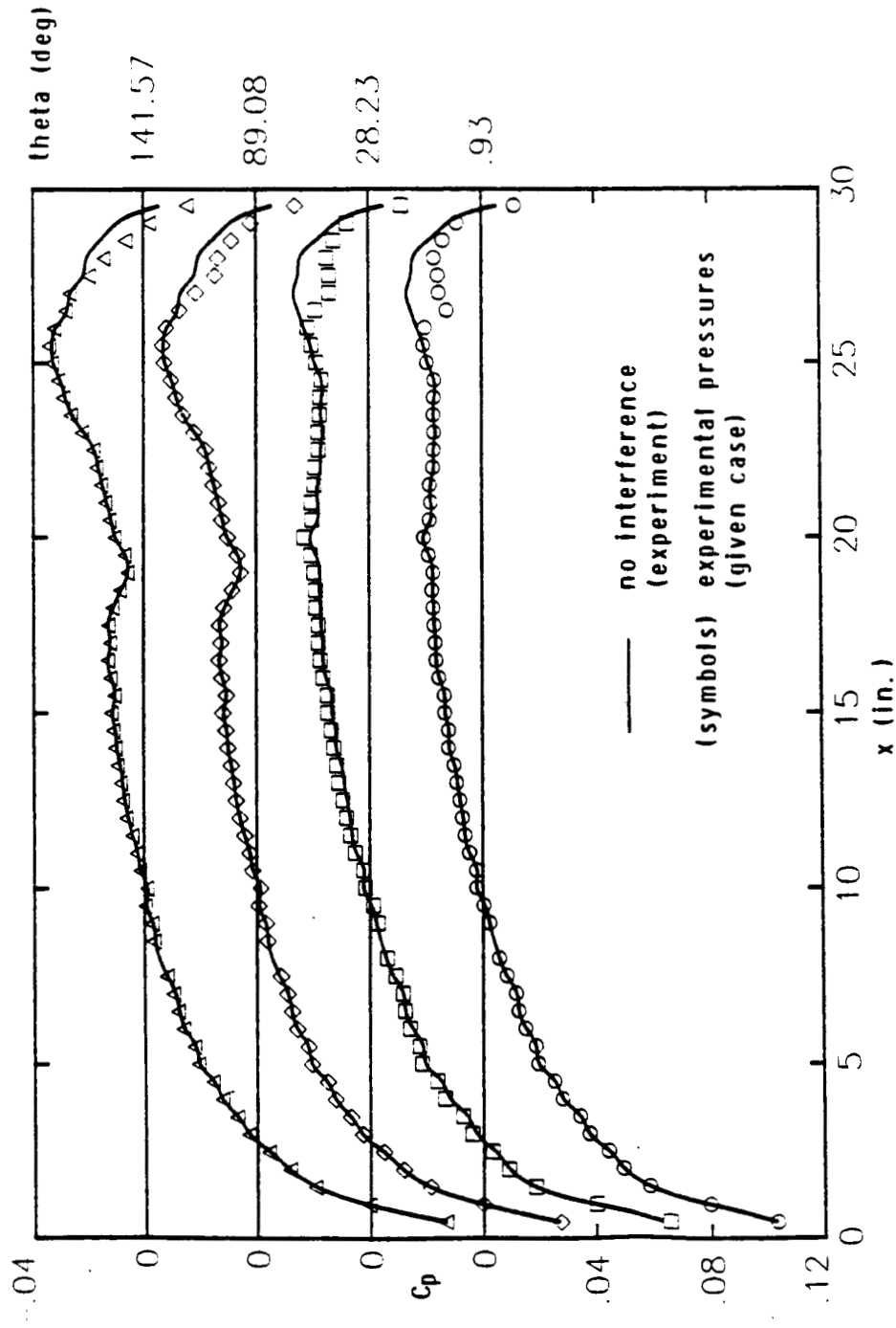Figure 21.- Change in body pressure distribution due to shock passing (less than .1 body lengths) in front of body.

SEP/ℓ = .13   .20   .30   .40   .50

Mach
lines

blade
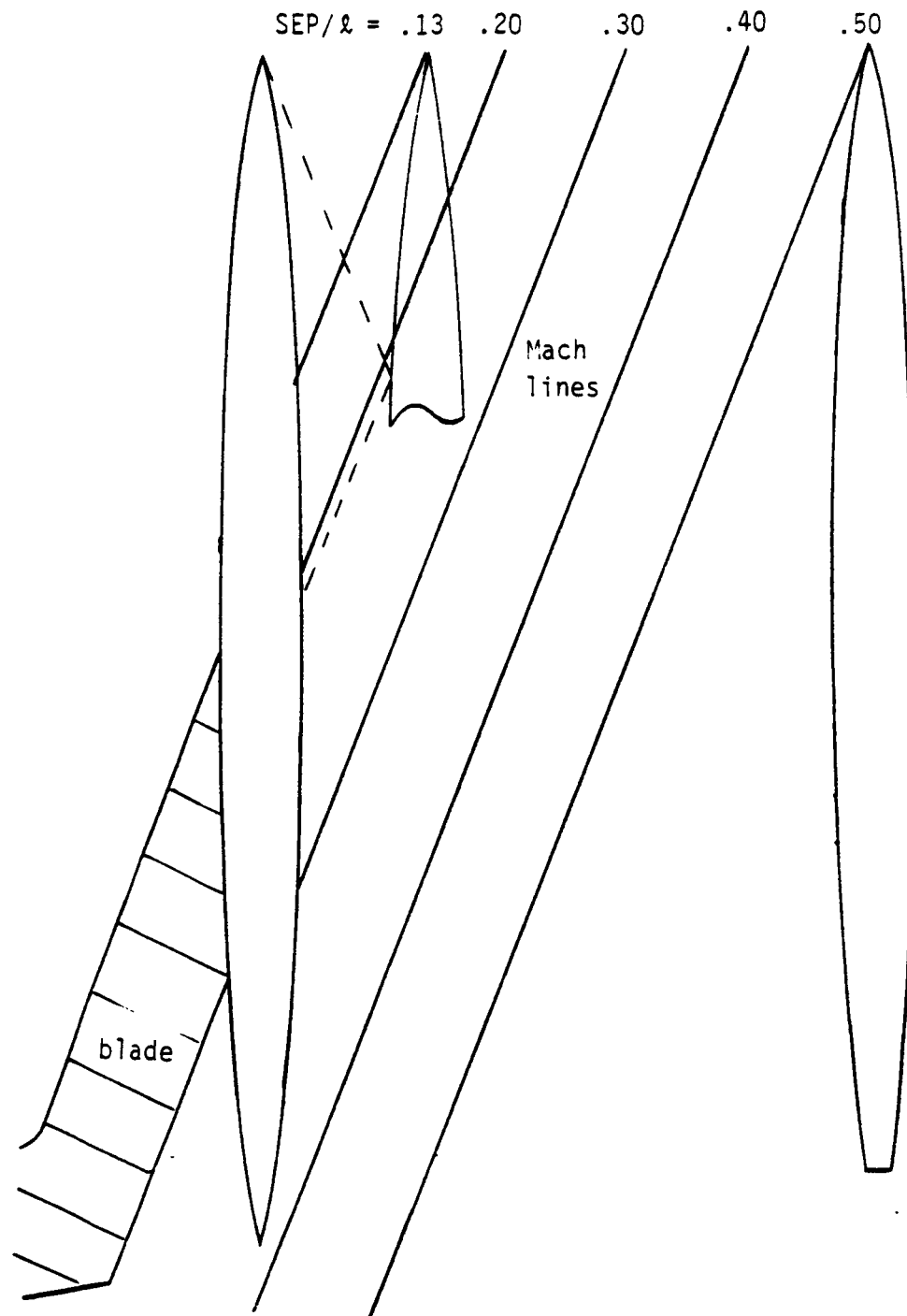
Figure 22.- Illustration of different separations of the bodies.
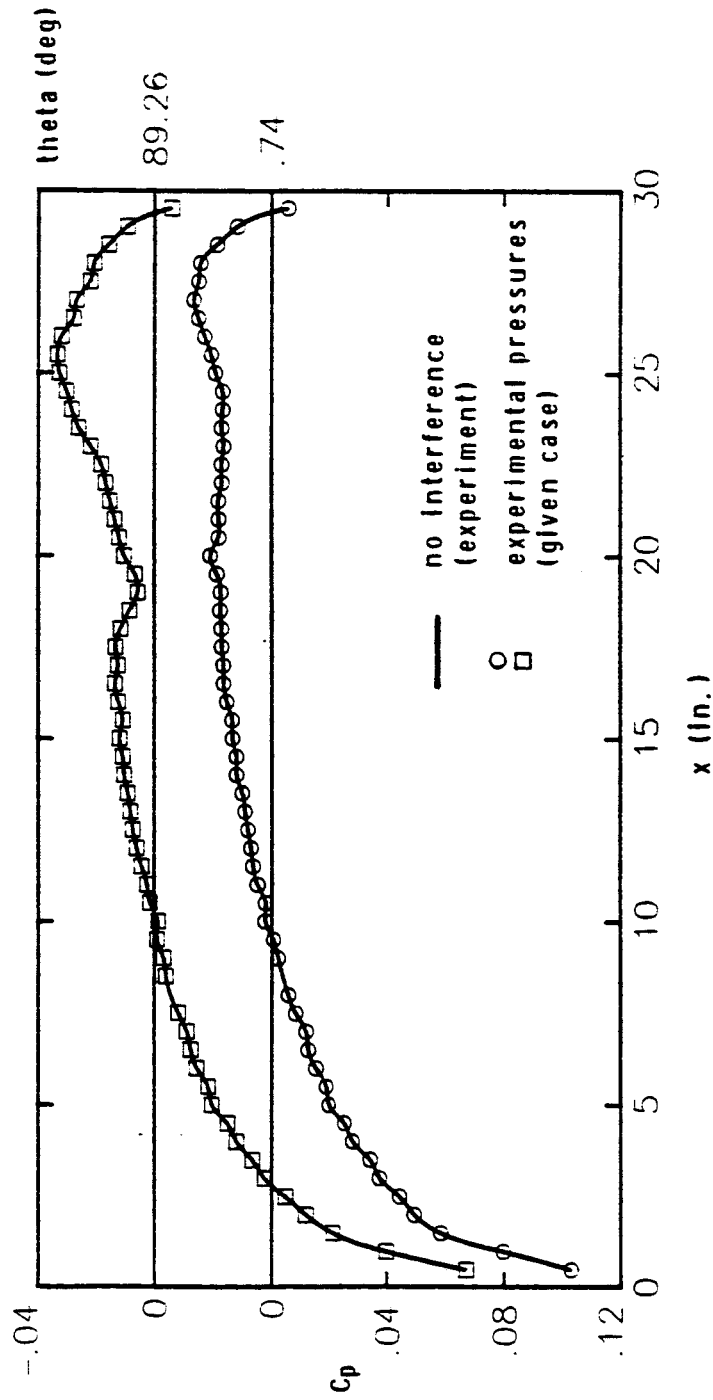
(a) SEP/ℓ = .50

Figure 23. - Experimental pressure distributions at different values of SEP/ℓ.
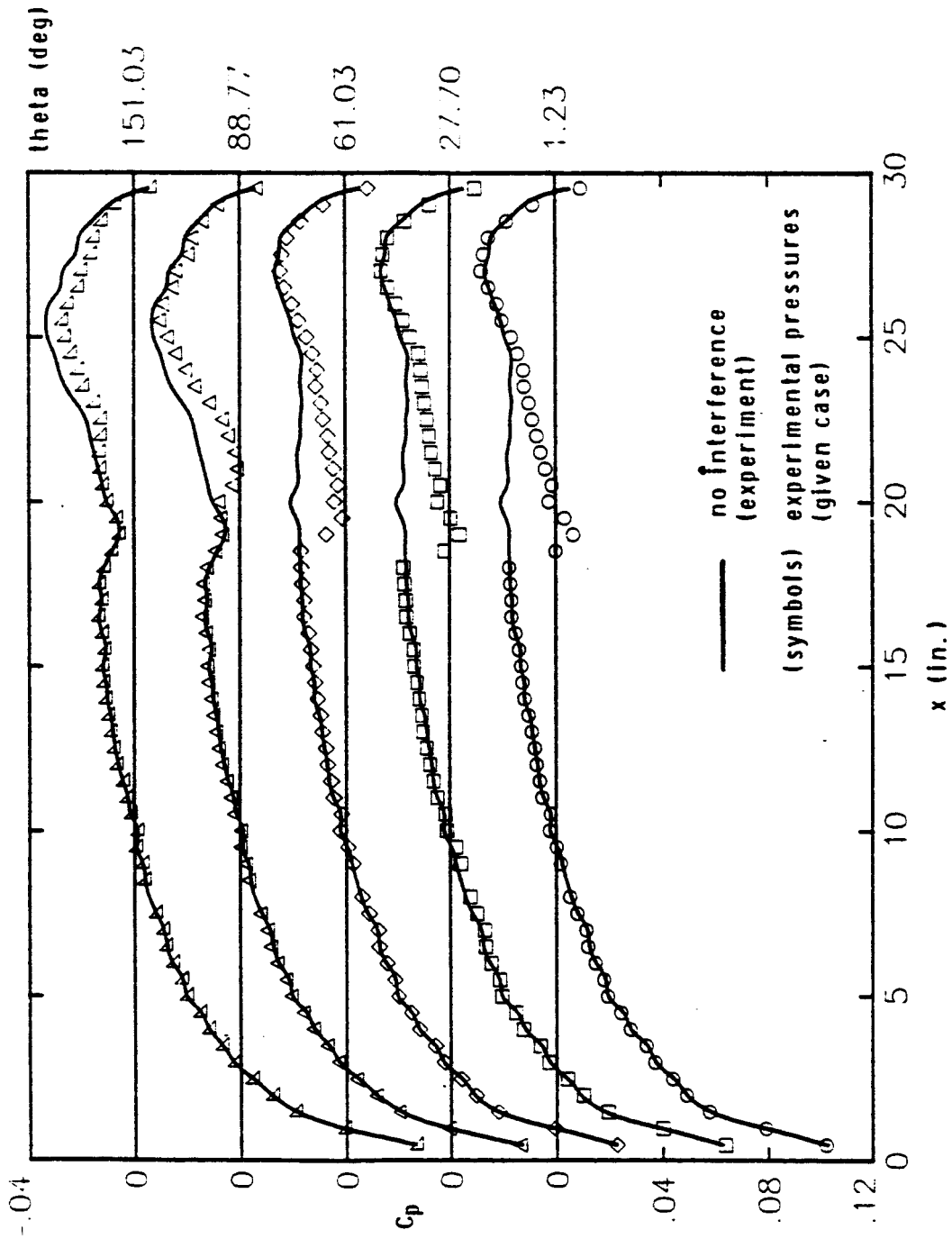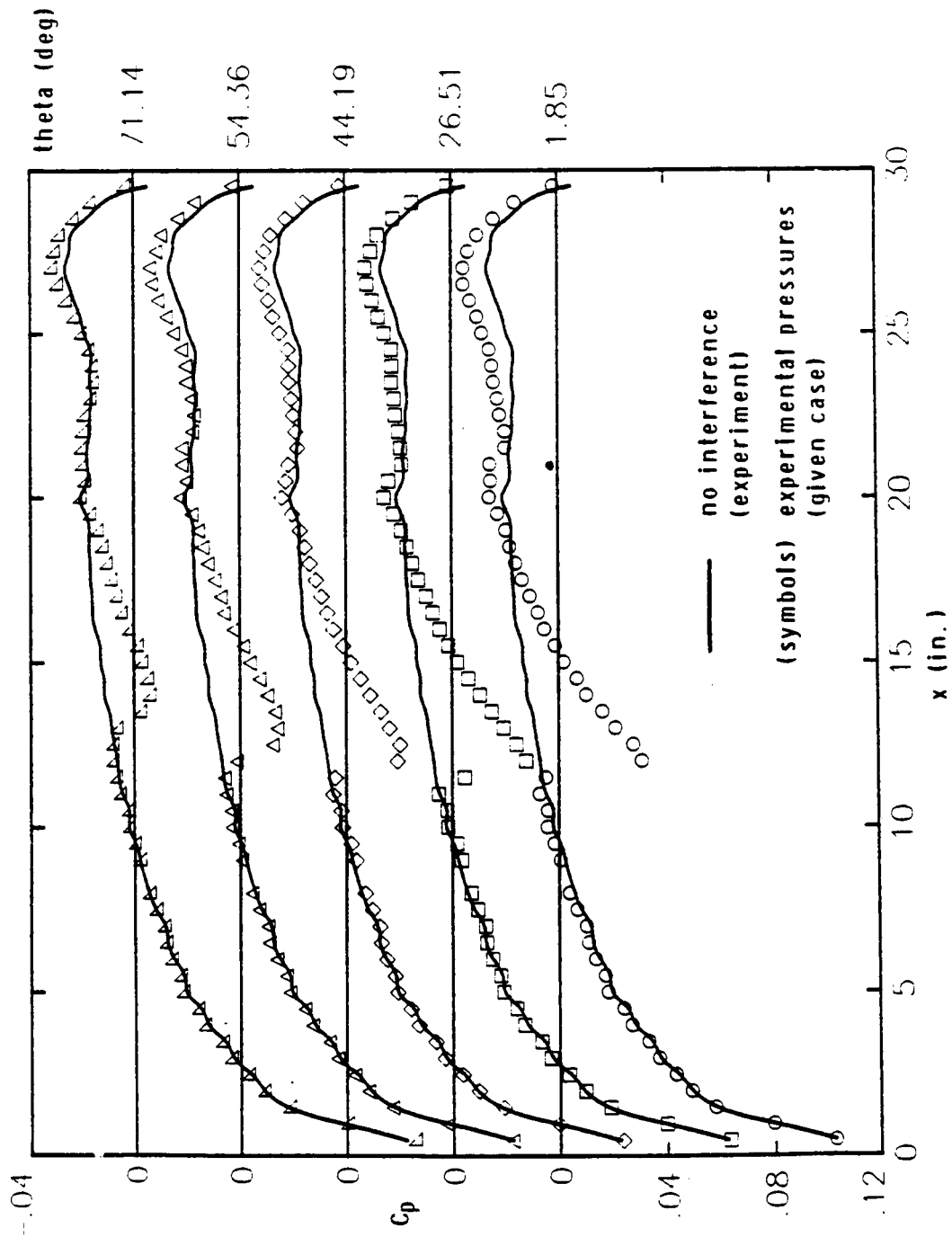
(b) SEP/ℓ = .40

Figure 23. - Continued.

theta (deg)

151.03

88.77

61.03

27.70

1.23

—————— no interference
(experiment)

(symbols) experimental pressures
(given case)

(c) SEP/ℓ = .30

Figure 23. - Continued.

(d) SEP/ℓ = .20

Figure 23. - Continued.

theta (deg)

161.14

144.36

134.19

116.51

88.15

no interference
(experiment)

(symbols) experimental pressures
(given case)
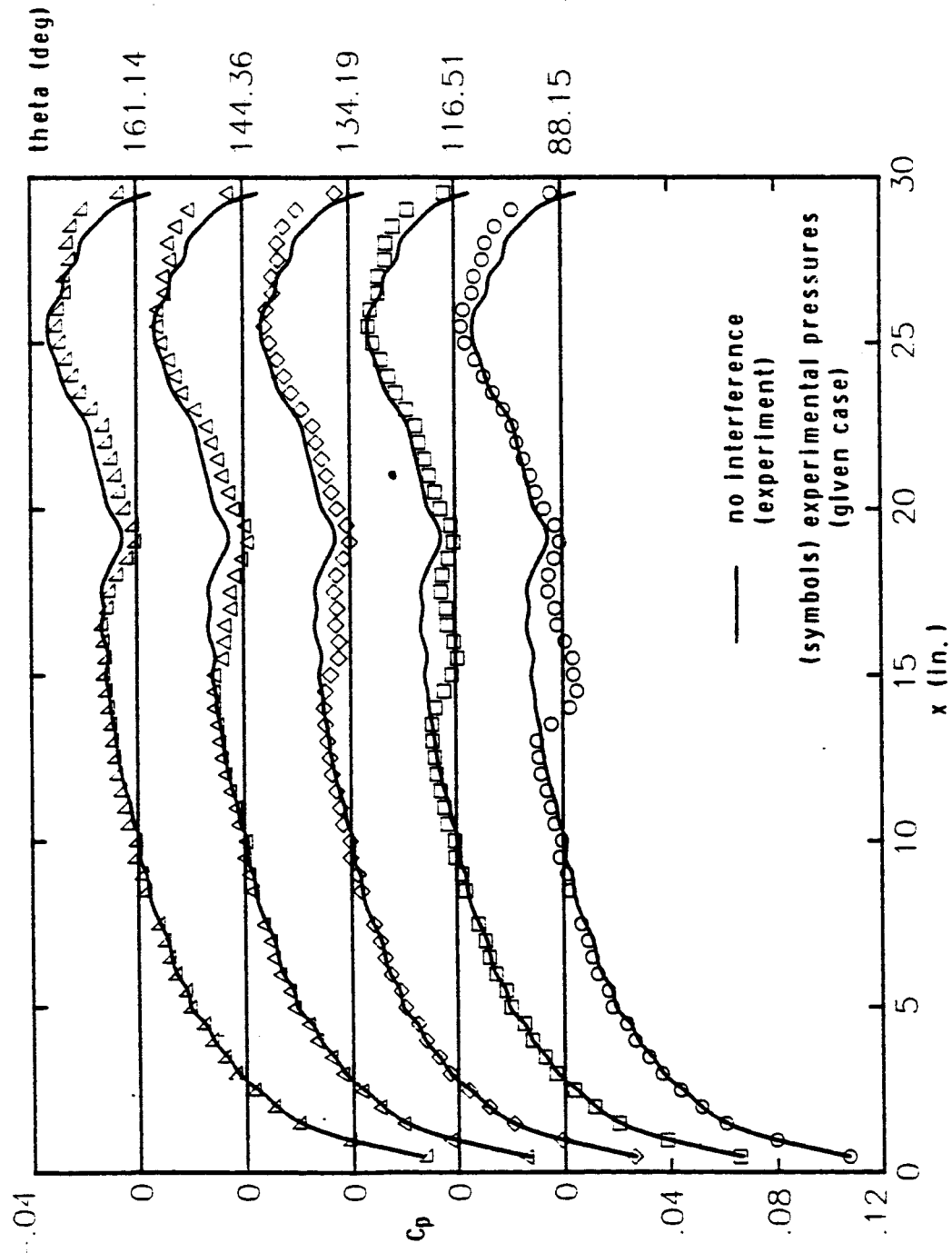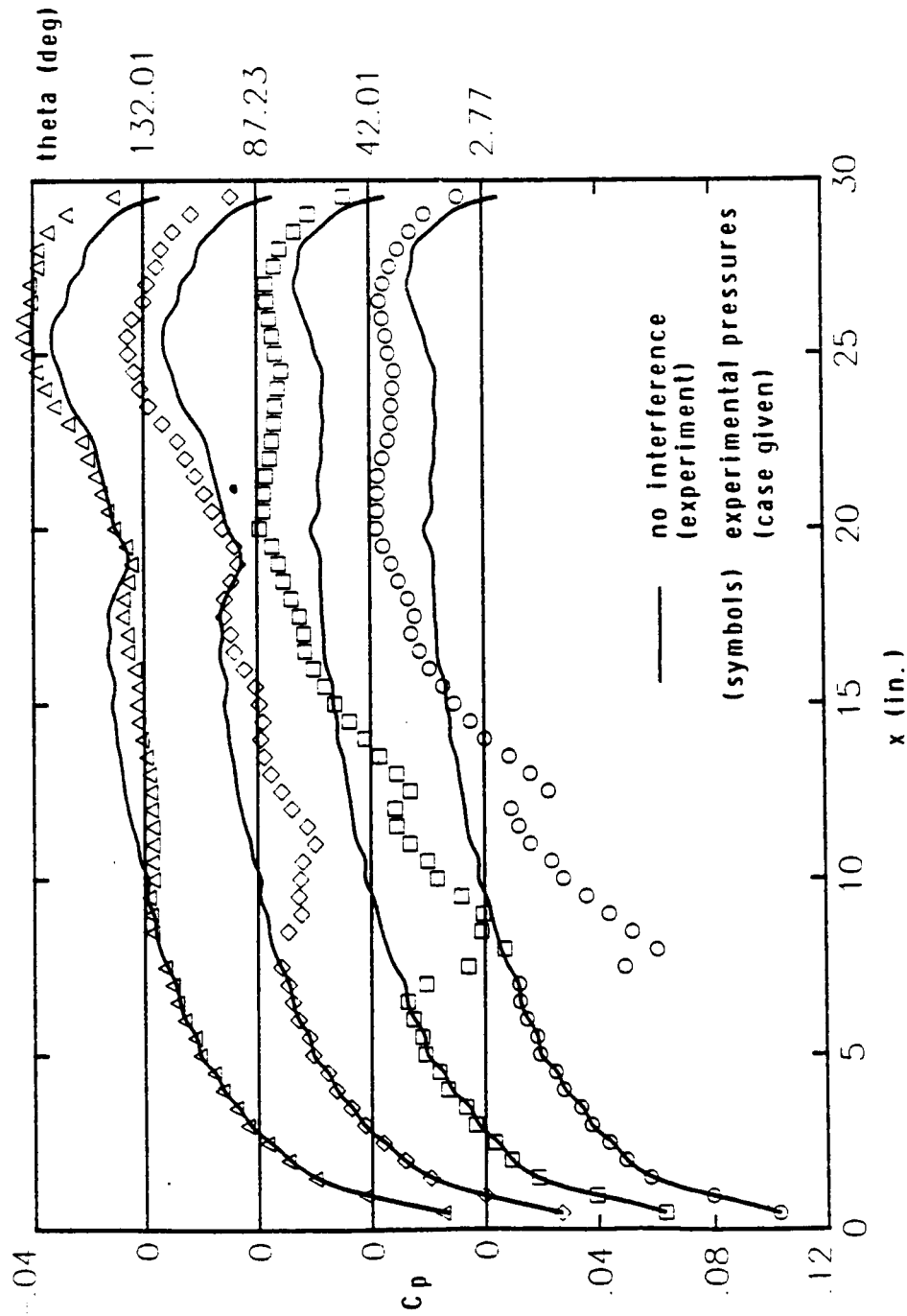
(d) Concluded (SEP/ℓ = .20)

Figure 23. - Continued.
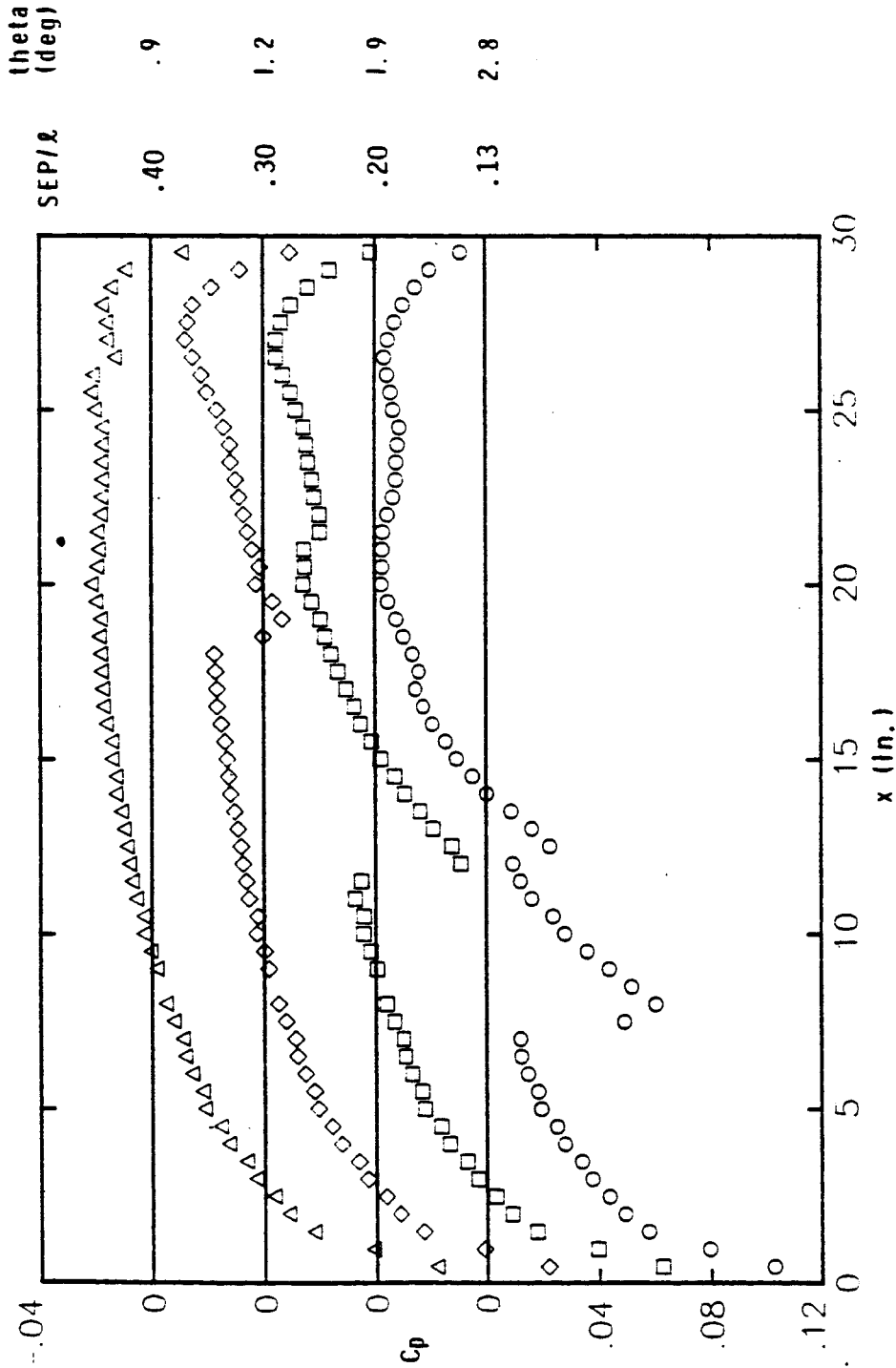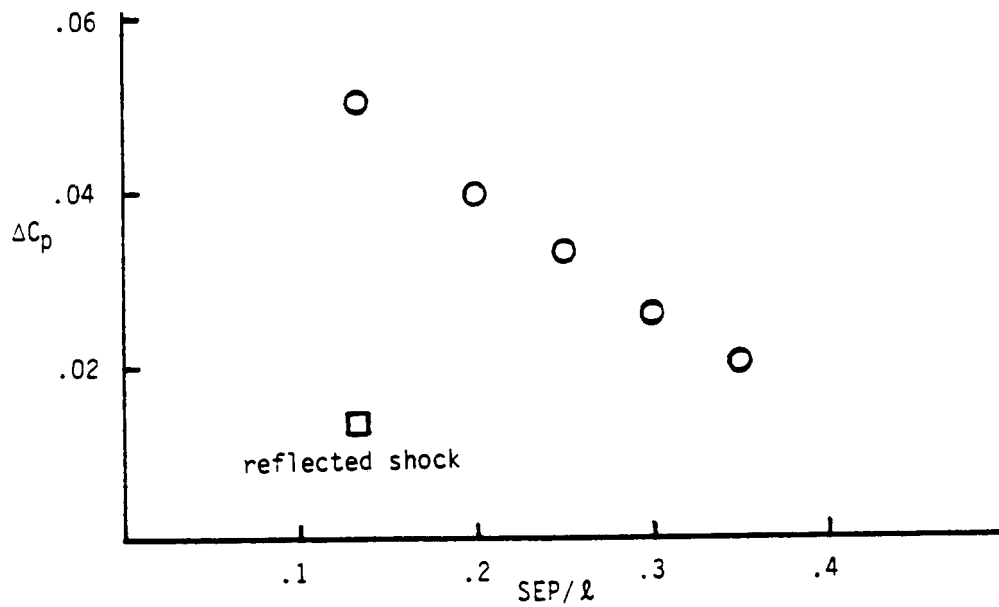
(e) SEP/ℓ = .13
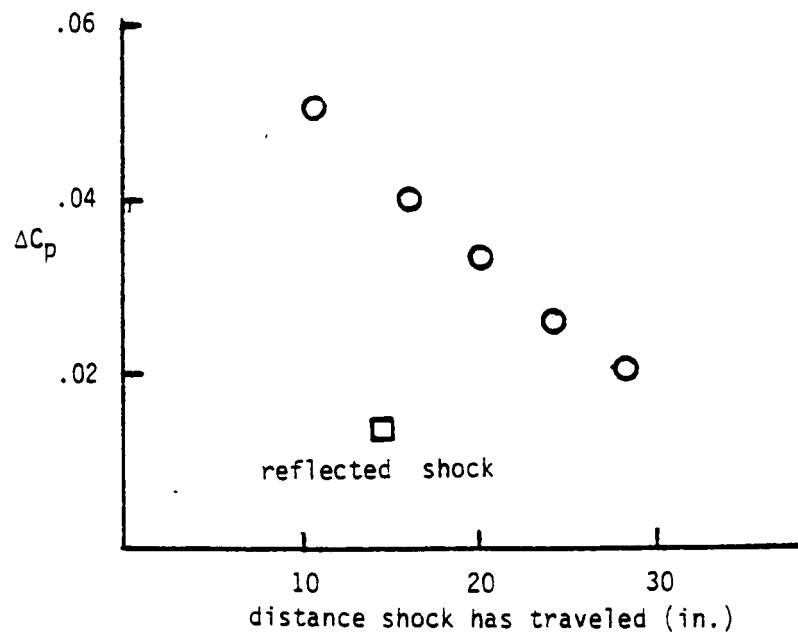
Figure 23. - Concluded.

Figure 24.- Experimental pressure distributions for four different separations.

(a) peak change in C_p vs. SEP/ℓ

(b) peak change in C_p vs. distance shock has traveled

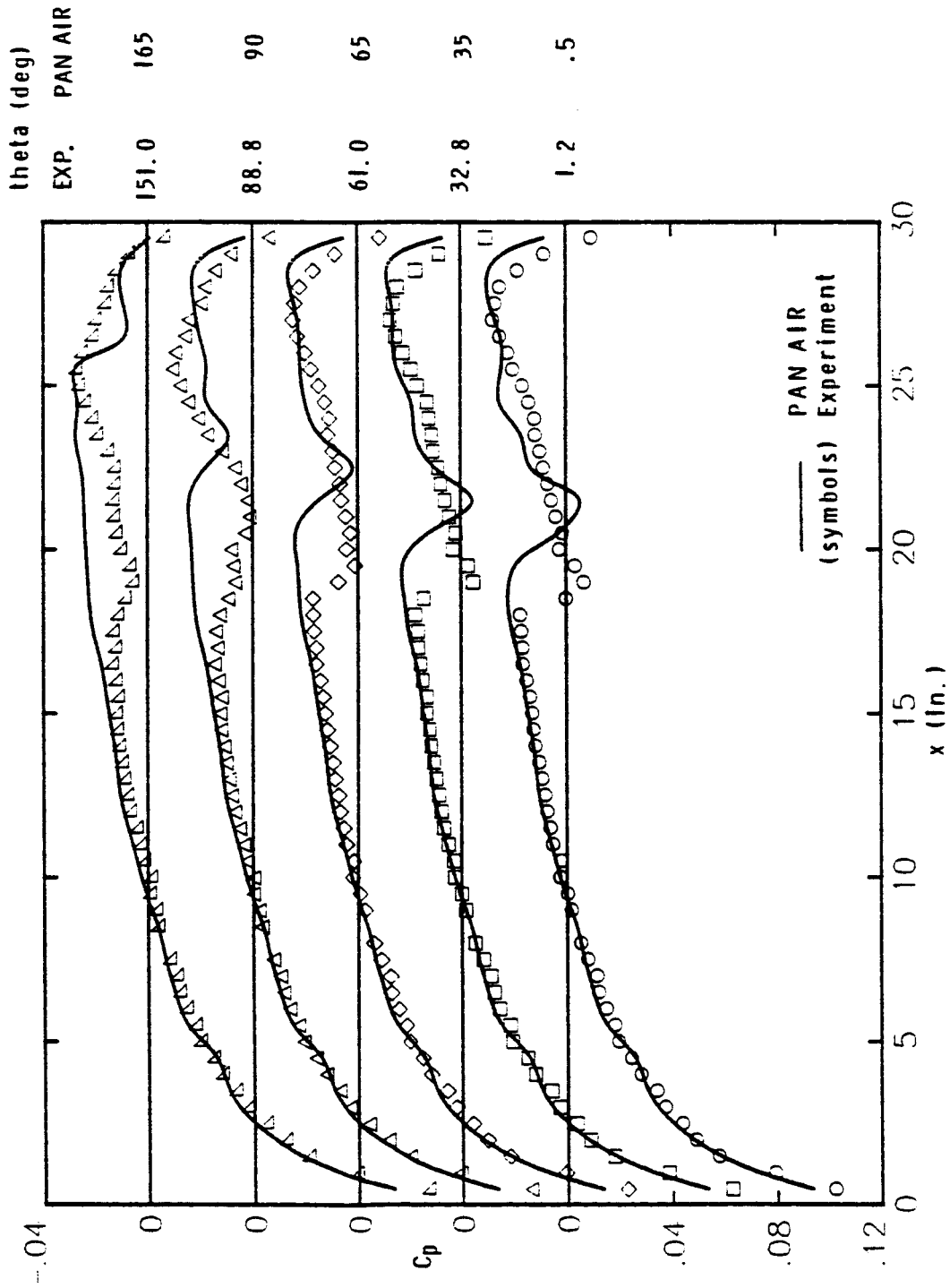Figure 25.- Comparison of ΔC_p for the pressure peaks at four different separations.

(a) SEP/ℓ = .30

Figure 26. - Pressure distribution comparisons between experiment and PAN AIR.
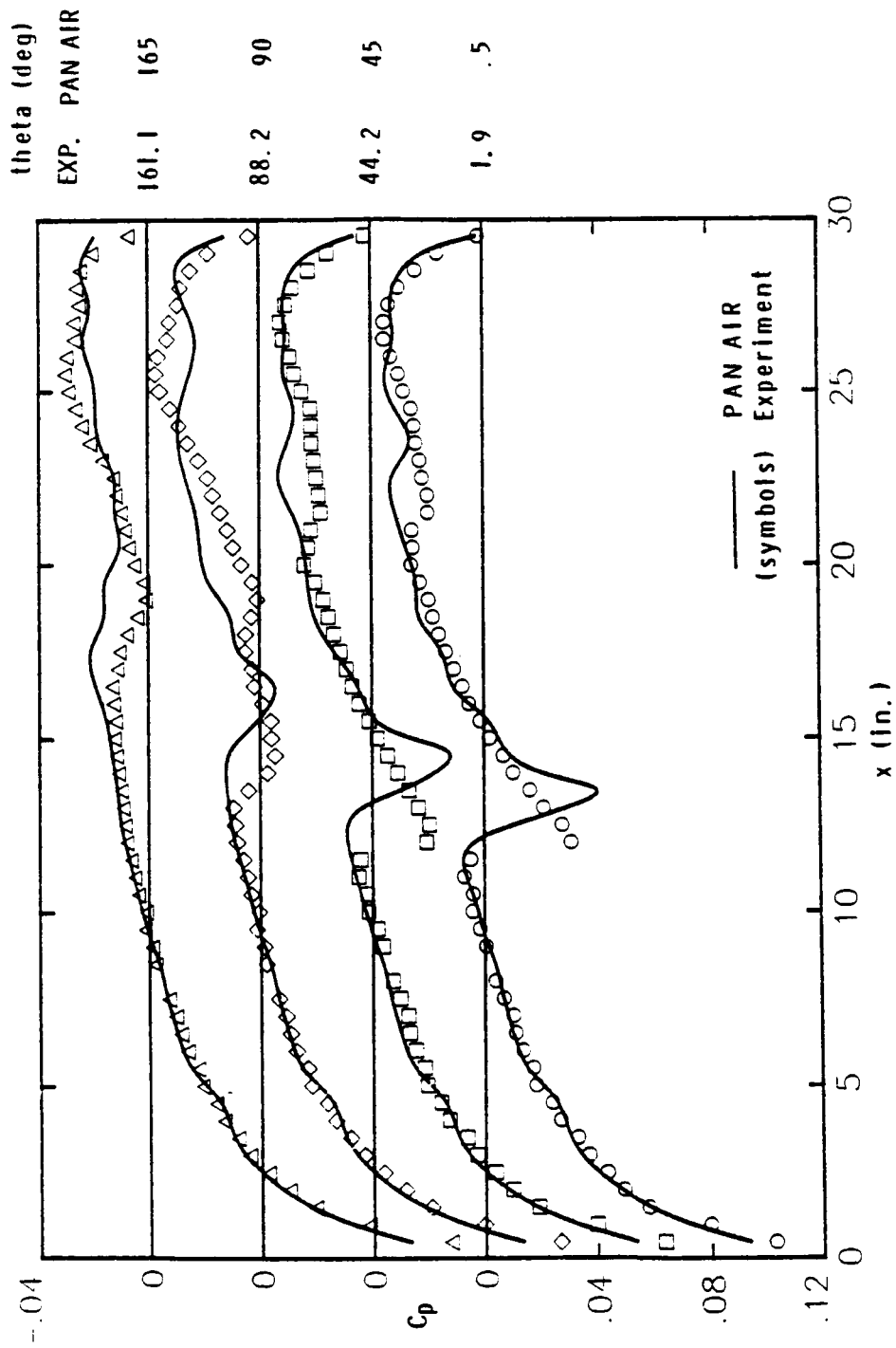
(b) SEP/ℓ = .20

Figure 26. - Continued.
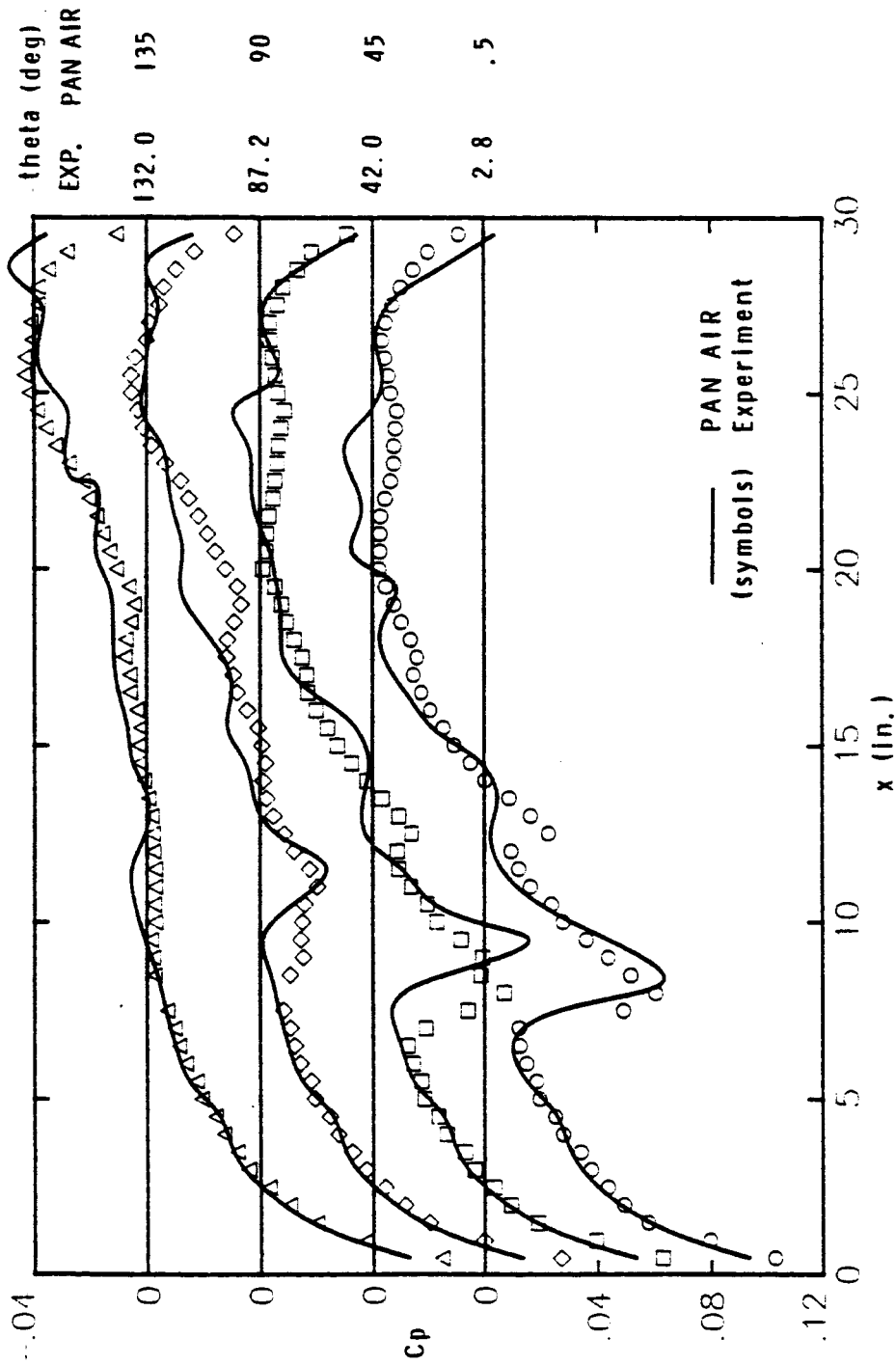
(c) SEP/ℓ = .13

Figure 26. - Continued.
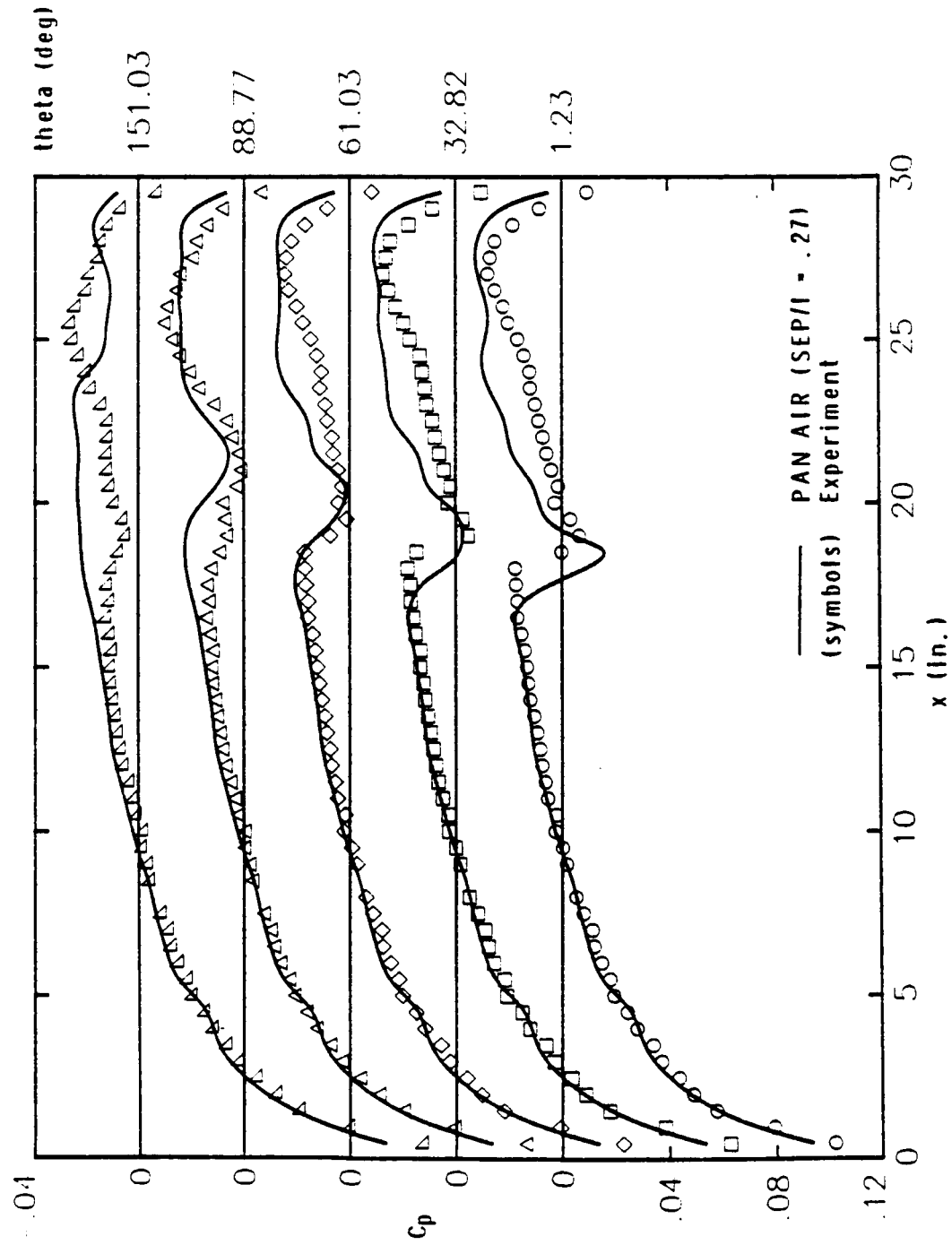
Figure 27. - Pressure distribution comparison between experiment (SEP/l = .30) and PAN AIR (SEP/ℓ = .27).
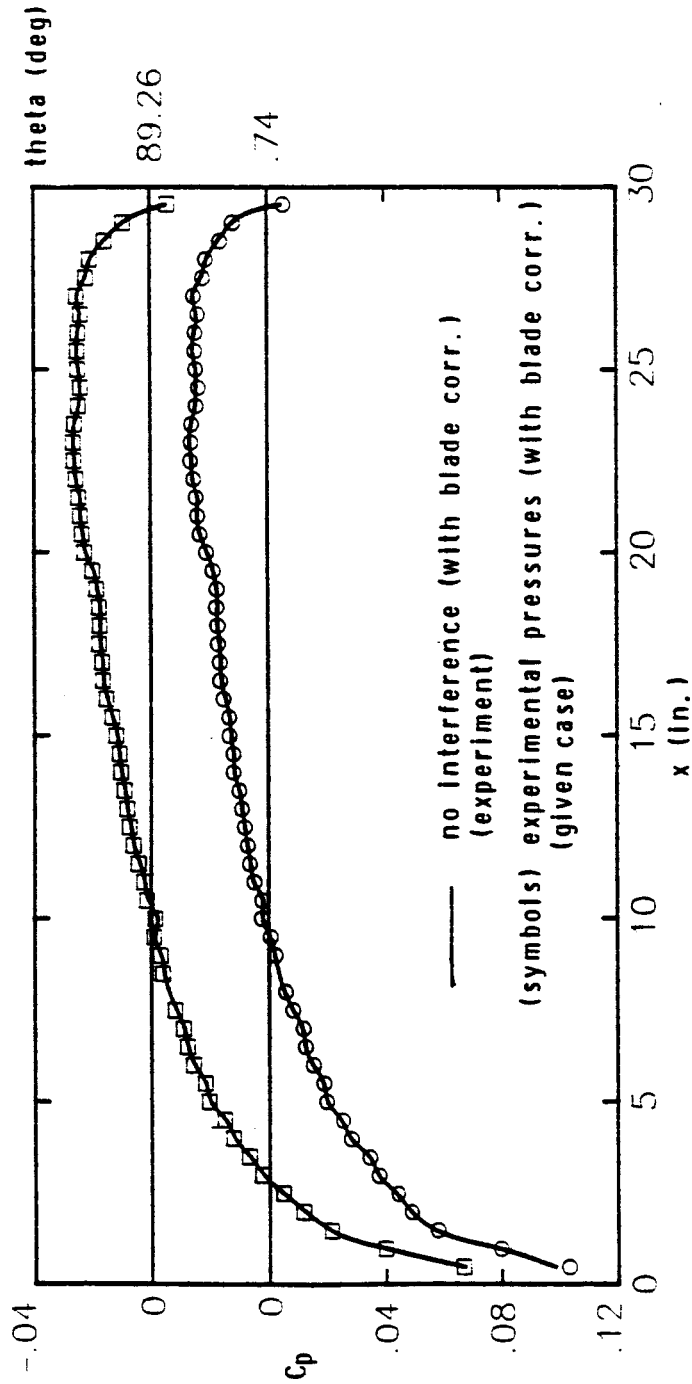
(a) SEP/ℓ = .50

Figure 28. - Experimental pressure distributions at different values of SEP/ℓ (with blade correction).
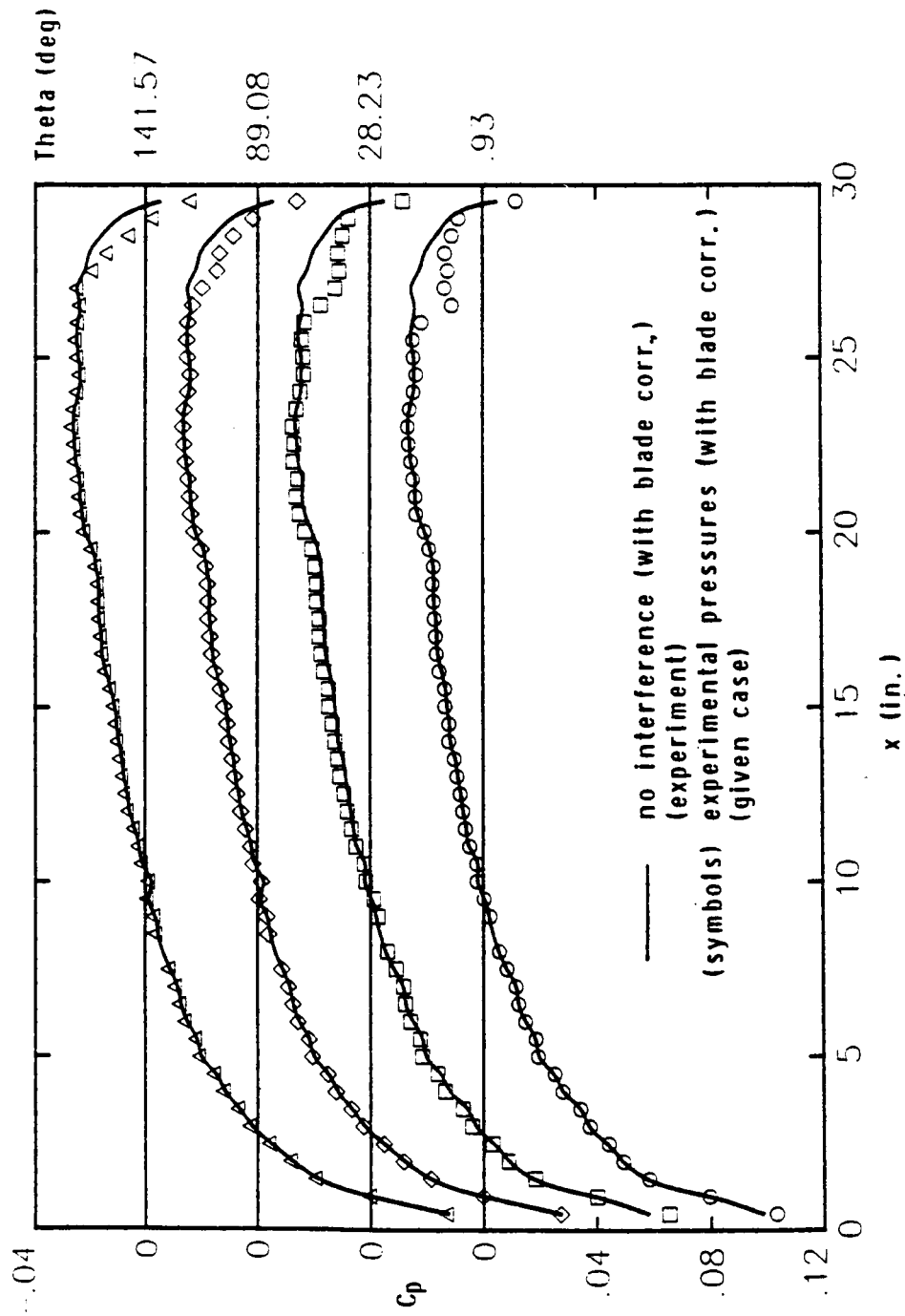
(b) SEP/ℓ = .40

Figure 28. - Continued.
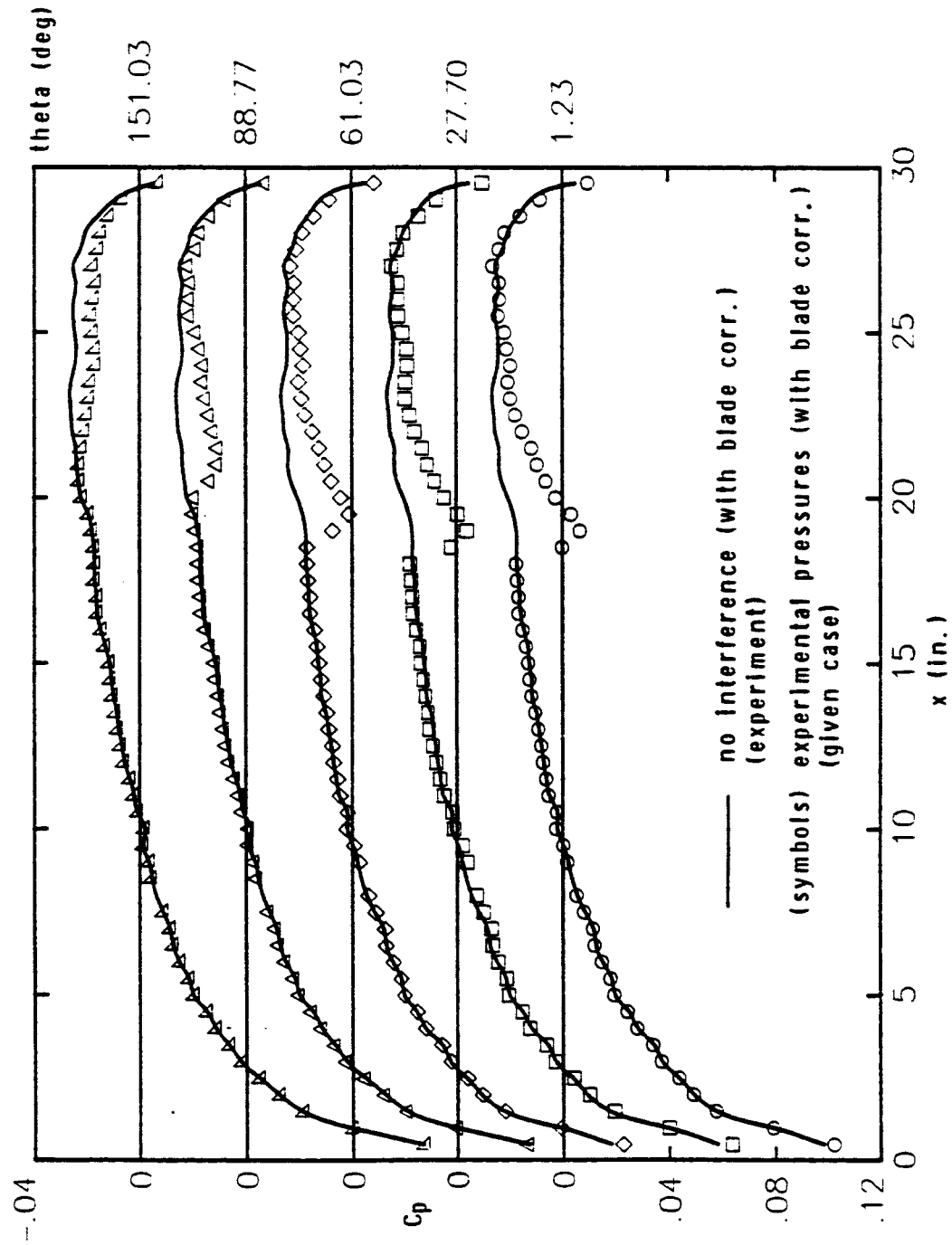
(c) SEP/ℓ = .30

Figure 28. - Continued.
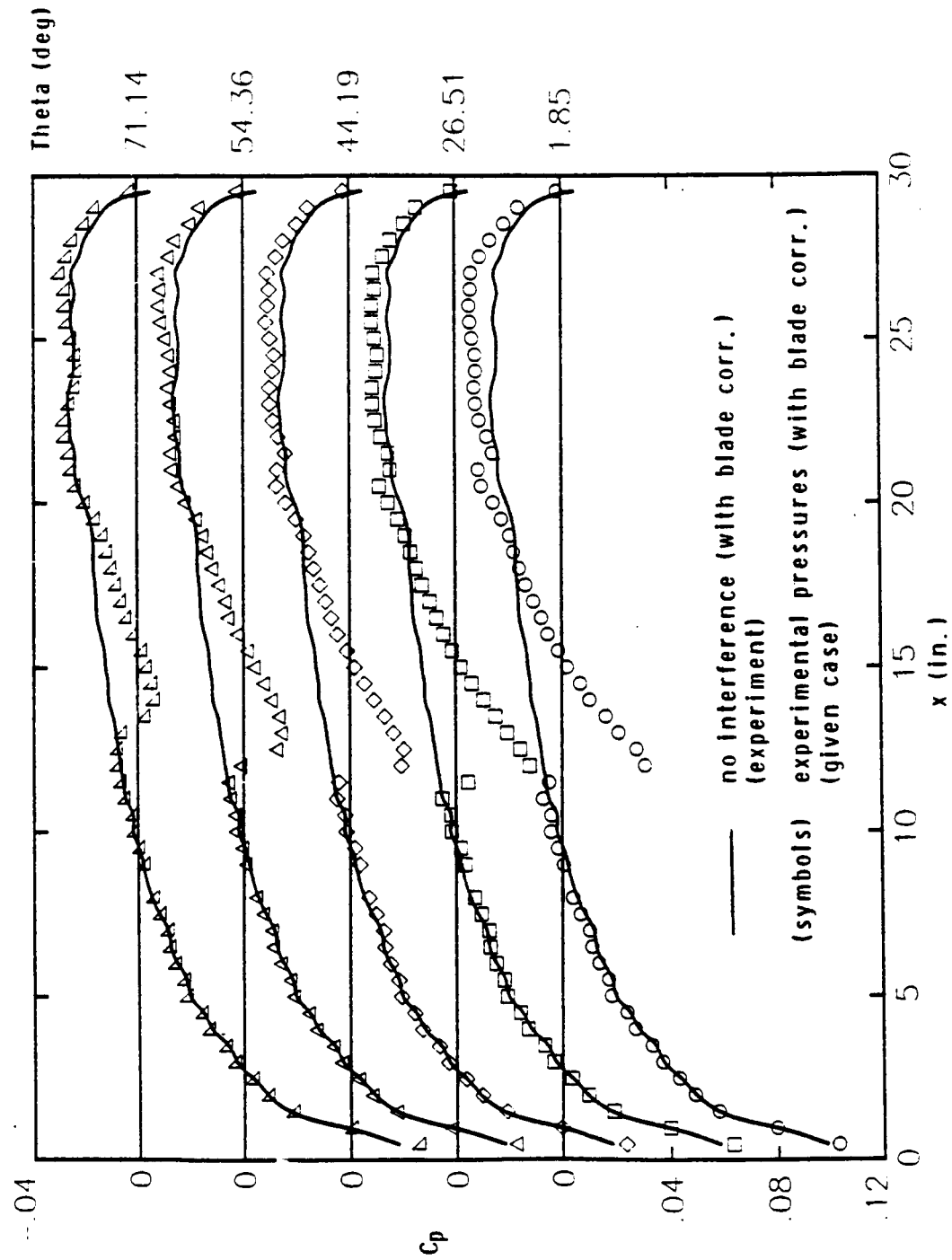
(d) SEP/ℓ = .20

Figure 28. – Continued.
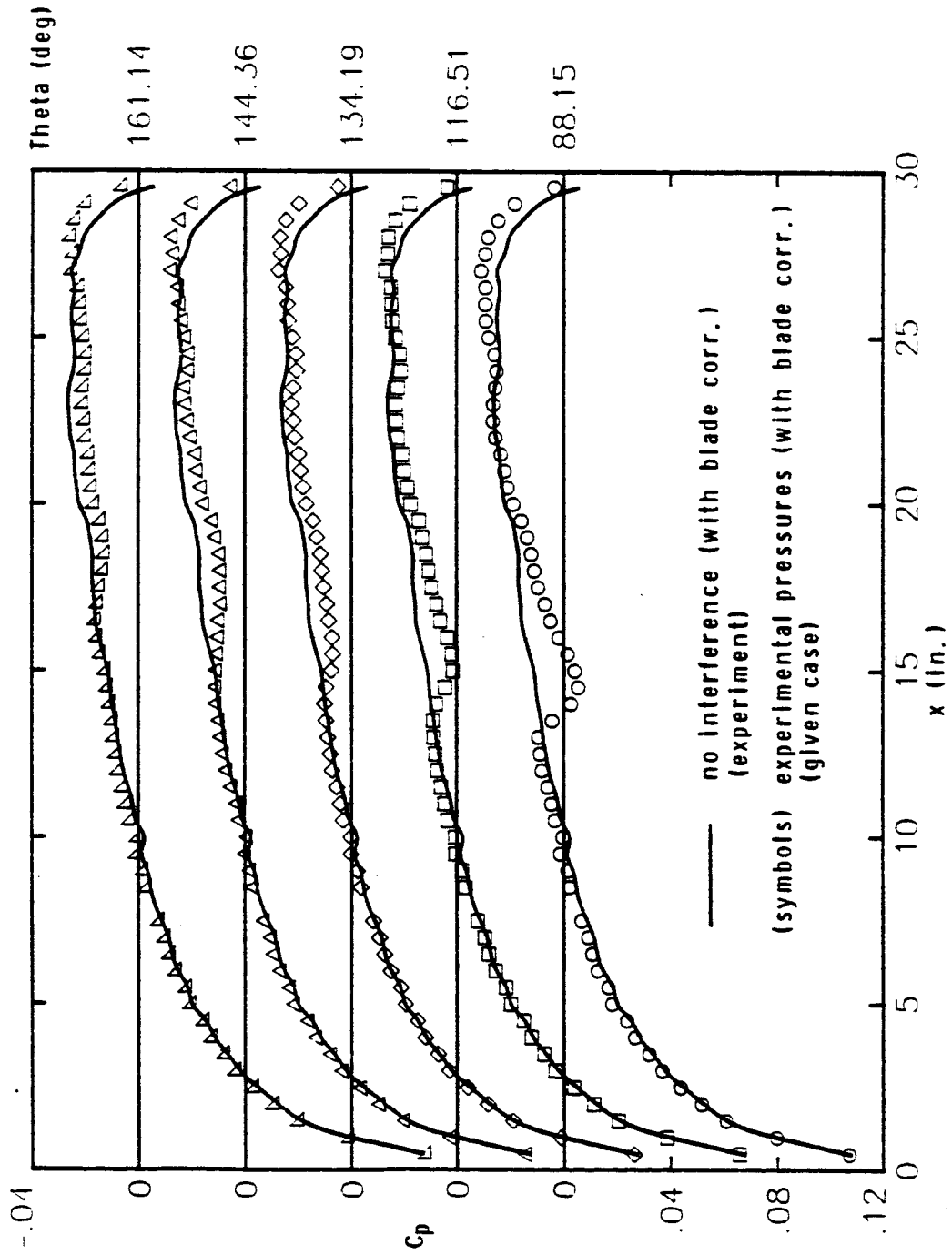
(d) Concluded (SEP/ℓ = .20)

Figure 28. - Continued.
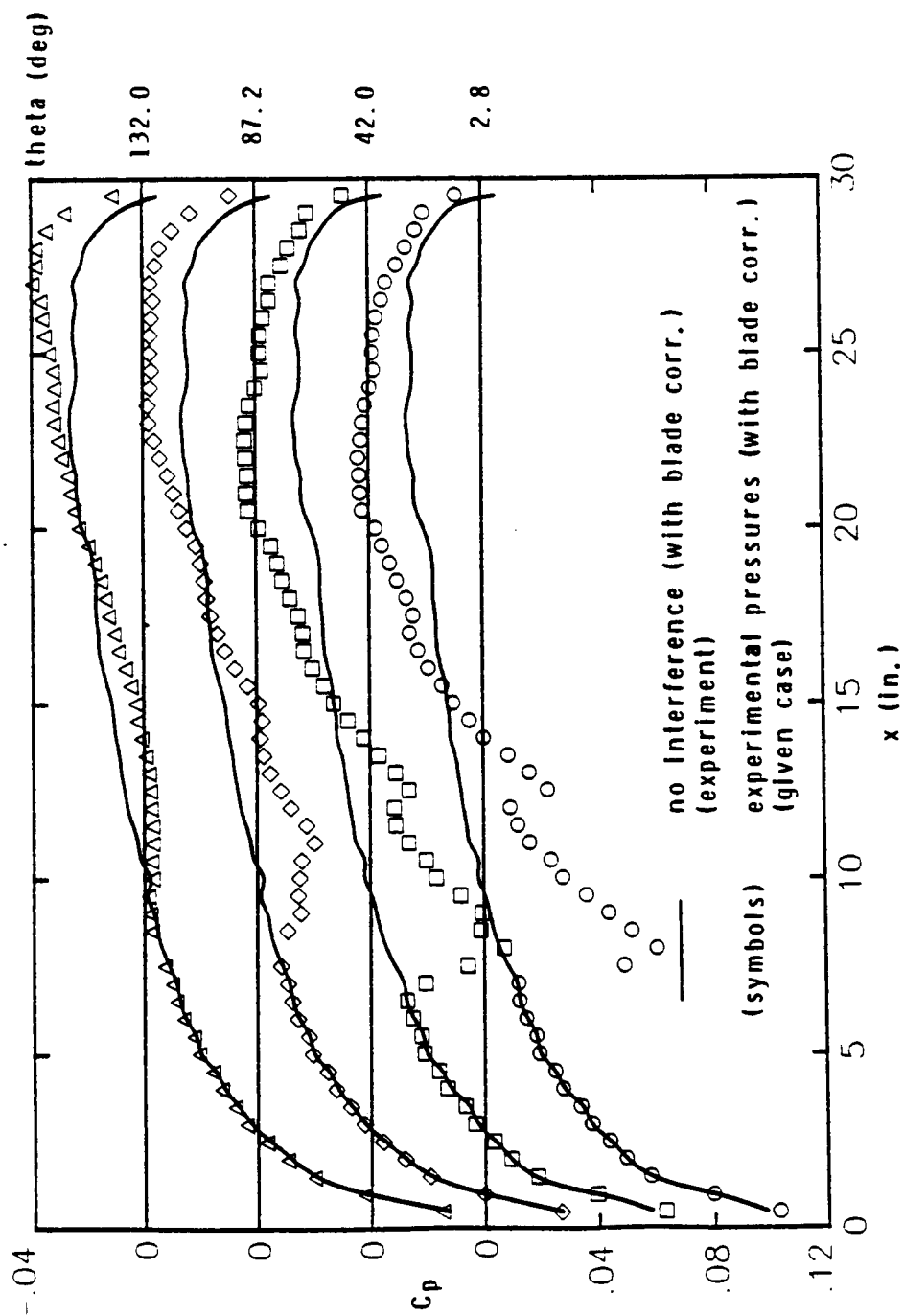
(e) SEP/ℓ = .13

Figure 28. - Concluded.
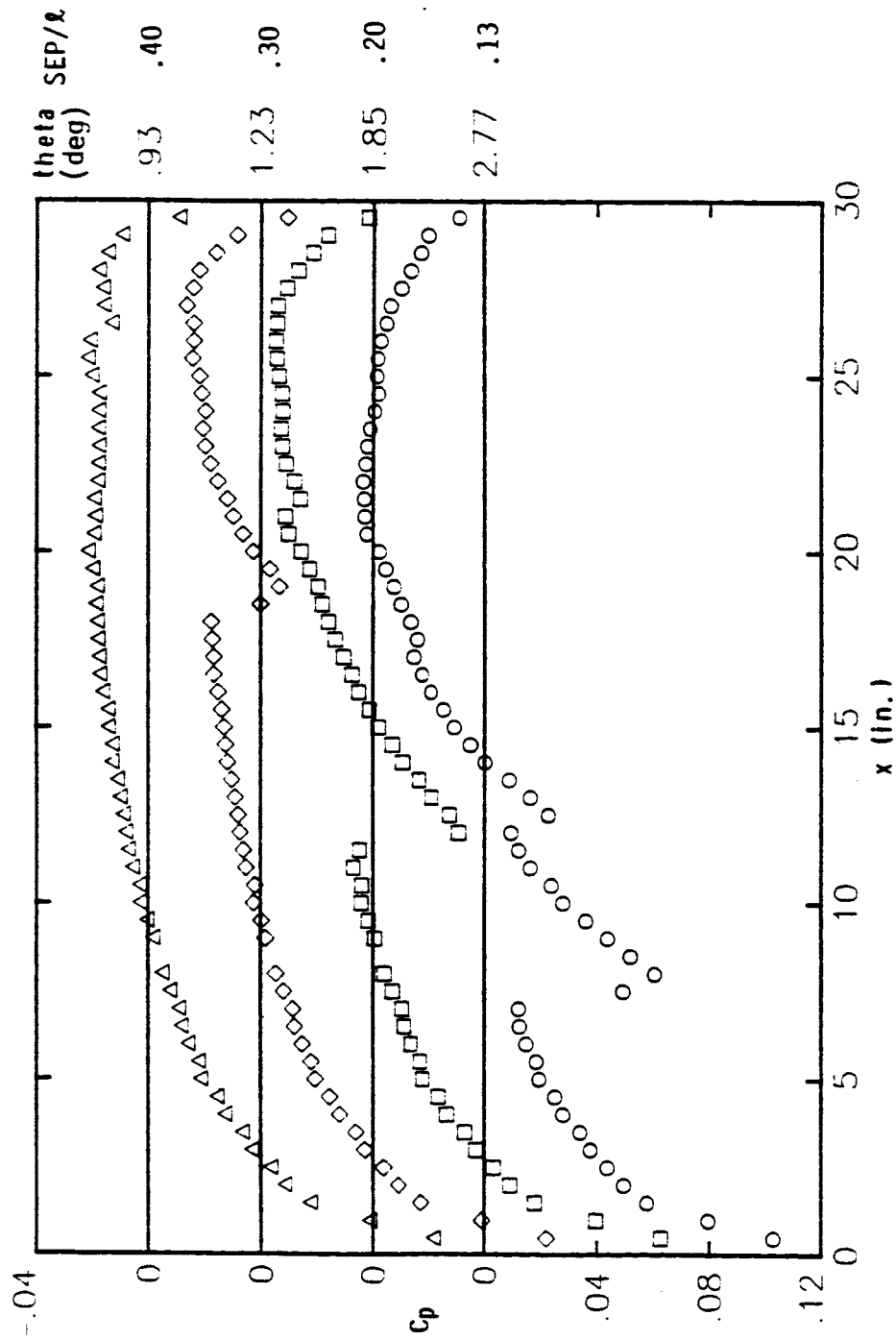
Figure 29.- Pressure distributions at four different lateral separations (with blade correction).
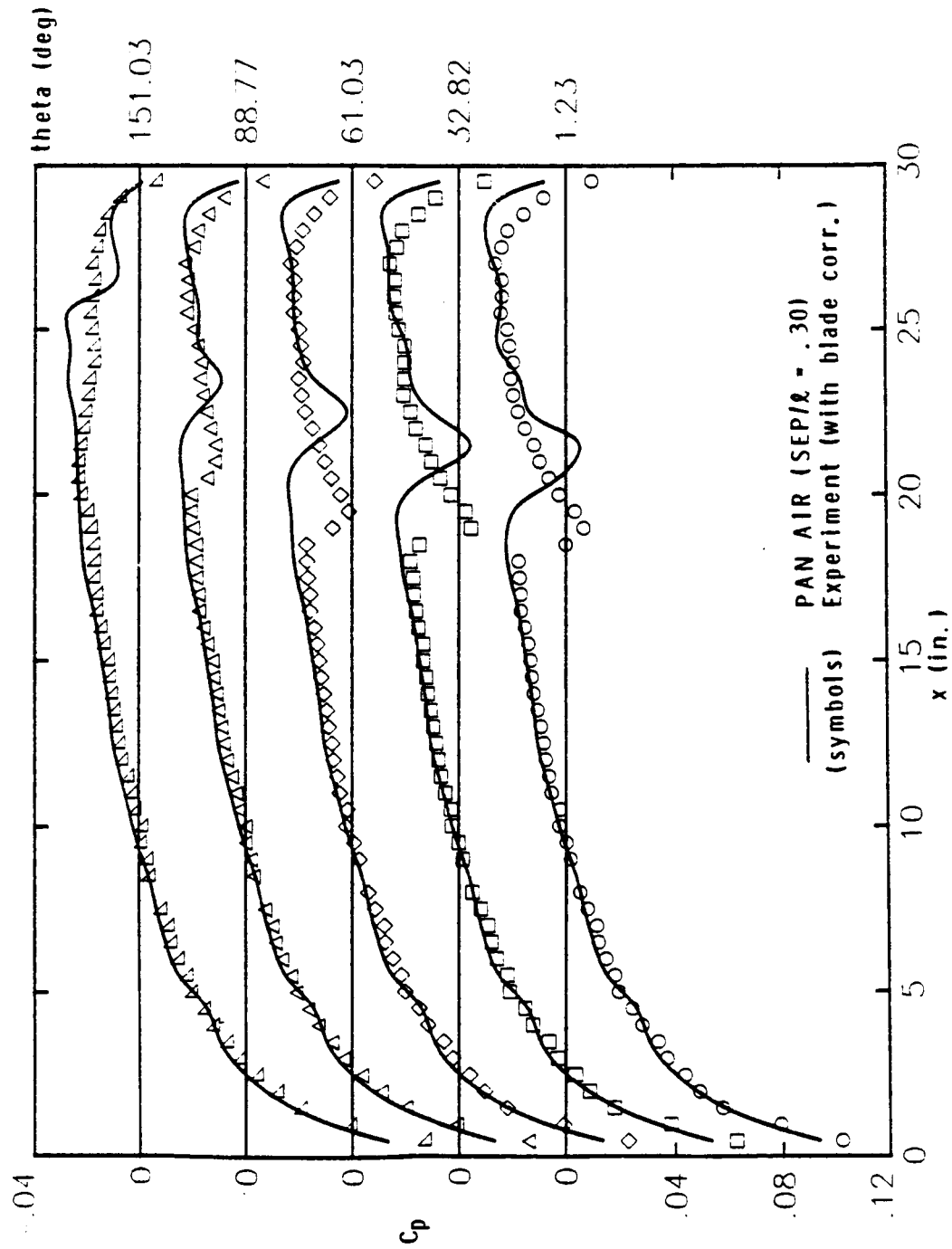
Figure 30. - Pressure distribution comparisons between experiment (with blade correction) and PAN AIR.

theta (deg)	
EXP.	PAN AIR
161.1.	165
88.2	90
44.2	45
1.9	.5

PAN AIR (SEP/ℓ = .20)

(symbols) Experiment (with blade corr.)
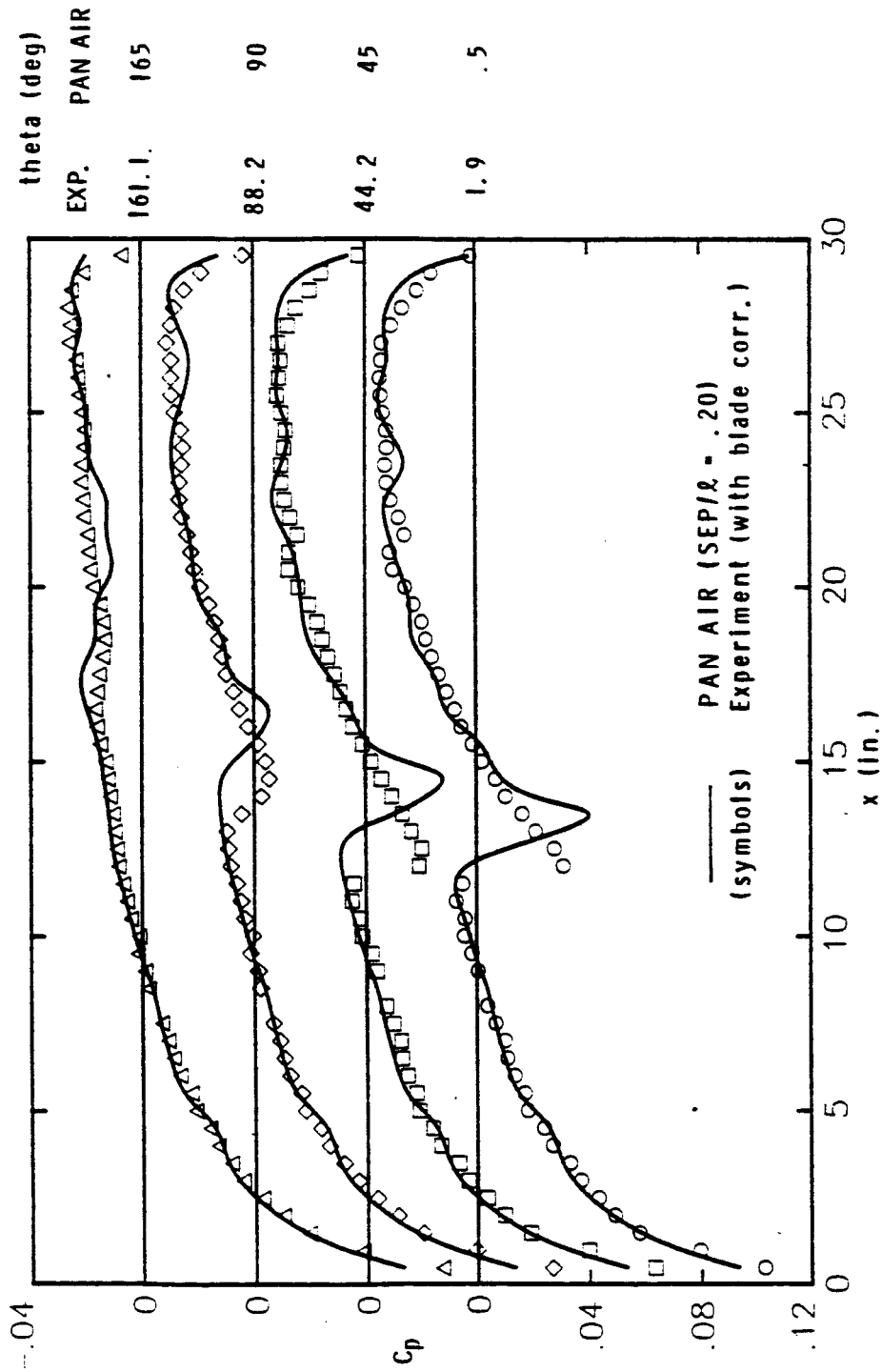
(b) SEP/ℓ = .20

Figure 30. - Continued.
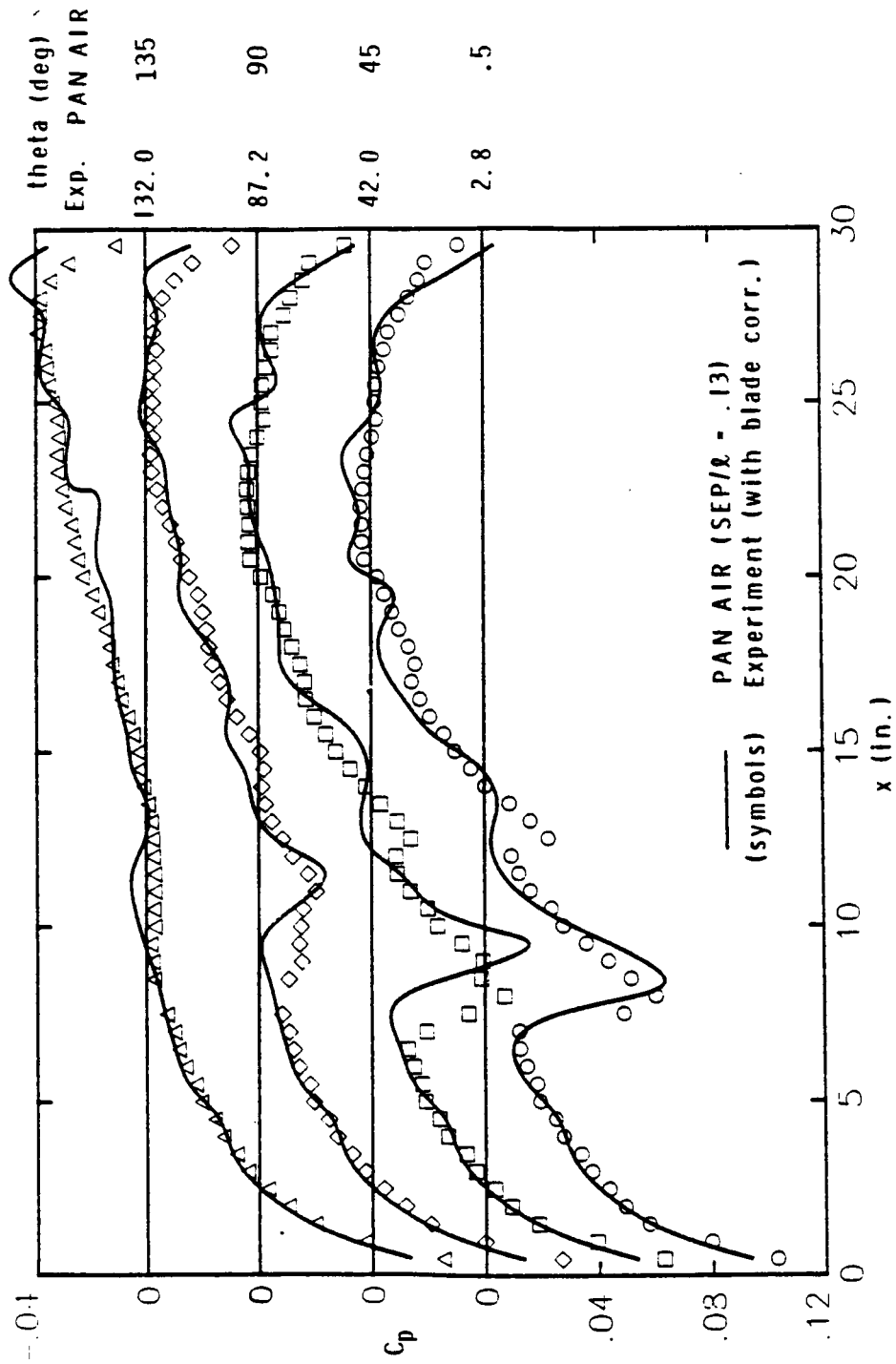
(c) SEP/ℓ = .13

Figure 30. – Continued.

107
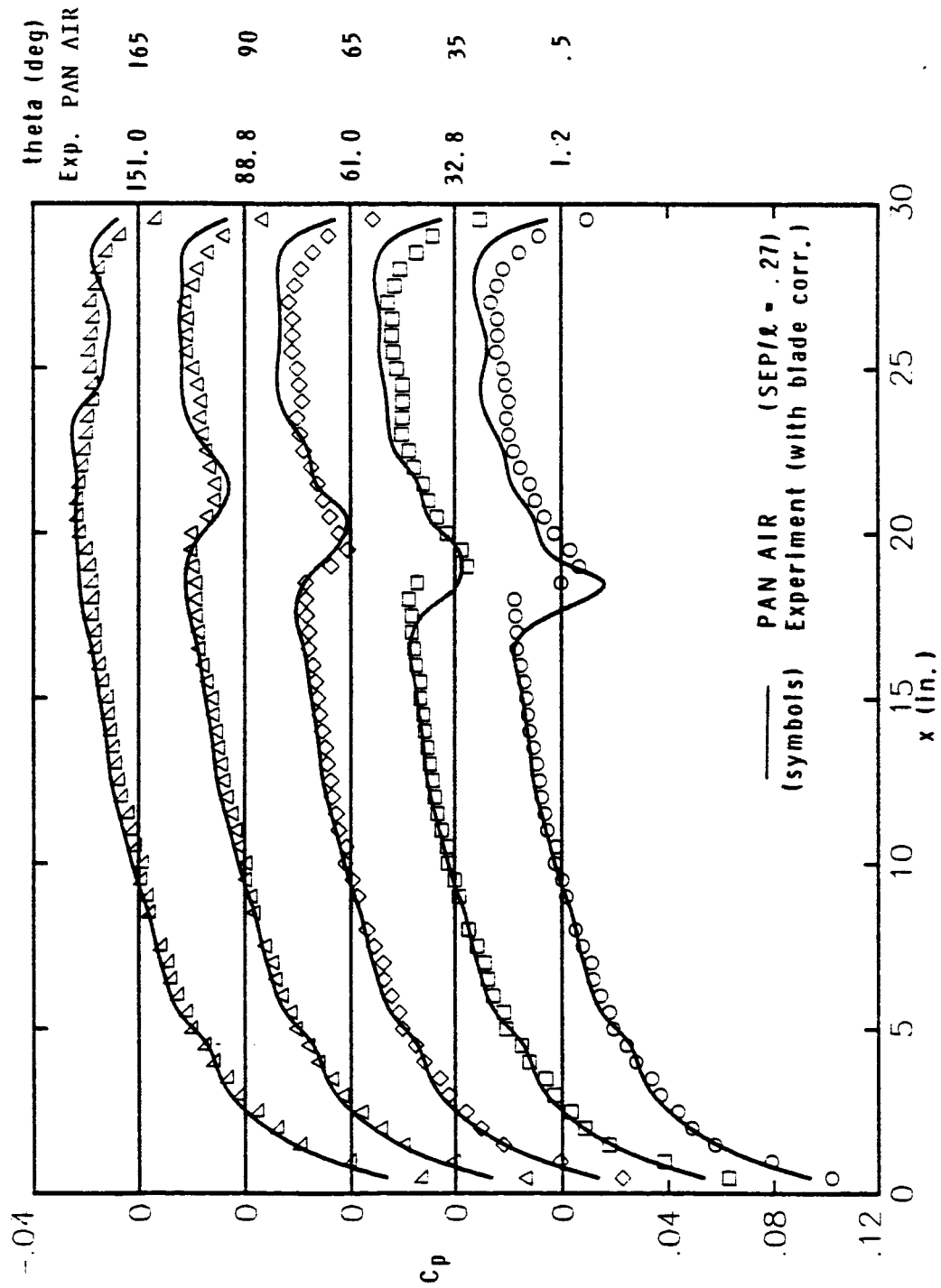
Figure 31.- Pressure distribution comparison between experiment (with blade correction, SEP/ℓ = .30) and PAN AIR (SEP/ℓ = .27)
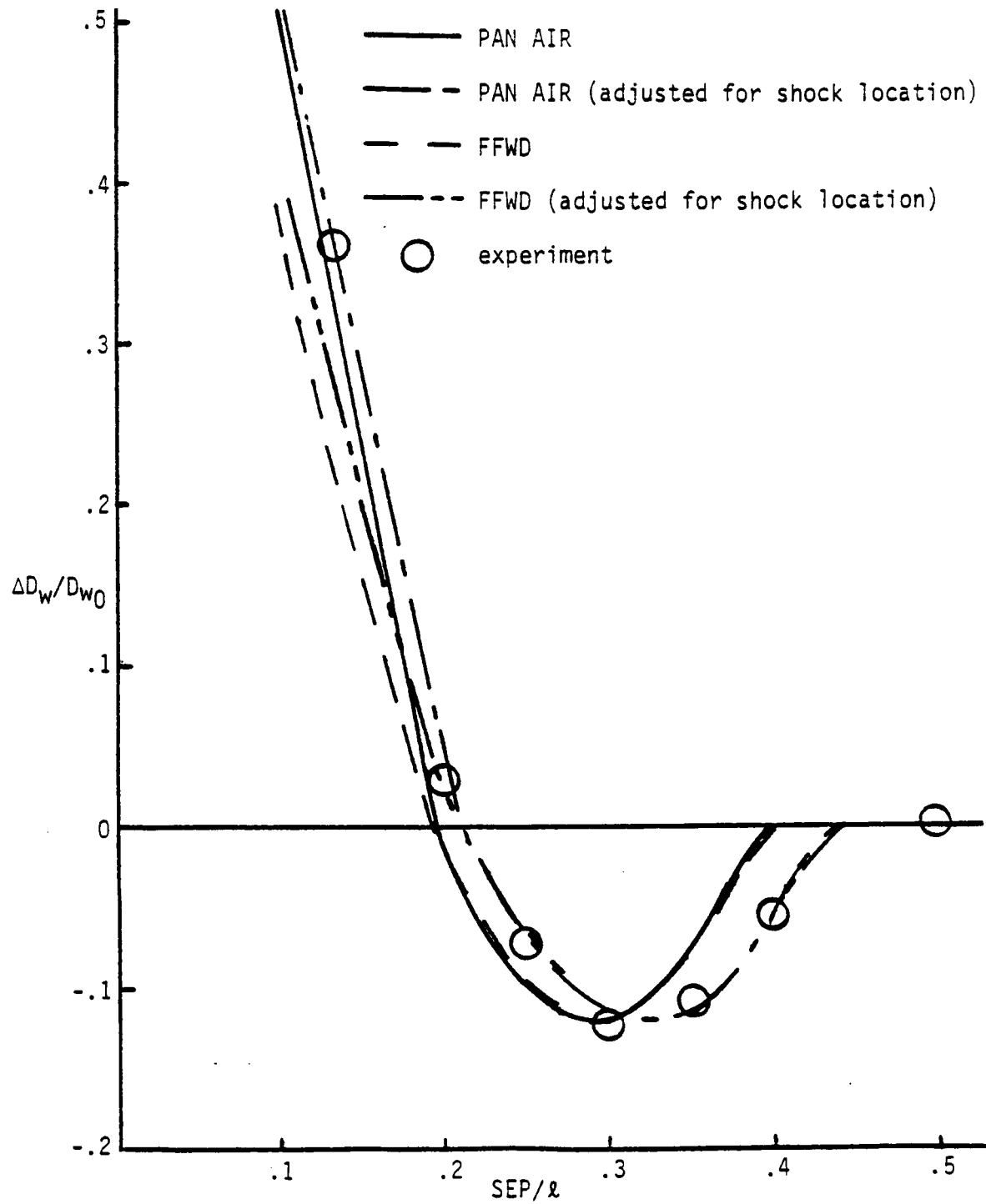
Figure 32.- Comparison of $\Delta D_w/D_{w_0}$ versus separation in body lengths for the 30" body between experiment, PAN AIR, and FFWD (SKEW/ℓ = 0).
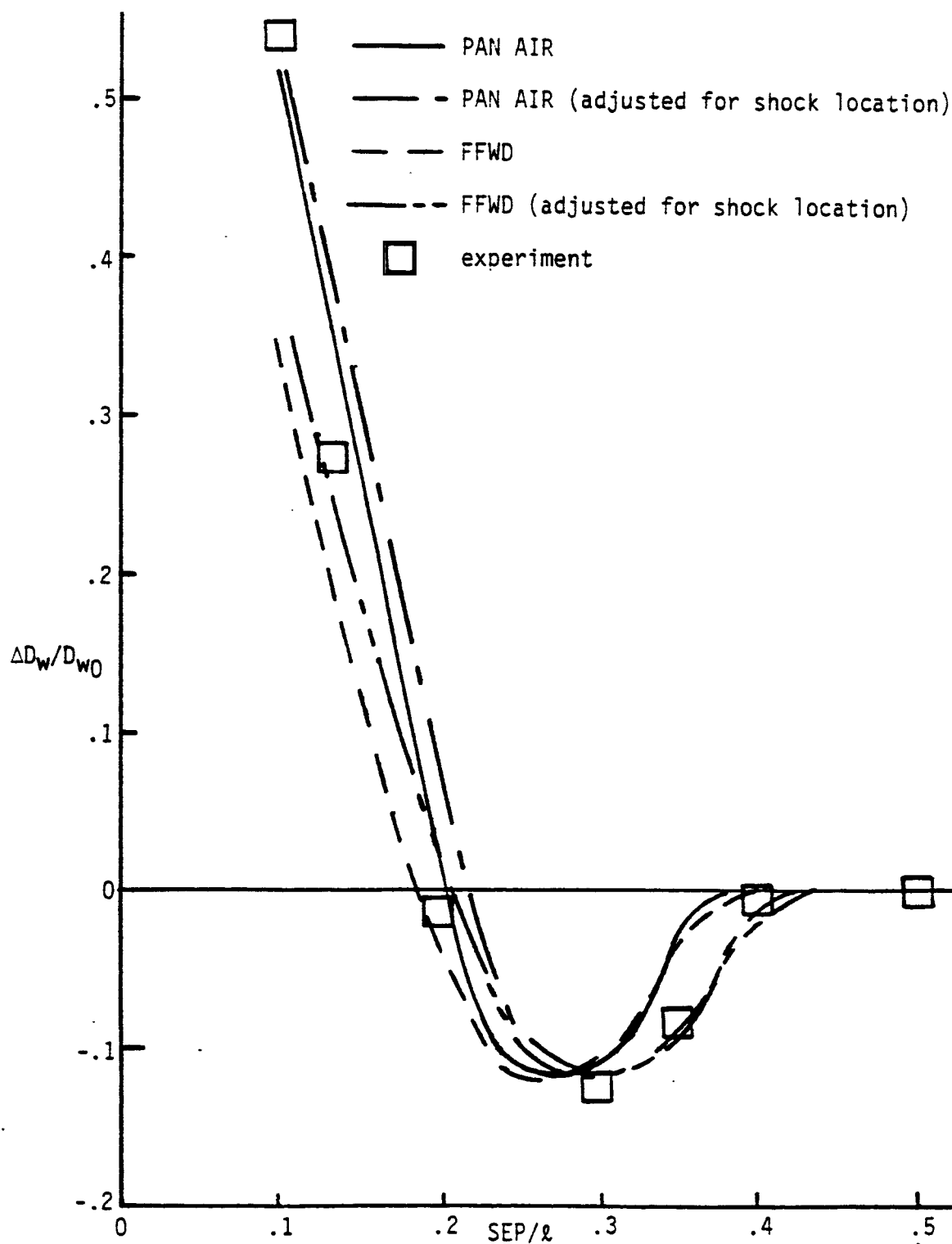
Figure 33.- Comparison of $\Delta D_W/D_{WO}$ versus separation in body lengths for the cutoff body between experiment, PAN AIR, and FFWD (SKEW/ℓ = 0).
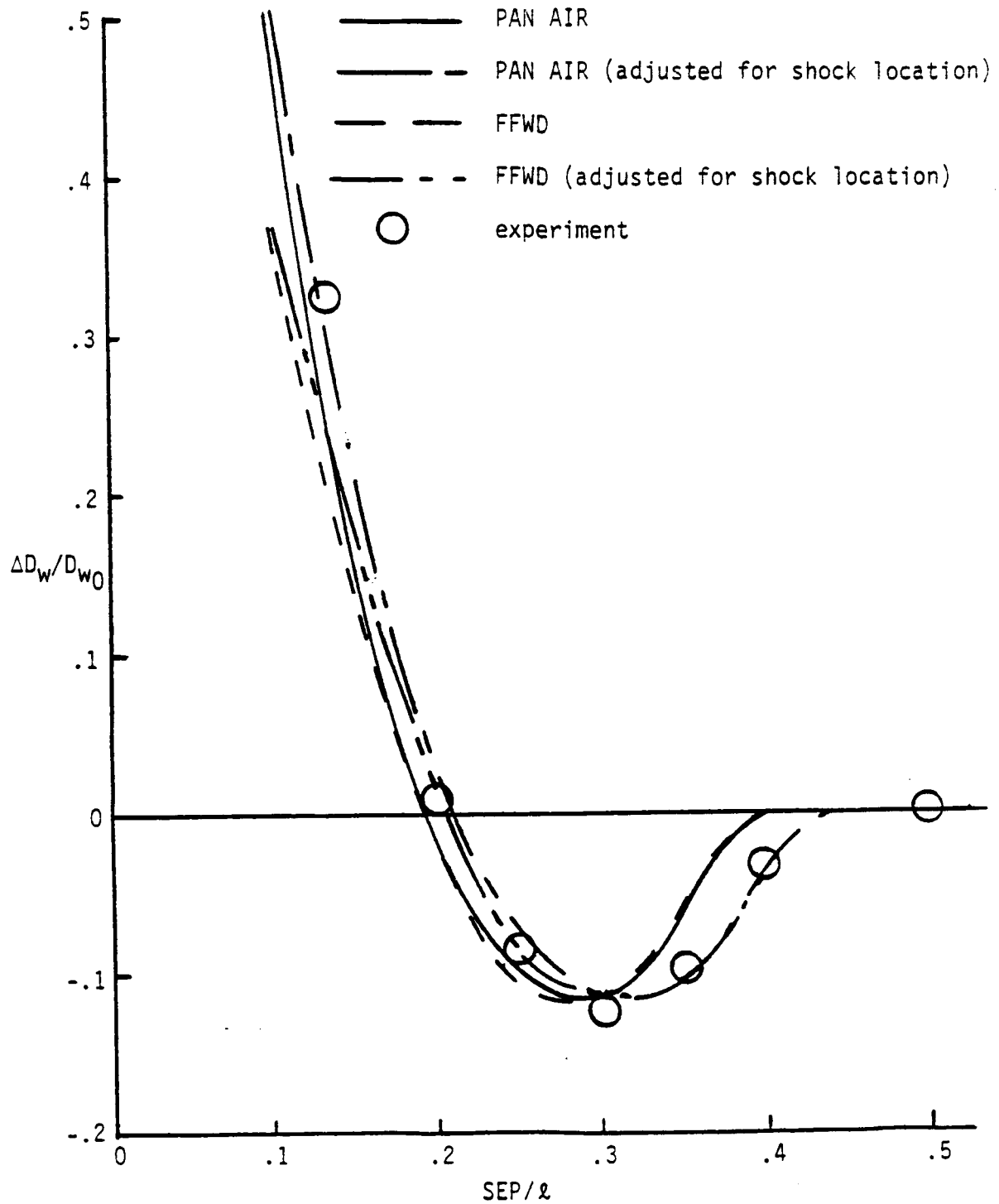
Figure 34.- Comparison of $\Delta D_w/D_{w_0}$ versus separation in body lengths for the entire configuration between experiment, PAN AIR, and FFWD (SKEW/ℓ = 0).
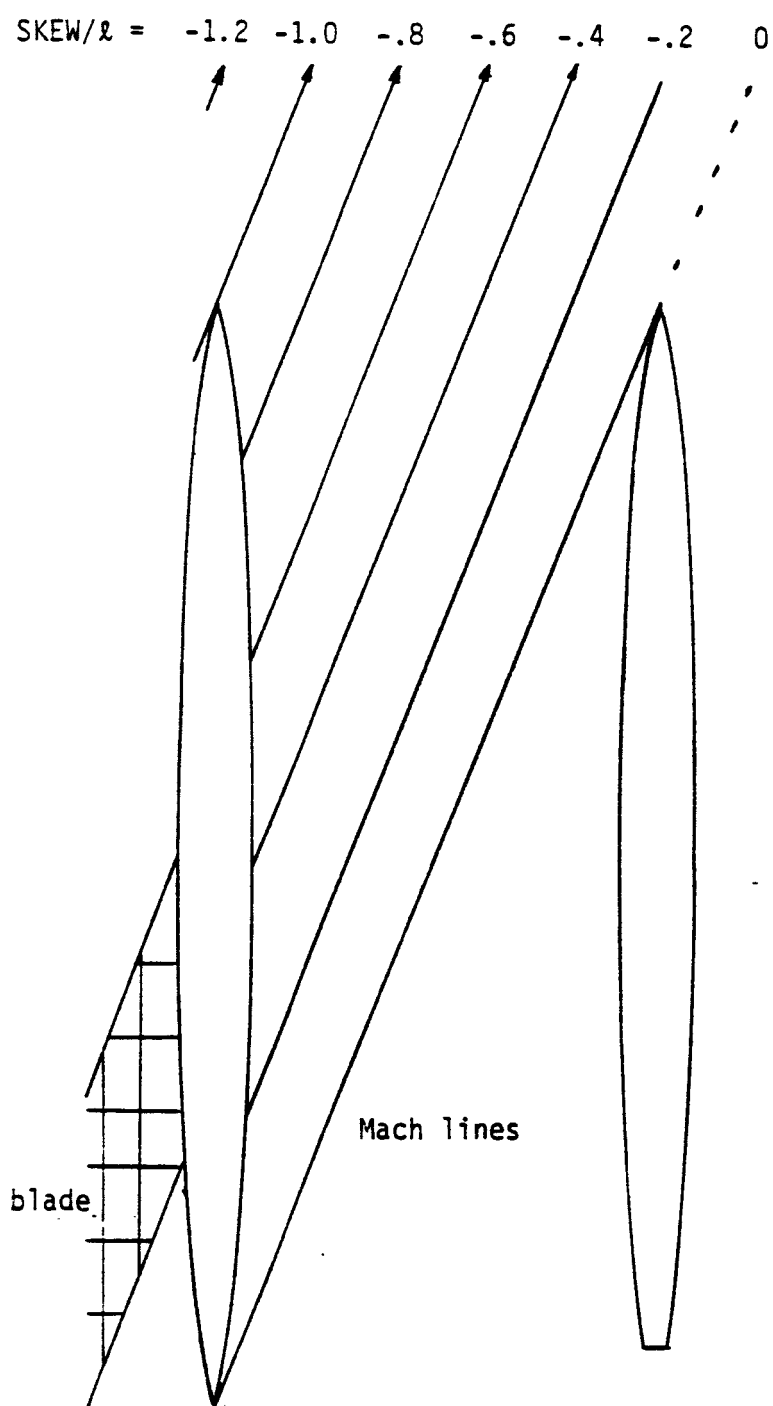
Figure 35.- Illustration of different positions of SKEW/ℓ at SEP/ℓ = .40.
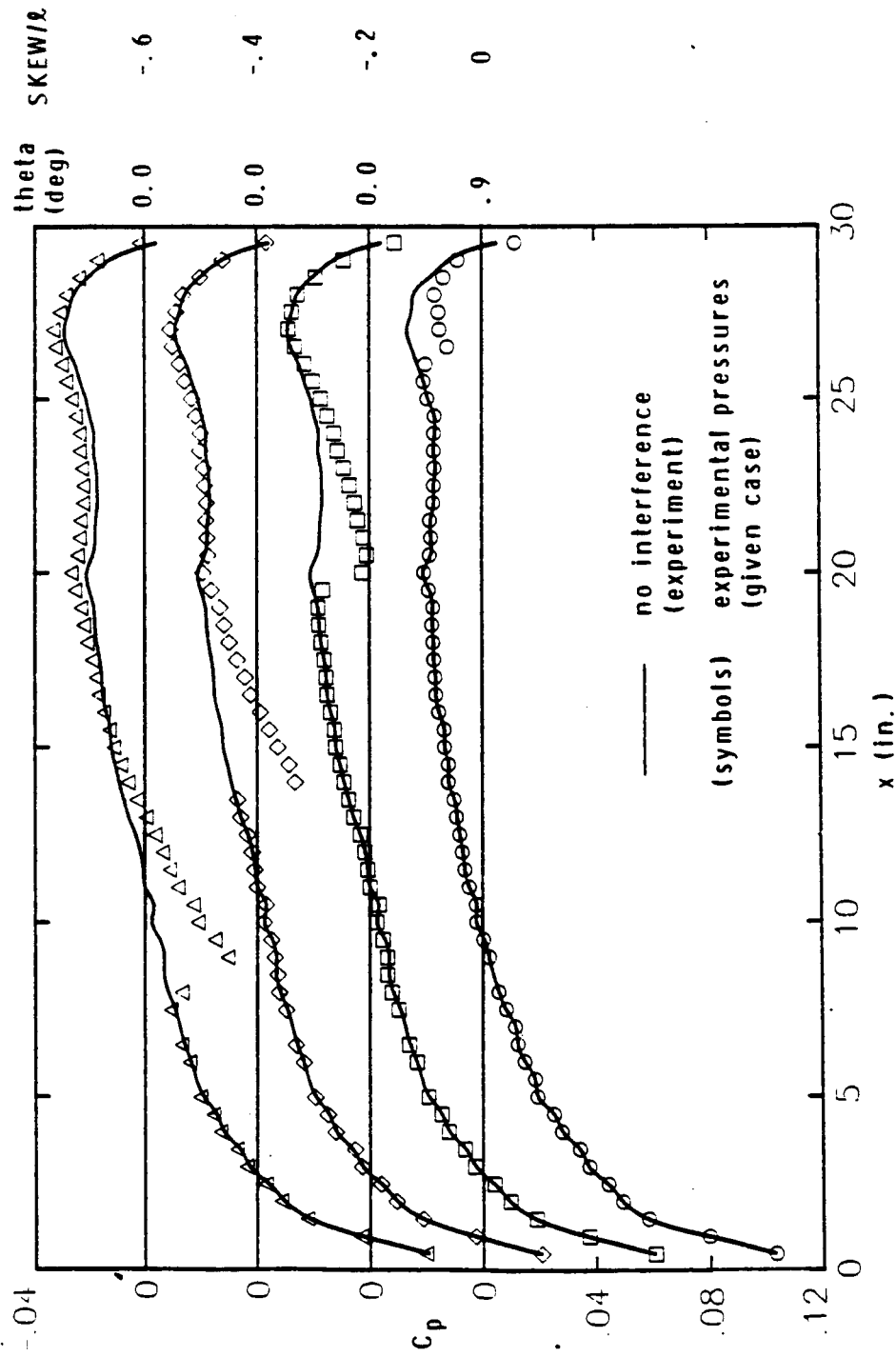
(a) SKEW/ℓ = 0 to -.6

Figure 36. - Experimental pressure distributions for different values of SKEW/ℓ at SEP/ℓ = .40.
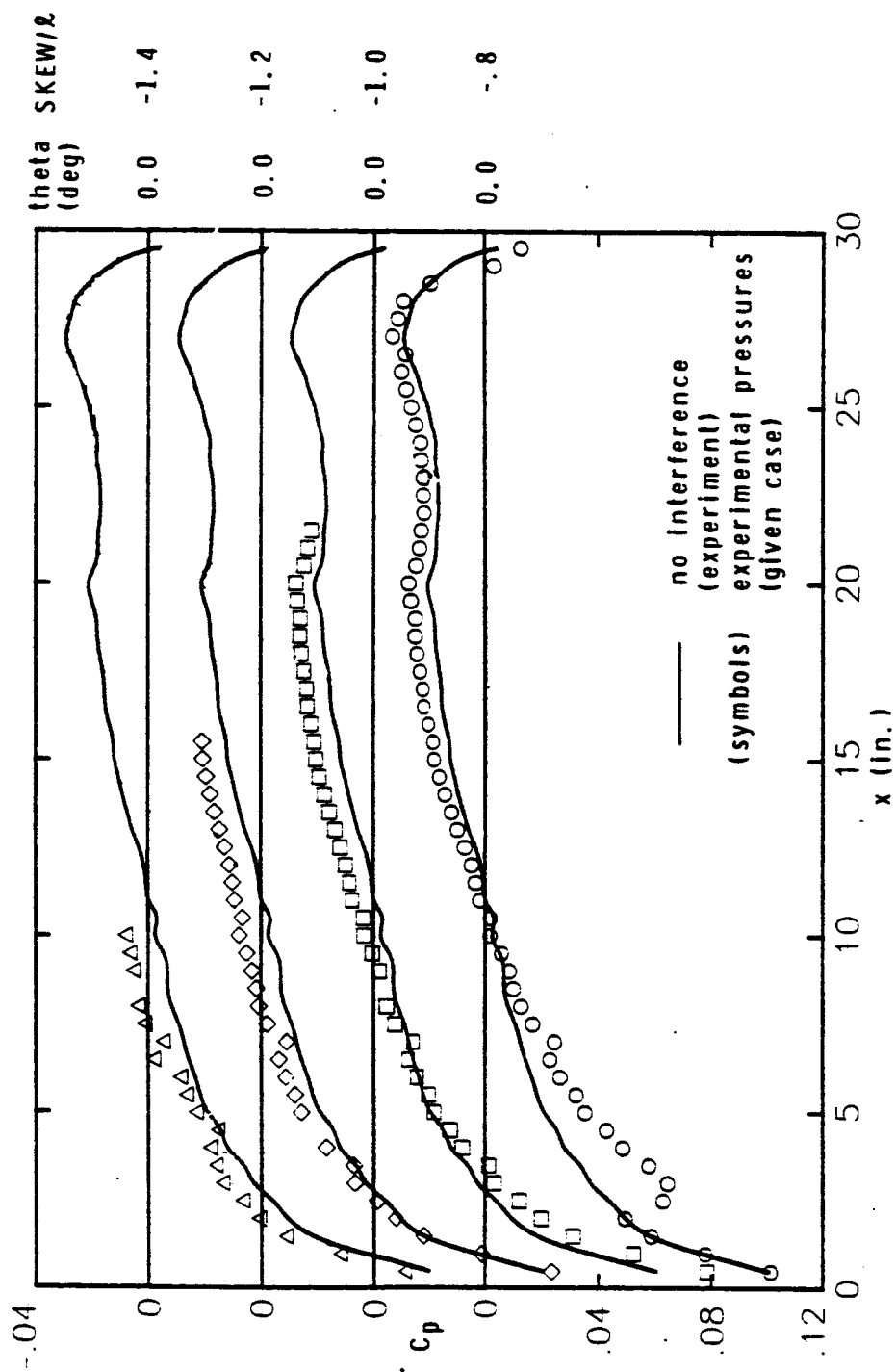
(b) SKEW/ℓ = -.8 to -1.4

Figure 36. - Concluded.
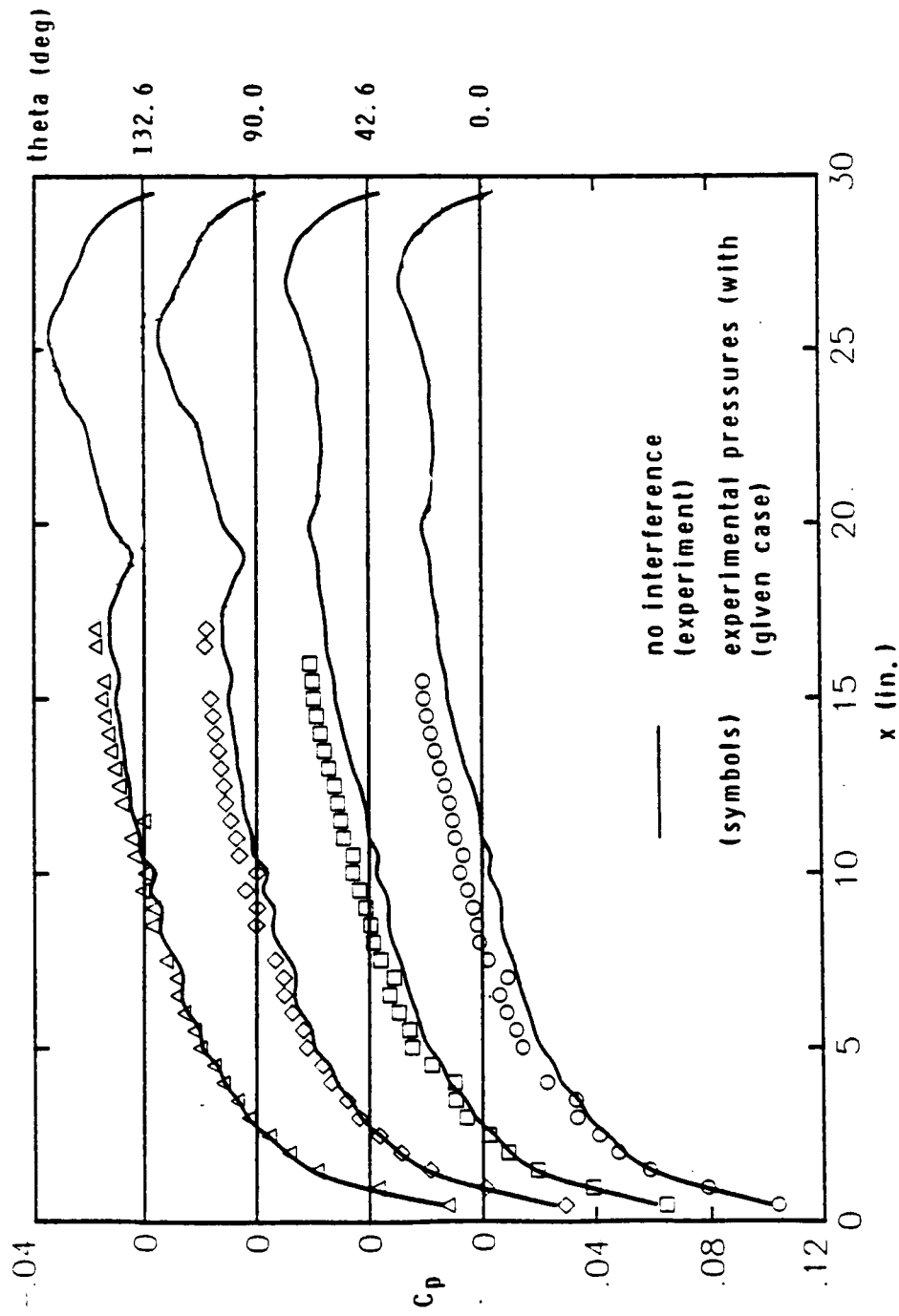
Figure 37.- Experimental pressure distributions around the body for SEP/ℓ = .40 and SKEW/ℓ = -1.2.
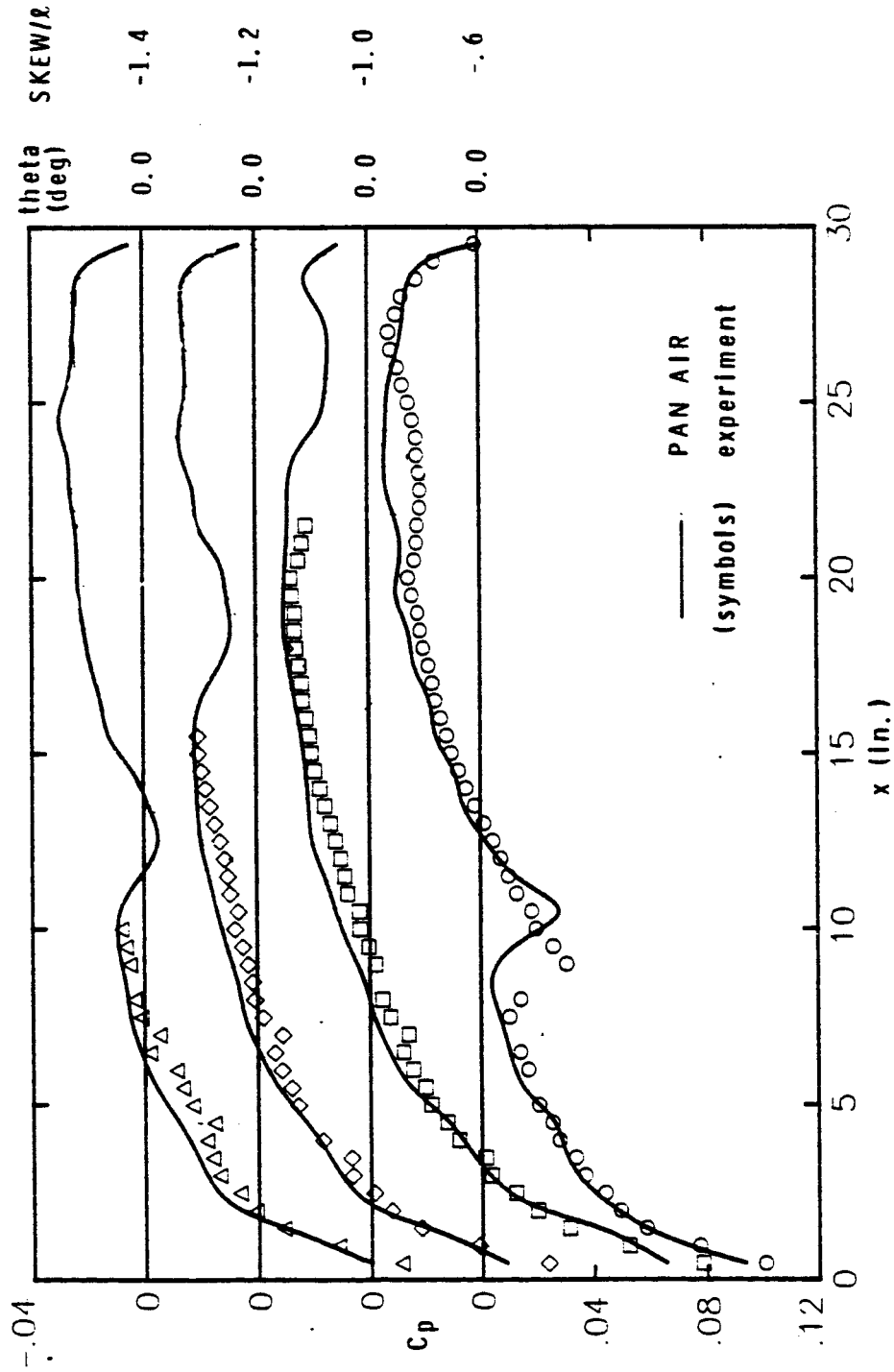
Figure 38. – Comparisons between experiment and PAN AIR of pressure distributions for SKEW/ℓ = –.6, –1.0, –1.2, and –1.4 at a SEP/ℓ of .40.
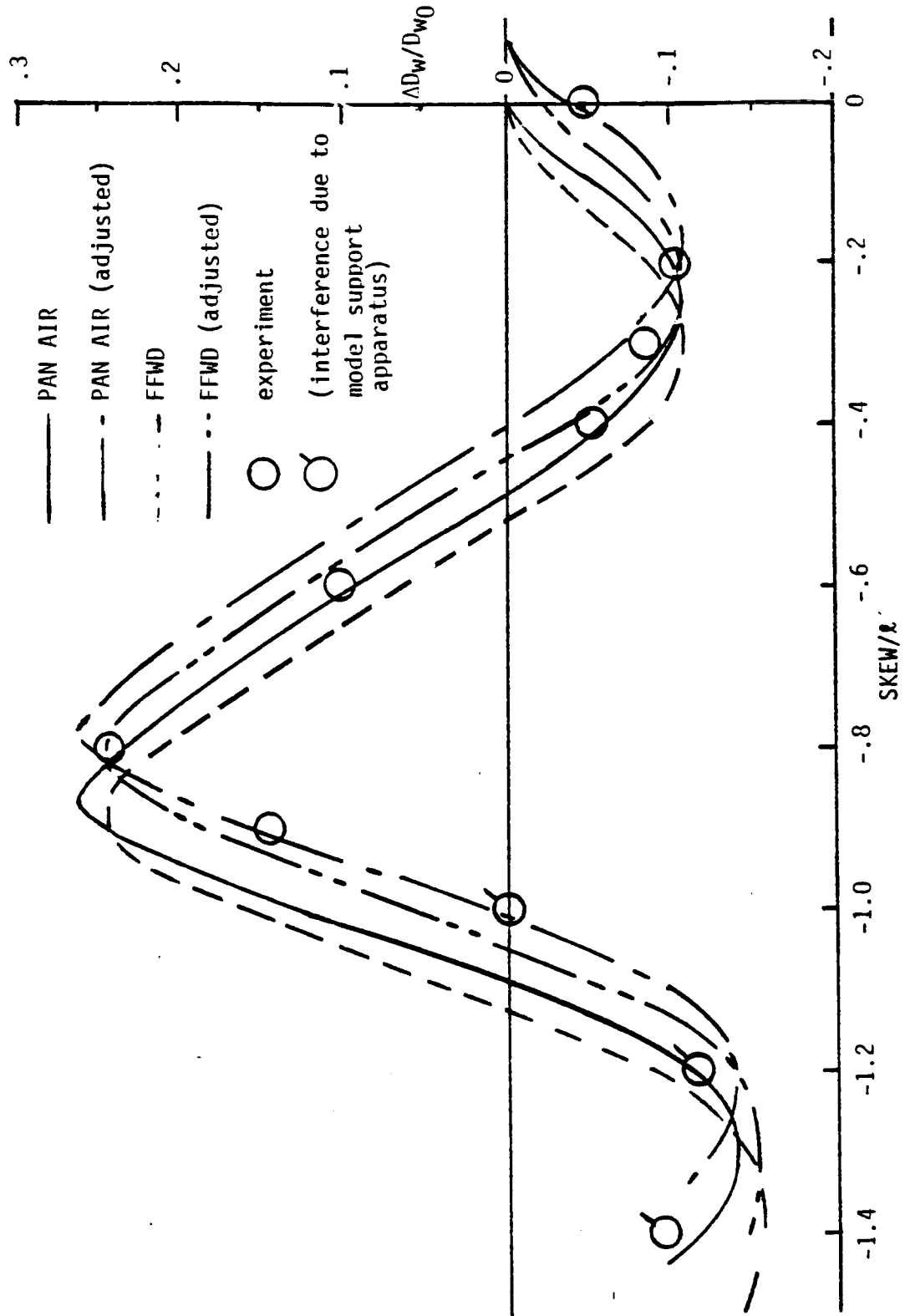
Figure 39.- Comparison of $\Delta D_W/D_{W_0}$ versus SKEW/ℓ at SEP/ℓ = .40 for the 30" body between experiment, PAN AIR, and FFWD.
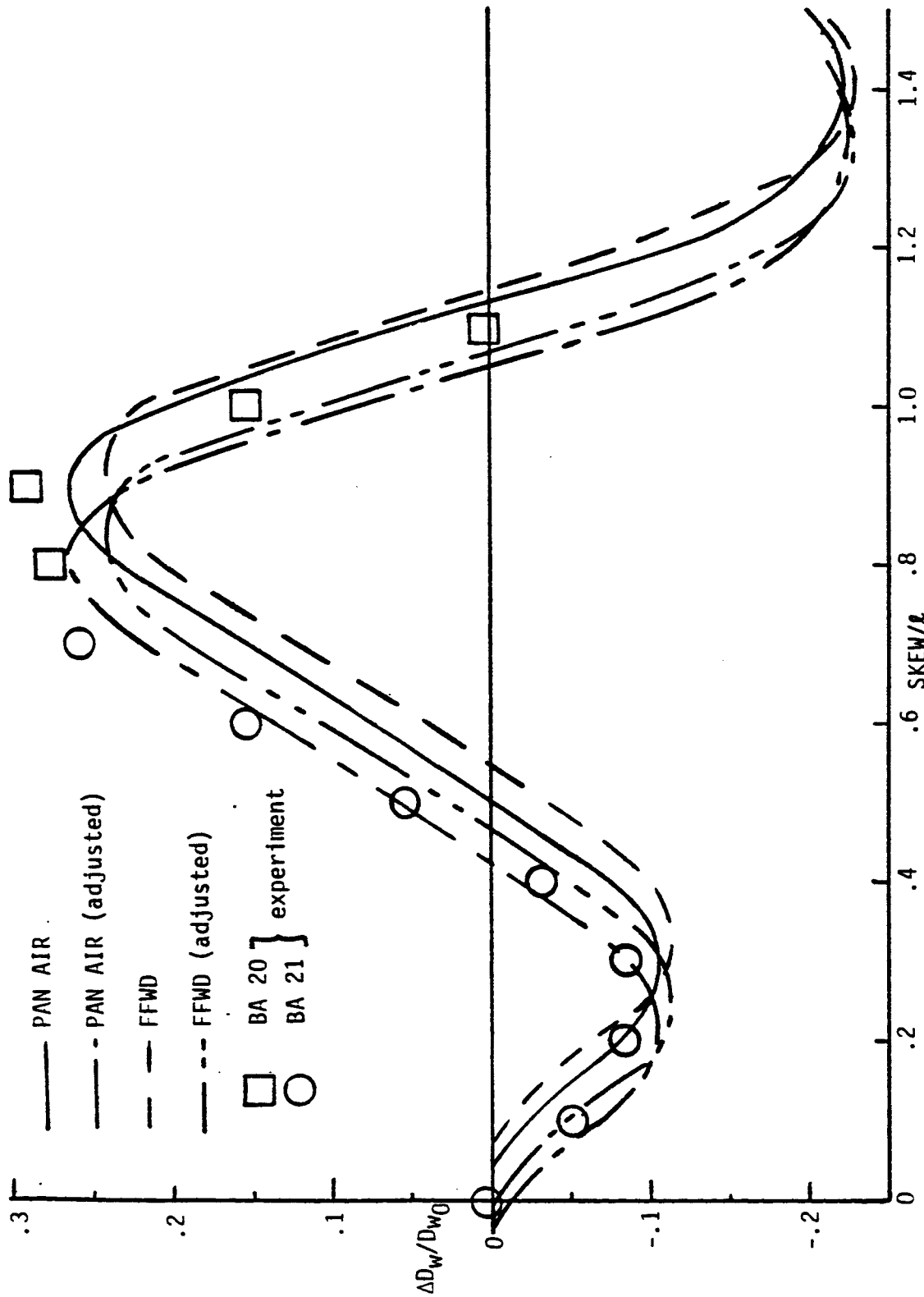
Figure 40.- Comparison of $\Delta D_W/D_{W_0}$ versus SKEW/ℓ at SEP/ℓ = .40 for the cutoff body between experiment, PAN AIR, and FFWD.
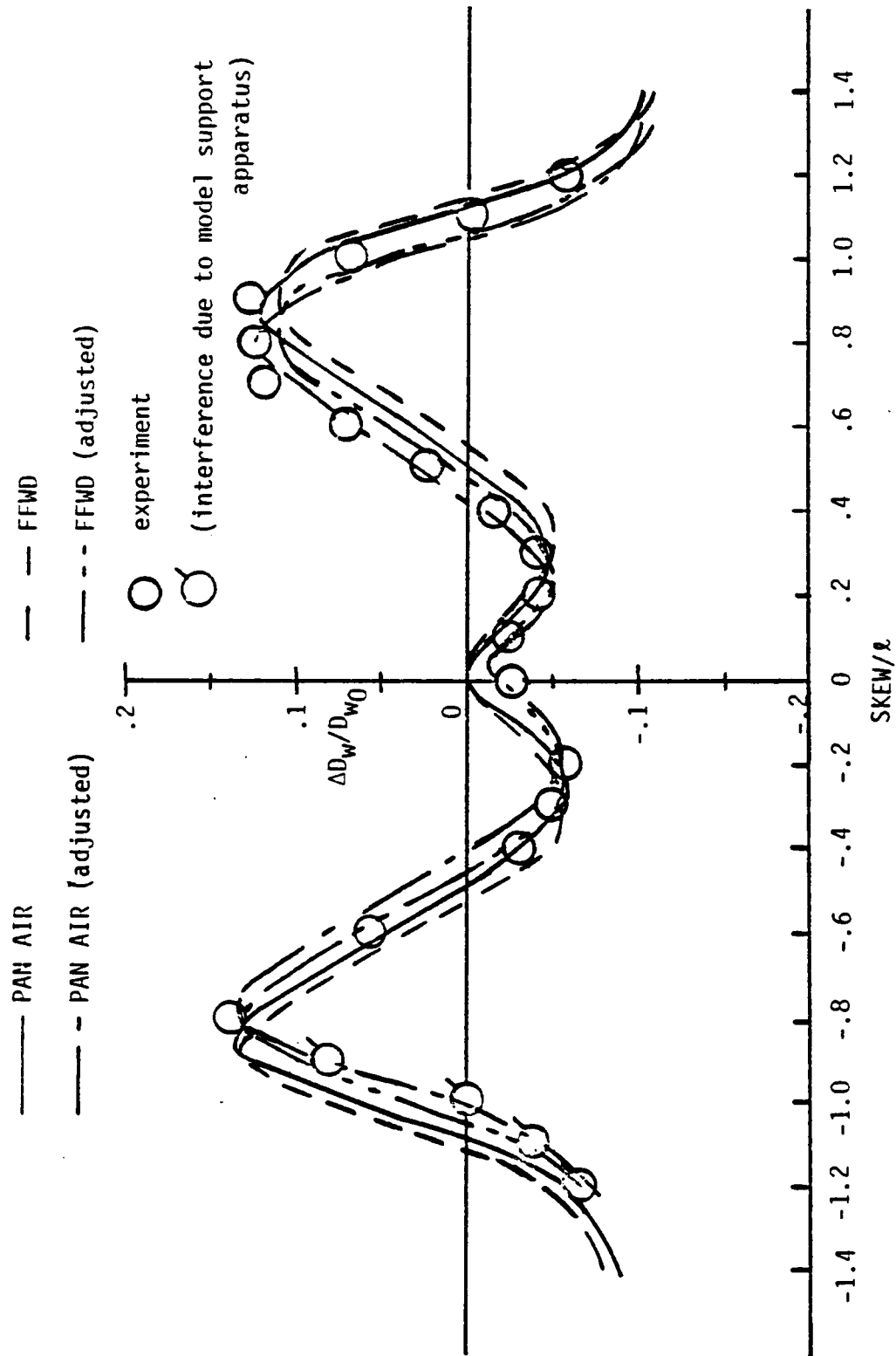
Figure 41.- Comparison of $\Delta D_W/D_{W0}$ versus SKEW/ℓ at SEP/ℓ = .40 for the configuration between experiment, PAN AIR, and FFWD.

SKEW/ℓ

−.3

−.2

0

.2

.3

.4

.5

blade

Mach lines
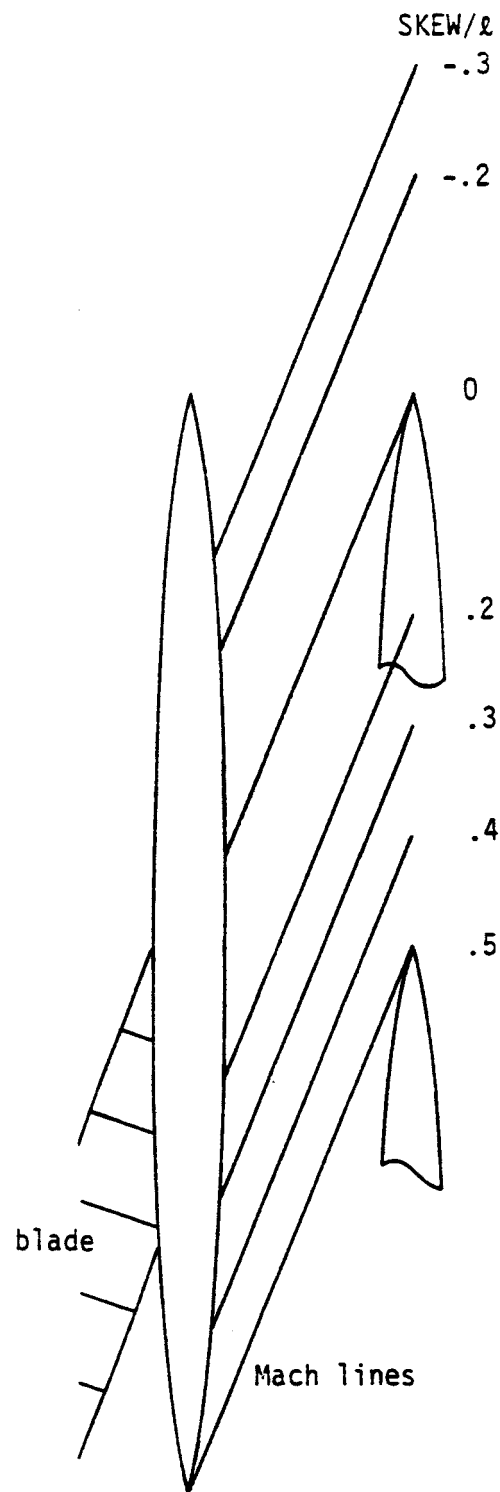
Figure 42.- Illustration of different positions of SKEW/ℓ
at SEP/ℓ = .20.
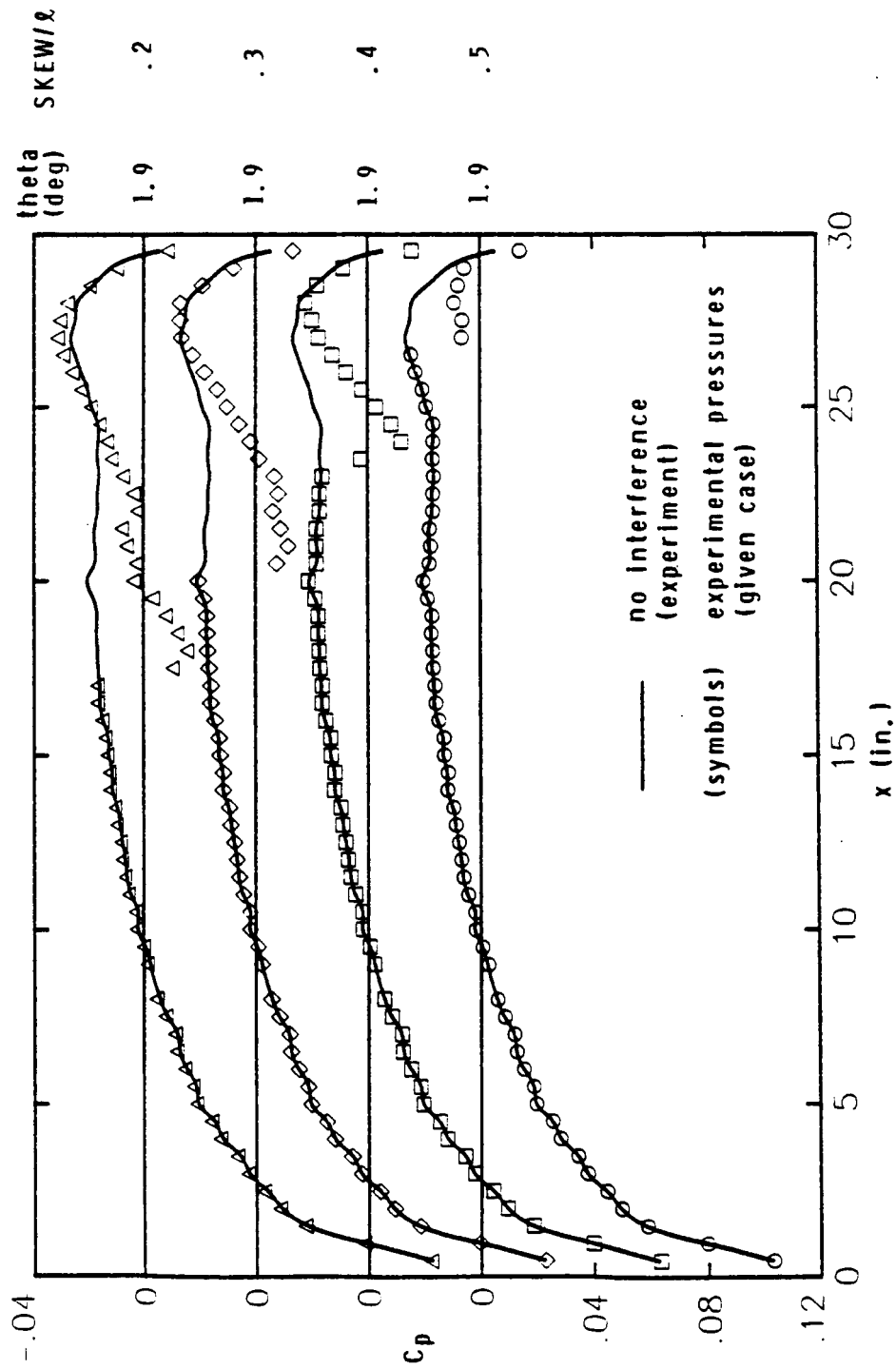
(a) SKEW/ℓ = .5 to .2

Figure 43. - Experimental pressure distributions for different values of SKEW/ℓ at SEP/ℓ = .20.
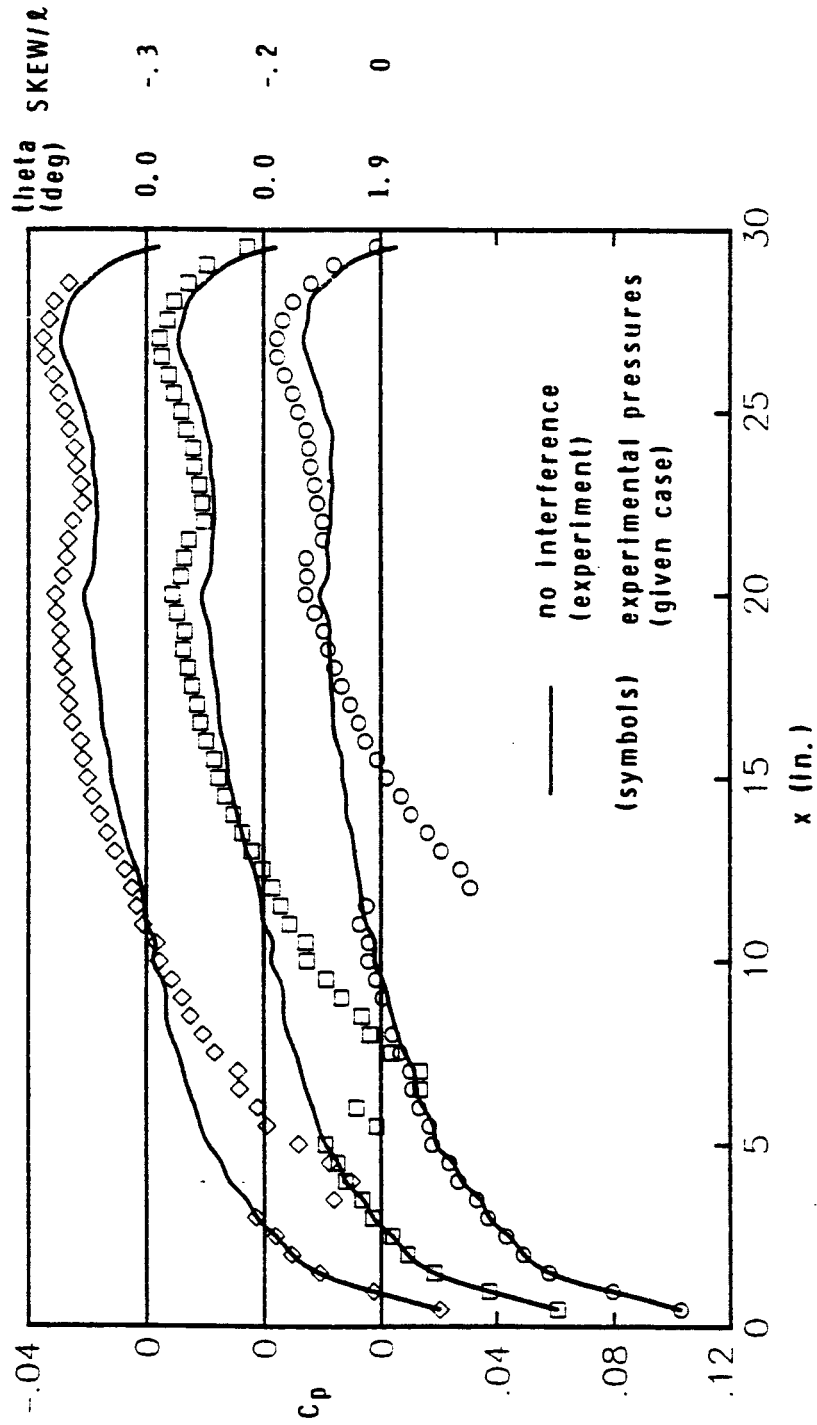
(b) SKEW/ℓ = 0 to -.3

Figure 43. - Concluded.
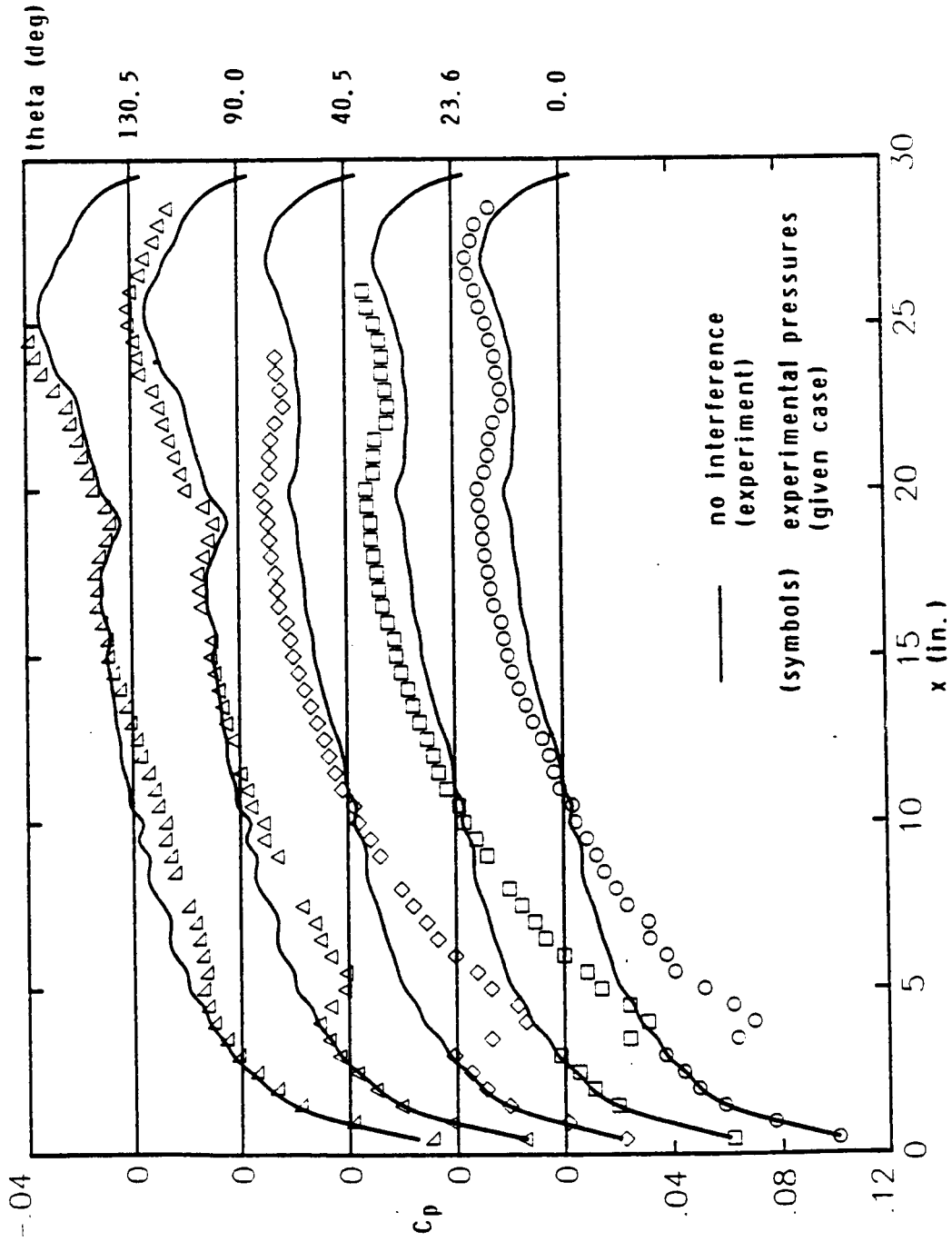
Figure 44. - Experimental pressure distributions around the body for SEP/ℓ = .20 and SKEW/ℓ = -.30.
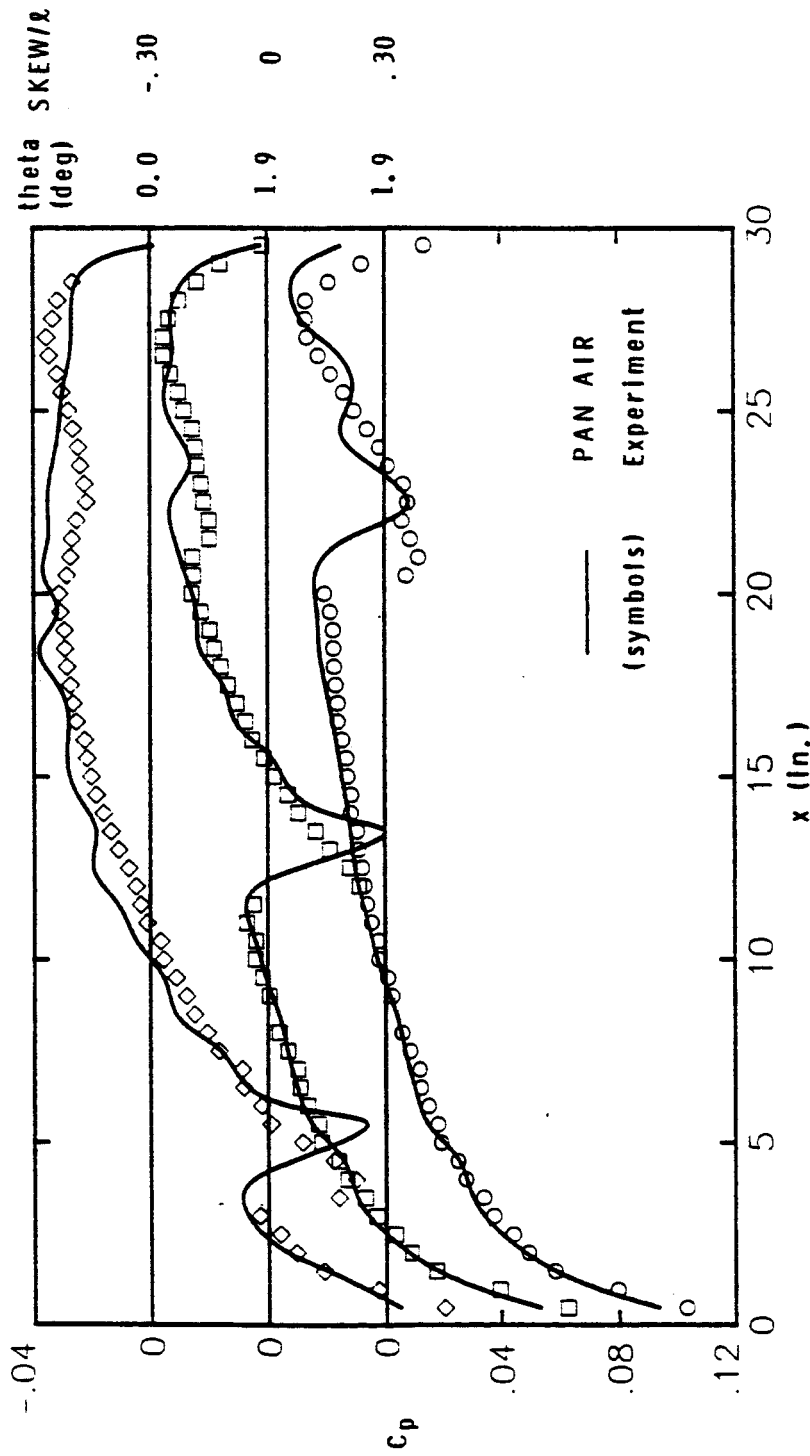
Figure 45. - Pressure distribution comparisons between PAN AIR and experiment at SEP/ℓ = .20 for SKEW/ℓ = .30, 0, -.30.
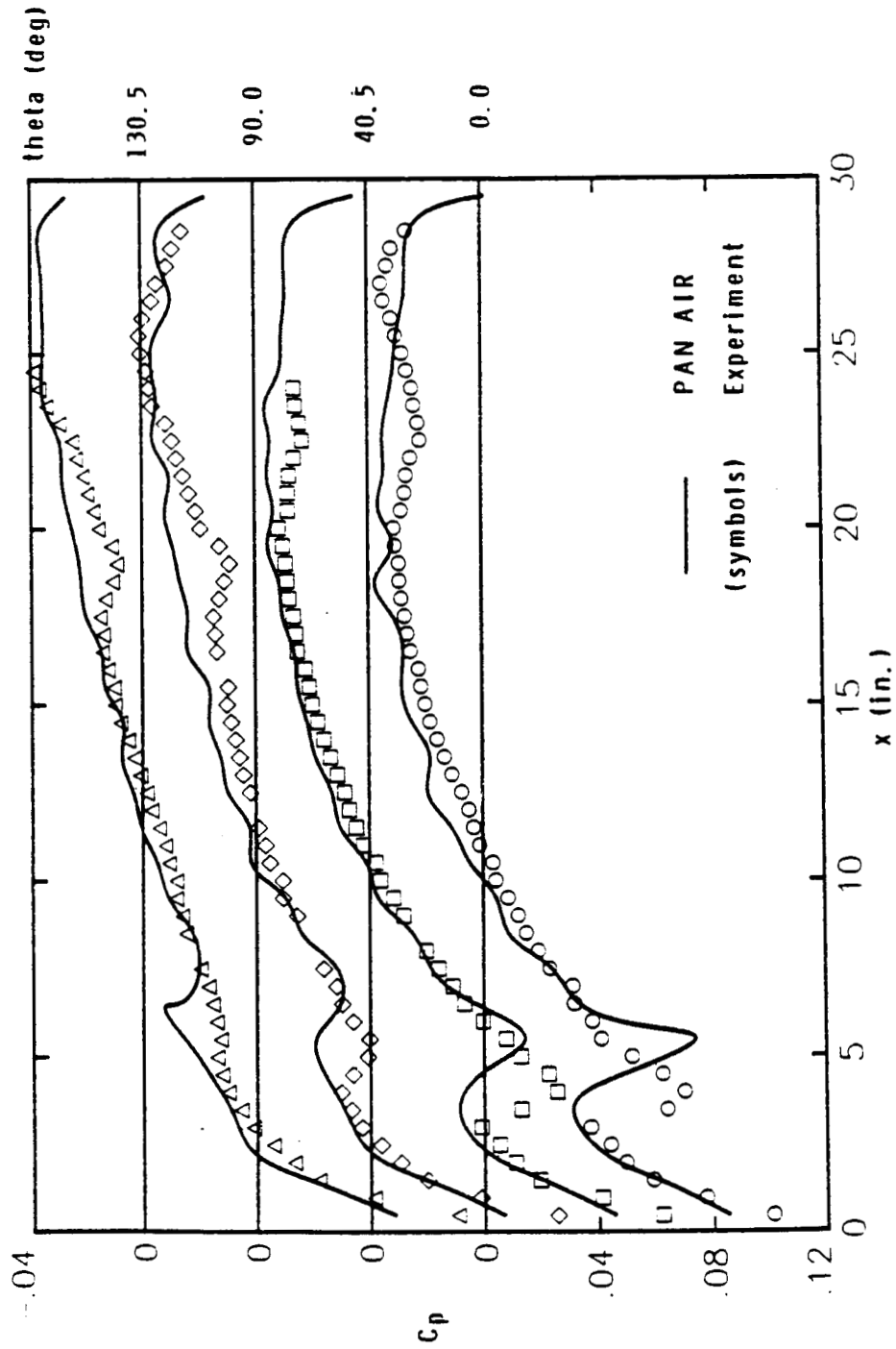
Figure 46. - Pressure distribution comparisons between PAN AIR and experiment around the body for SEP/ℓ = .20 and SKEW/ℓ = -.30.
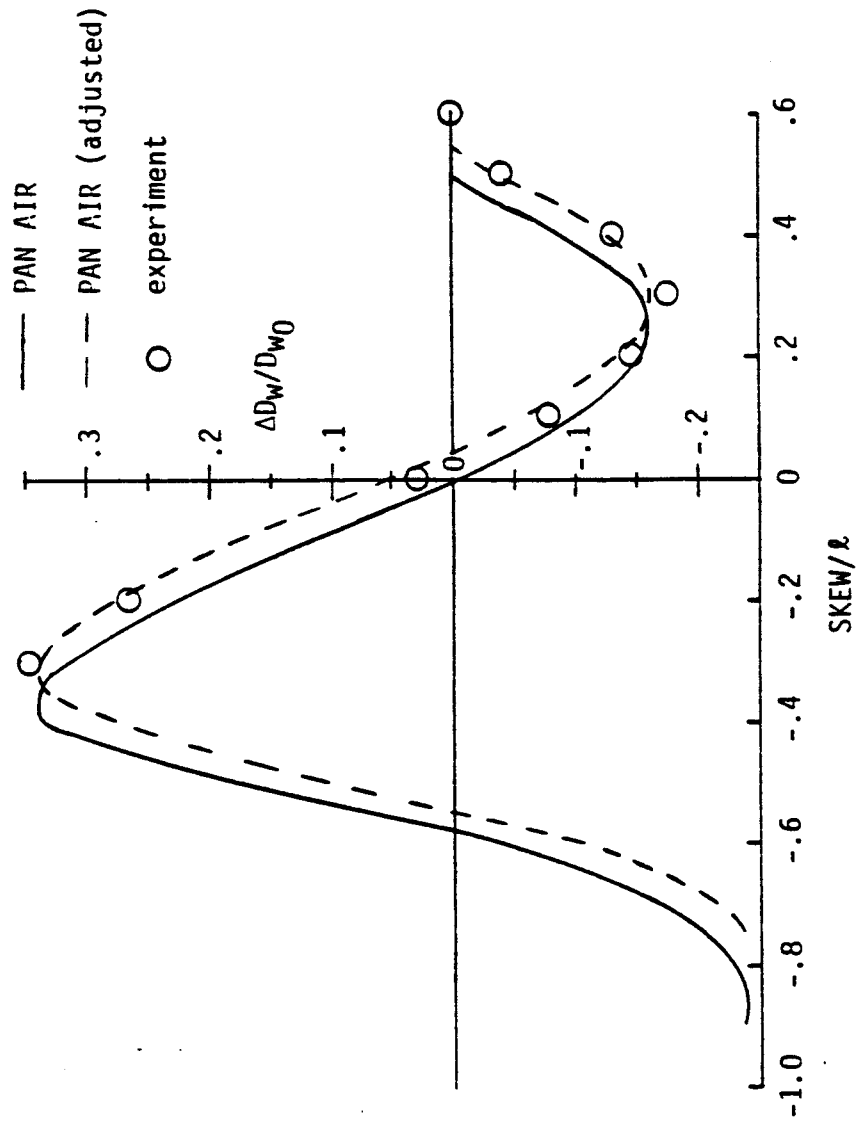
Figure 47.- Comparison of $\Delta D_W/D_{W0}$ versus SKEW/ℓ at SEP/ℓ = .20 between experiment and PAN AIR for the 30" body.
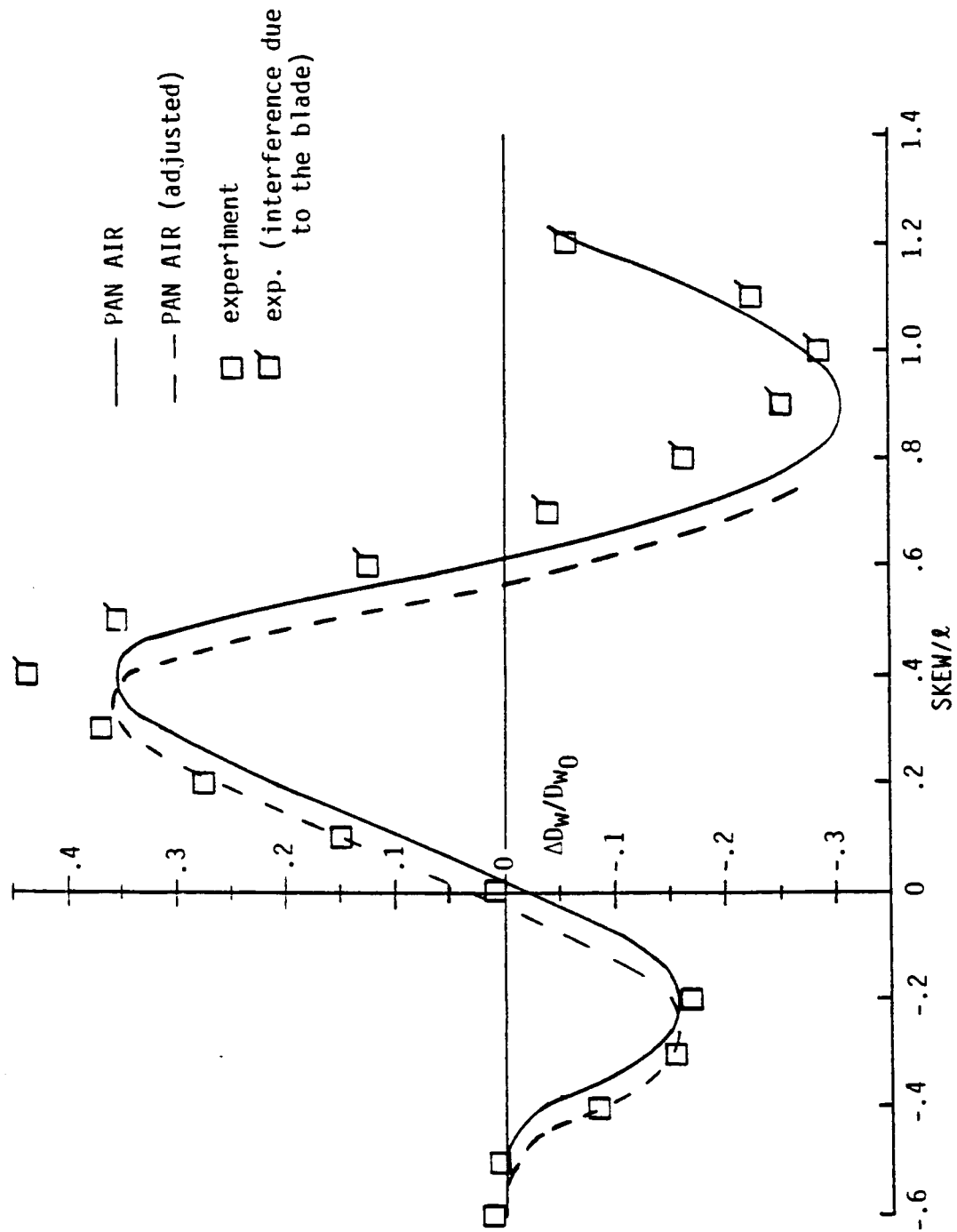
Figure 48.- Comparison of $\Delta D_W/D_{W_0}$ versus SKEW/ℓ at SEP/ℓ = .20 between experiment and PAN AIR for the cutoff body.
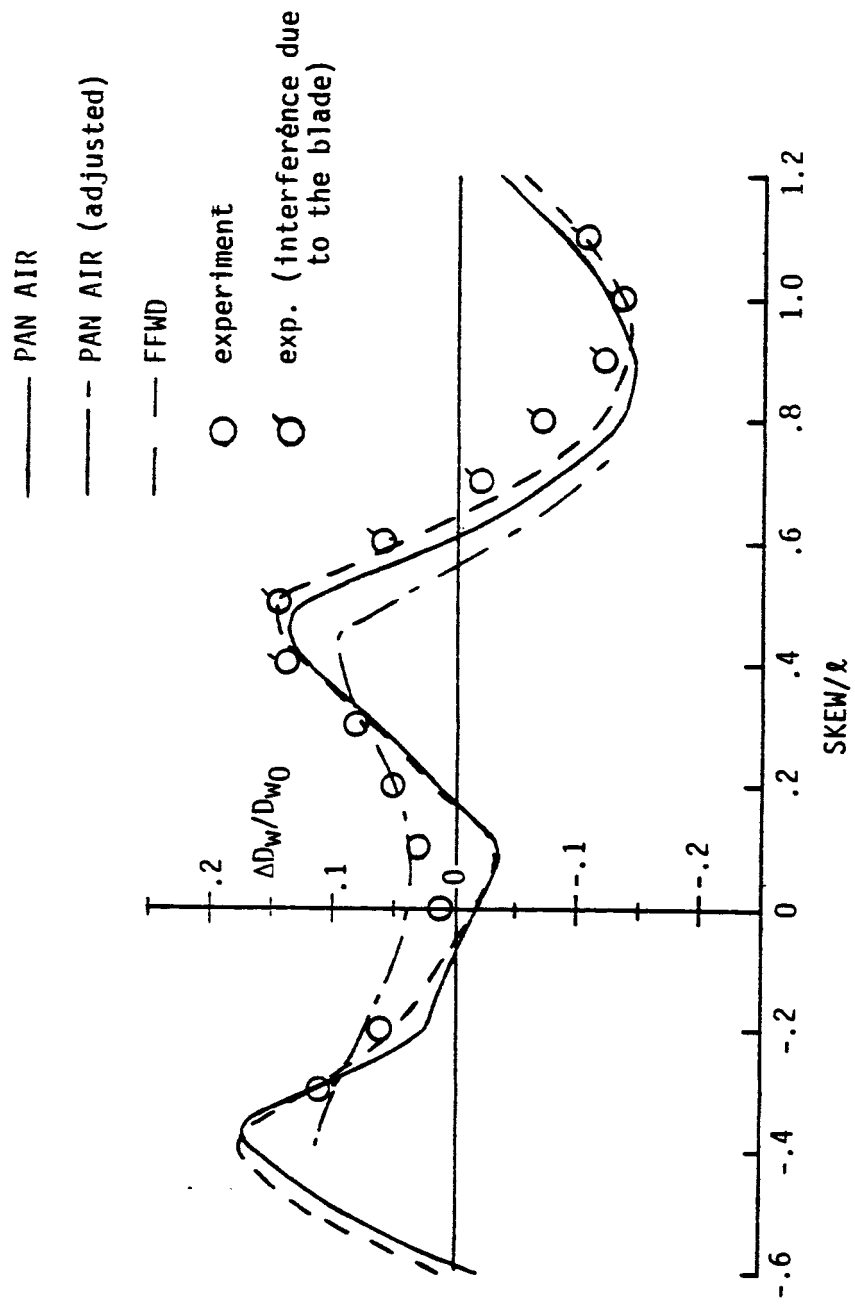
Figure 49.- Comparison of $\Delta D_W/D_{W_0}$ versus SKEW/ℓ at SEP/ℓ = .20 between experiment, PAN AIR, and FFWD for the configuration.
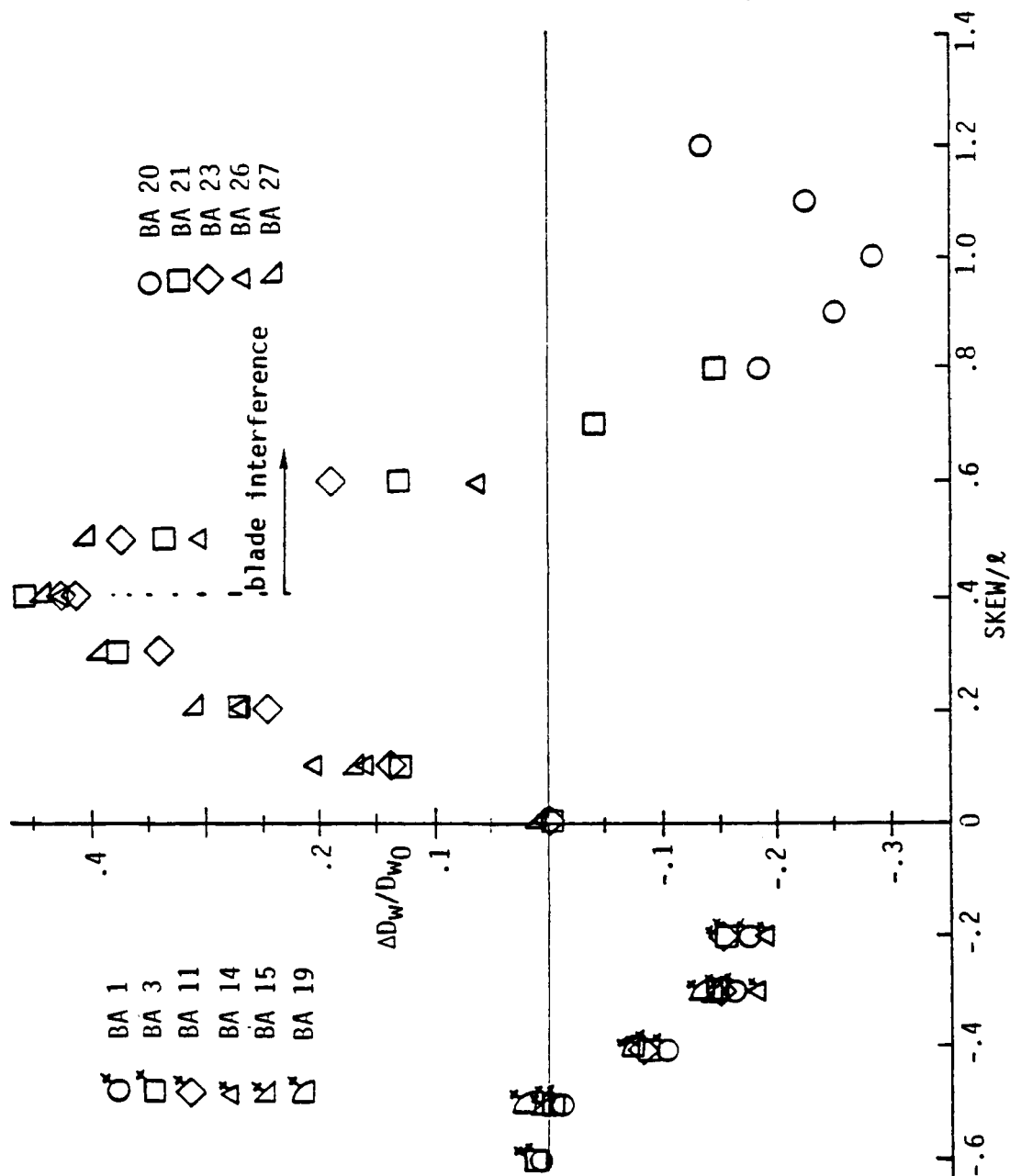
Figure 50.- Experimental values of $\Delta D_W/D_{W0}$ versus SKEW/ℓ at SEP/ℓ = .20 for the cutoff body (different batches).
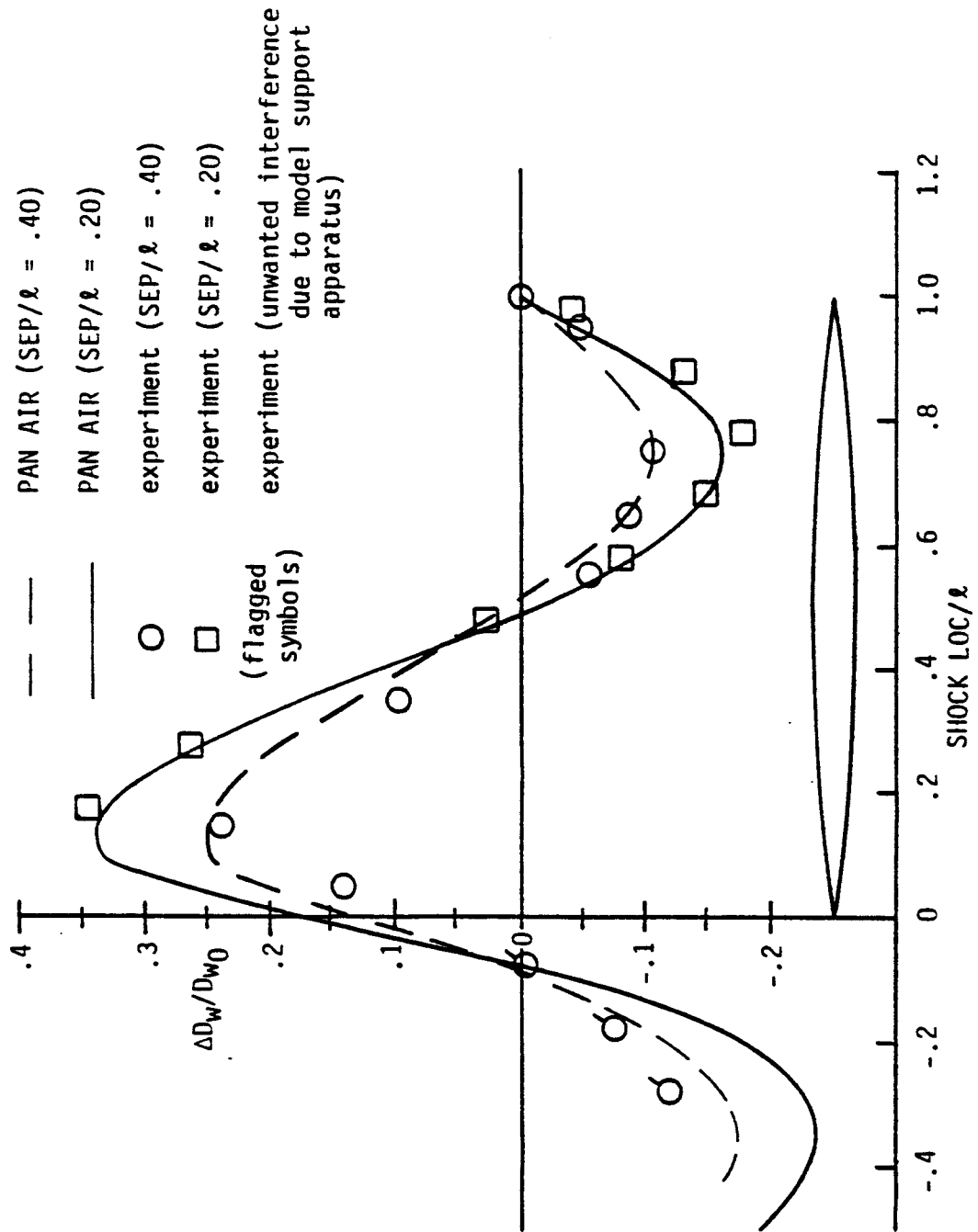
Figure 51.- Values of $\Delta D_W/D_{W_0}$ from the experiment and PAN AIR versus the shock location on the 30" body.

Equation for a parabolic body:

$$\begin{cases} r(x) = (.23571)x - (.01389)x^2 & 0 \leq x \leq 14.14 \text{ cm} \\ r(x) = .55578 & 14.14 \leq x \leq 33.94 \text{ cm} \end{cases}$$

14.14 cm

16.97 cm

33.94 cm
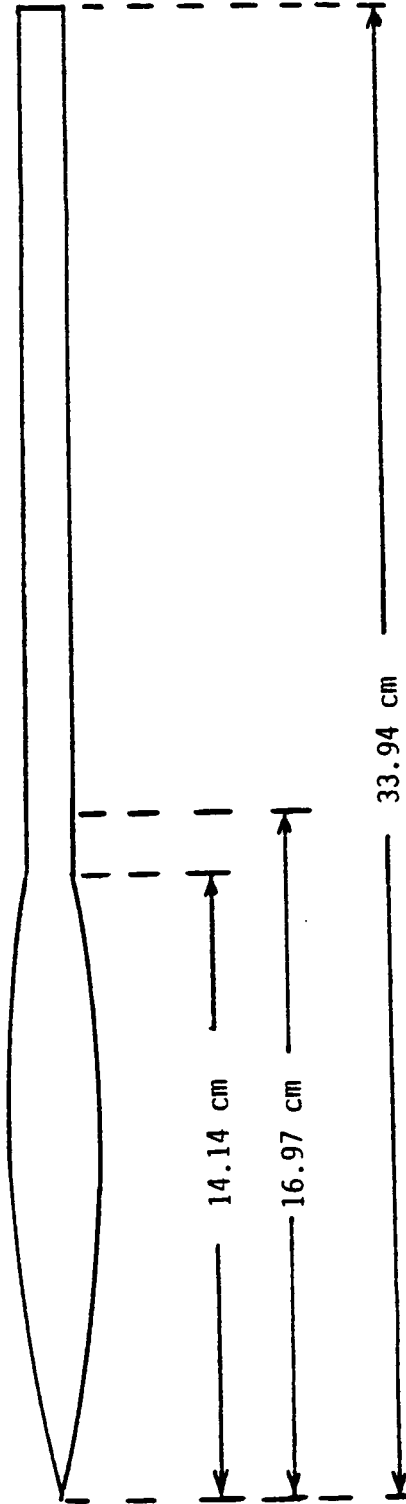
Figure 52.- Parabolic bodies (ref. 5).
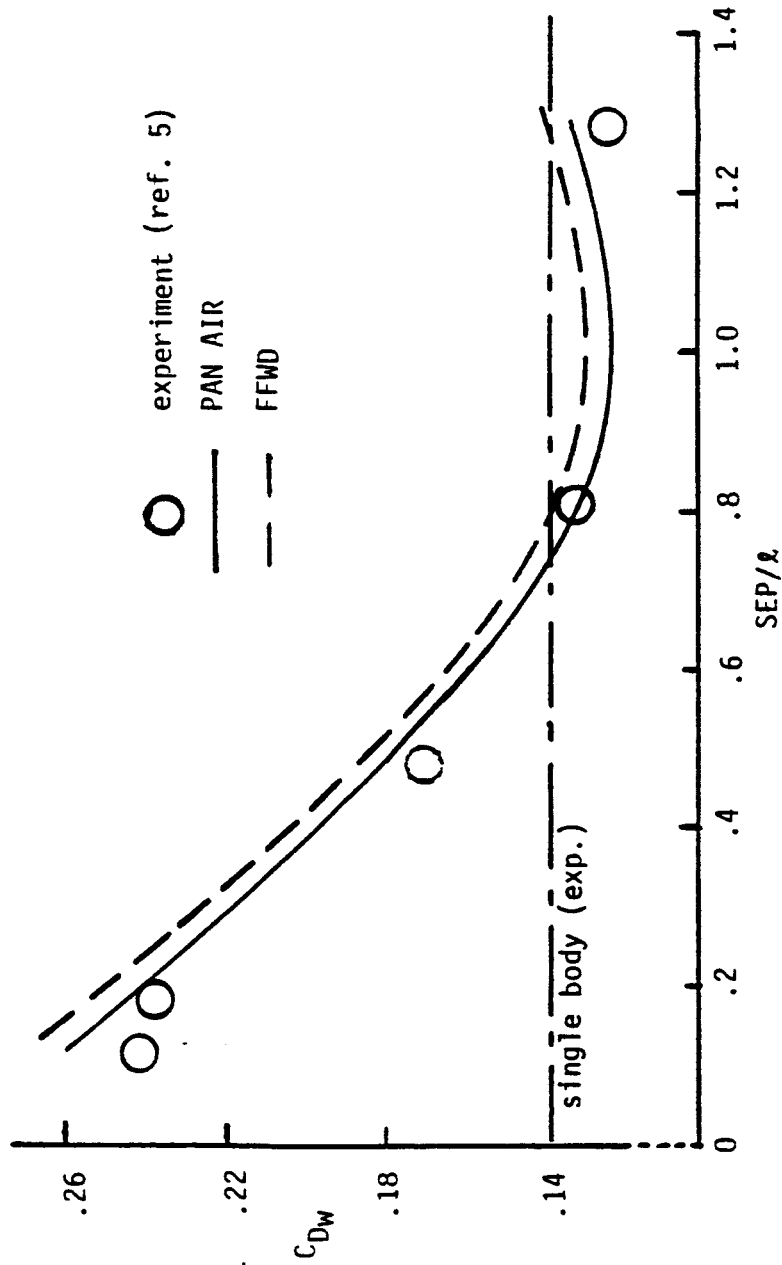
Figure 53.- Wave drag versus separation in body lengths (SEP/ℓ) (full bodies)
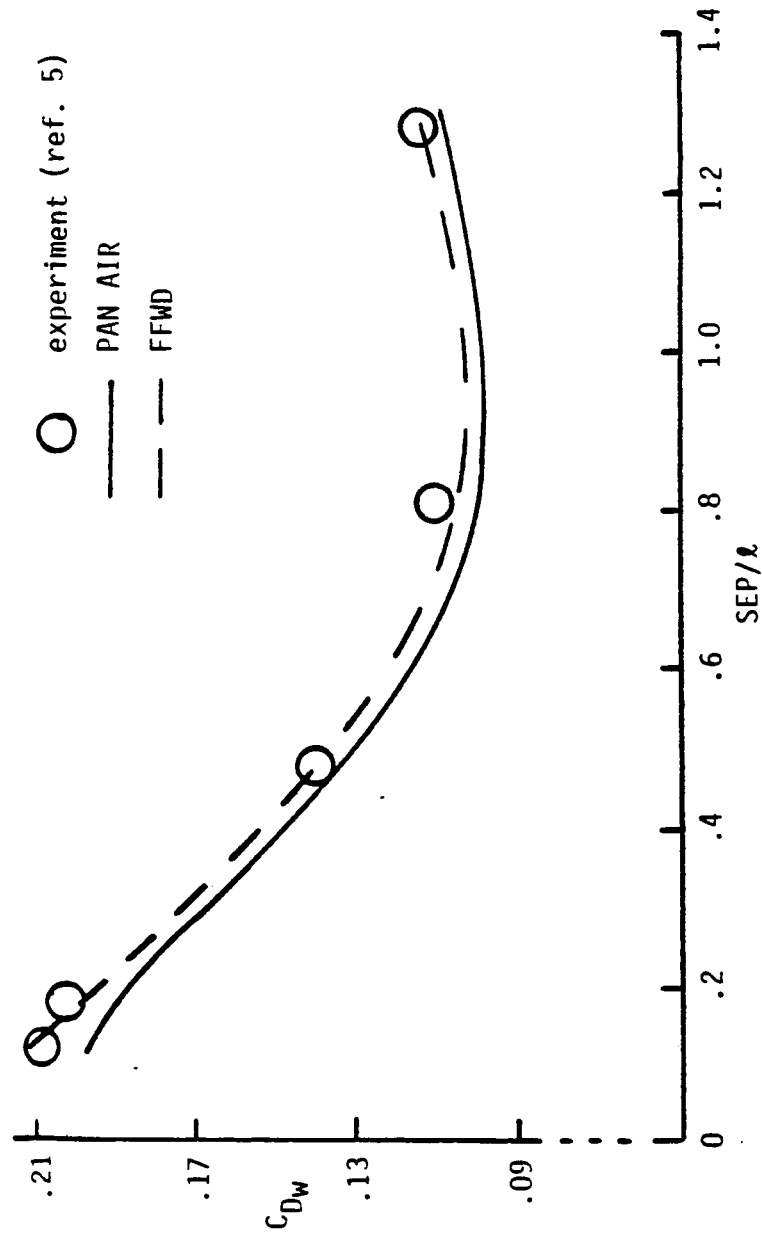
Figure 54.- Wave drag versus separation in body lengths (SEP/ℓ) (part bodies)

.Table I.- Test summary (data point number for given seperation, skew and batch).

SEP = 15

BA	0	-6	-12	-15	-18	-21	-24	Δ (in)	θ₁	θ₂
					SKEW				θ_1	θ_2
1	15	23	33		39		44	0.00	no press data	
3	136	144	157		164		170	0.00	0.0°	90.0°
15	685	695	705		712		717	2.40	9.2°	99.2°
19	867	875	882		888		893	3.90	15.1°	105.1°
11	445	451	458		463		467	5.05	19.7°	109.7°
14	622,628	634	641		646		650	5.43	21.2°	111.2°
4	197	198	204	206		208		8.12	32.7°	122.7°
7	308	310	313		315			9.59	39.7°	129.7°
8	341	344	347		350		352	11.08	47.6°	137.6°

BA	-24	-30	-33	-36	-39	-42	-45	Δ (in)	θ_1	θ_2
2	85	92	98	101	106	108	111	0.00	0.0°	90.0°
16	744	752	758	761,768	765,772	774	777	2.46	9.4°	99.4°
18	829	835	839	842	846	848		3.98	15.4°	105.4°
10	392	399	403	406	409	411	413	5.17	20.2°	110.2°
17	795	802	806	809	812	814	816	5.47	21.4°	111.4°
12	554	557	559	561	563	564	566	8.05	32.4°	122.4°
6	276	279	281	283	285	286	288	9.77	40.6°	130.6°
9	371	374	376	378	380	381	383	11.20	48.3°	138.3°

BA	0	3	6	9	12	15	18	21	24	Δ (in)	θ_1	θ_2
21	1035		1026			1017	1009,1011	1003	997	991	0.19	0.7° 89.3°
26	1222,1248	1244								2.68	10.3°	100.3°
27	1273,1288	1283	1280							4.19	16.2°	106.2°
23	1102,1136	1132	1128							4.88	19.0°	109.0°
25	1176,1190	1186	1183							5.68	22.2°	112.2°
24	1149,1160	1157	1155	1153						7.88	31.6°	121.6°
22	1072,1080	1078	1075							9.40	38.8°	128.8°

BA	24	30	33	36	39	42	45	48	Δ (in)	θ_1	θ_2
20	968	960	954	947	938	935	929	914,922	-0.21	0.8°	89.2°

Table I.- Continued.

SEP = 12

				SKEW							
BA	0	-6	-9	-12	-15	-18	-21	-24	Δ (in)	θ_1	θ_2
1	16	24	29	34		40		45	0.00	no press. data	
3	137	145	153	158		166		172	0.00	0.0°	90.0°
15	686	696	702	706		713		718	2.40	11.5°	101.5°
19	868	876	880	883		889		894	3.90	19.0°	109.0°
11	446	452	456	459		464		469	5.05	24.9°	114.9°
14	623,629	635	639	642		647		651	5.43	26.9°	116.9°
4	194	199	202,203	205	207		209		8.12	42.6°	132.6°
7	309	311	312	314		316			9.59	53.0°	143.0°
8	342	345	346	348		351			11.08	67.4°	157.4°

				SKEW						
BA	-24	-27	-30	-33	-36	-42	-45	Δ (in)	θ_1	θ_2
2	86	89	93	99	102	109	112	0.00	0.0°	90.0°
16	745	750	753	759	762,769	775	778,780	2.46	11.8°	101.8°
18	830	833	836	840	843	849		3.98	19.3°	109.3°
10	393	397	400	404	407	412	415	5.17	25.5°	115.5°
17	796	800	803	807	810	815	817	5.47	27.0°	117.0°
12	555	556	558	560	562	565	567	8.05	32.4°	122.4°
6	277	278	280	282	284	287	290	9.77	54.5°	144.5°
9	372	373	375	377	379			11.20	69.0°	159.0°

					SKEW							
BA	0	3	6	9	12	15	18	21	24	Δ (in)	θ_1	θ_2
21	1036	1032	1027	1023	1018	1012	1004	998	992	0.19	0.9°	89.1°
26	1249	1245								2.68	12.9°	102.9°
27	1289	1285								4.19	20.4°	110.4°
23	1137	1133	1129	1111,1124						4.88	24.0°	114.0°
25	1191									5.68	28.2°	118.2°
24	1161	1158								7.88	41.0°	131.0°
22	1081	1079	1077	1074						9.40	51.6°	141.6°

					SKEW							
BA	24	27	30	33	36	39	42	45	48	Δ (in)	θ_1	θ_2
20	969	964	961	955	948	942	936	930	923	-0.21	1.0°	89.0°

Table I.- Continued.

SEP = 10.5, SKEW = 0

BA	POINT	Δ (in)	θ_1	θ_2
1	17	0.00	no press.	data
3	138	0.00	0.0°	90.0°
15	687	2.40	13.2°	103.2°
19	869	3.90	21.8°	111.8°
11	447	5.05	28.7°	118.7°
14	624,630	5.43	31.1°	121.1°
4	195	8.12	50.6°	140.6°
21	1037	-0.19	1.1°	88.9°
26	1250	2.68	14.8°	104.8°
27	1291	4.19	23.5°	113.5°
23	1138	4.88	27.7°	117.7°
25	1192	5.68	32.7°	122.7°
24	1162	7.88	48.5°	138.5°
22	1082	9.40	63.5°	153.5°

Table I.- Continued.

SEP = 9

BA	0	-6	-12	-15	-18	SKEW -21	-24		Δ (in)	θ₁	θ₂
1	18	25	35	37	41	43	46		0.00	no press. data	
3	139	146	160	162	167	169	173		0.00	0.0°	90.0°
15	688	698	707	710	714	716	719		2.40	15.0°	105.4°
19	870	877	884	886	890	892	895		3.90	27.7°	115.7°
11	448	454	460	462	465	466	470		5.05	34.1°	124.1°
14	625,631	637	643	645	648	649	652		5.43	37.1°	127.1°
4	196	200							8.12	64.4°	154.4°

BA	-24	-30	-33	-36	-39	SKEW -45		Δ (in)	θ₁	θ₂
2	87	95	100	103	107	113		0.00	0.0°	90.0°
16	746	755	760	763,770	773	781		2.46	15.8°	105.8°
18	831	837	841	844	847			3.98	26.2°	116.2°
10	394	401	405	408	410	416		5.17	35.1°	125.1°
17	798	804	808	811	813	818		5.47	37.4°	127.4°

BA	0	3	6	9	12	SKEW 15	18	21	24	Δ (in)	θ₁	θ₂
21	1038	1033	1028	1024	1019	1013	1005	999	993	-0.19	1.2°	88.8°
26	1223,1251	1246	1240	1239				1226		2.68	17.3°	107.3°
27	1292	1286	1281	1278	1275					4.19	27.7°	117.7°
23	1139	1134	1130	1112,1125	1108					4.88	32.8°	122.8°
25	1193	1187	1184	1181						5.68	39.1°	129.1°
24	1163	1159	1156	1154	1151					7.88	61.0°	151.0°

BA	24	30	33	36	39	SKEW 45	48	Δ (in)	θ₁	θ₂
20	970	962	956	949,950	943	931	925	-0.21	1.3°	88.7°

Table I.- Continued.

SEP = 7.5, SKEW = 0

BA	POINT	Δ (in)	θ_1	θ_2
1	19	0.00	no press. data	
3	140	0.00	0.00	90.0°
15	689	2.40	18.6°	108.6°
19	871	3.90	31.3°	121.3°
11	449	5.05	42.3°	132.3°
14	626	5.43	46.4°	136.4°
26	1252	2.68	21.0°	111.0°
27	1293	4.19	33.9°	123.9°
23	1140	4.88	40.6°	130.6°
25	1194	5.68	49.2°	139.2°

SEP = 7.0

BA	Skew = 0 POINT	Δ (in)	θ_1	θ_2
21	1039	-0.19	1.6°	88.4°

Table I.- Continued.

SEP = 6

BA	0	-6	-9	-12	-15	SKEW -18	-24	Δ (in)	θ₁	θ₂
1	20	26	30	36	38	42	47	0.00	no press.	data
3	141	148	154	161	163	168	174	0.00	0.0°	90.0°
15	690	699	703	708	711	715	720	2.40	23.5°	113.5°
19	872	878	881	885	887	891	896	3.90	40.5°	130.5°
11	450	455	457	461				5.05	57.3°	147.3°
14	627,633	638	640	644				5.43	64.8°	154.8°

BA	-24	-27	-30	-36	-42	SKEW -45	Δ (in)	θ₁	θ₁
2	88	90	96	104	110	114	0.00	0.0°	90.0°
16	747	751	756	764,771	776	782	2.46	24.1°	114.1°
18	832	834	838	845	850		3.98	41.5°	131.5°
10	395	398	402				5.17	59.5°	149.5°
17	799	801	805				5.47	65.5°	155.5°

BA	0	3	6	9	12	SKEW 15	18	21	24	Δ (in)	θ₁	θ₂
21	1040	1034	1029	1025	1020	1014	1006	1000	994	-0.19	1.8°	88.2°
26	1253	1247	1241		1235	1232	1229			2.68	26.5°	116.4°
27	1294	1287	1282	1279	1276	1274				4.19	44.3°	134.3°
23	1142	1135	1131	1126	1109,1122	1105	1104			4.88	54.4°	144.4°
25	1195	1189	1185	1182	1179	1178				5.68	71.1°	161.1°

BA	24	27	30	33	36	SKEW 39	42	45	48	Δ (in)	θ₁	θ₂
20	971	965	963	957	951	944	937	932	927	-0.21	2.0°	88.0°

Table I.- Continued.

SEP = 4

BA	0	-3	-6	-9	-12	SKEW	-24	-30	Δ (in)	θ_1	θ_2
1	21	22	28	31					0.00	no press. data	
3	142	143	150	155					0.00	0.0°	90.0°
15	691	693	700	704	709				2.40	36.8°	126.8°
19	873	874	879						3.90	77.0°	167.0°
16							748	757	2.46	37.9°	127.9°

BA	0	6	12	15	18	21	SKEW 24	Δ (in)	θ_1	θ_2
21	1041	1030	1021	1015	1007	1001	995	-0.19	2.8°	87.2°
26	1254	1242	1236	1233	1230	1227	1224	2.68	42.0°	132.0°

BA	24	27	33	36	39	45	SKEW 48	Δ (in)	θ_1	θ_2
20	972	966	958	952	945	933	928	-0.21	2.9°	87.1°

Table I.- Concluded.

SEP = 3

BA	0	-3	-6	-9	SKEW	-24	Δ (in)	θ₁	θ₂
1				32			0.00	no. press. data	
3			151	156			0.00	$0.0°$	$90.0°$
15	692	694					2.40	$53.0°$	$143.0°$
16						749	2.46	$54.9°$	$144.9°$

BA	0	6	12	15	18	21	SKEW 24	Δ (in)	θ₁	θ₂
21		1031	1022	1016	1008	1002	996	-0.19	$3.7°$	$86.3°$
26	1255	1243	1237	1234	1231	1228	1225	2.68	$63.3°$	$153.3°$

BA	24	27	33	36	39	45 SKEW	Δ (in)	θ₁	θ₂
20	973	967	959	953	946	934	-0.21	$3.9°$	$86.1°$

Table 1I.- D_w/q of the 30" body for the two different test section locations.

Front location of 30" body in test section:

Batch(s)	No. of test points	D_w/q
20	38	.1381
21	33	.1382
22-23	16	.1374
24-27	27	.1386
Ave		.1381

Aft Location of 30" body in test section

Batch(s)	No. of test points	D_w/q
1-14	9	.1483